# Neural Recordings, Implant Refinement, and Rethinking Sample Sizes in Non-Human Primate Research





RADBOUD UNIVERSITY PRESS

# Neural Recordings, Implant Refinement, and Rethinking Sample Sizes in Non-Human Primate Research

Eleni Psarou

The research presented in this thesis was carried out at the Ernst Strüngmann Institute (ESI) for Neuroscience in Cooperation with Max Planck Society, in Frankfurt am Main, Germany.

Author: Eleni Psarou

Title: Neural Recordings, Implant Refinement, and Rethinking Sample Sizes in Non-

Human Primate Research

#### **Radboud Dissertations Series**

ISSN: 2950-2772 (Online); 2950-2780 (Print)

Published by RADBOUD UNIVERSITY PRESS Postbus 9100, 6500 HA Nijmegen, The Netherlands www.radbouduniversitypress.nl

Design: Proefschrift AIO | Guus Gijben Cover: Proefschrift AIO | Guntra Laivacuma

Printing: DPN Rikken/Pumbo

ISBN: 9789465150352

DOI: 10.54195/9789465150352

Free download at: www.boekenbestellen.nl/radboud-university-press/dissertations

© 2025 Eleni Psarou

# RADBOUD UNIVERSITY PRESS

This is an Open Access book published under the terms of Creative Commons Attribution-Noncommercial-NoDerivatives International license (CC BY-NC-ND 4.0). This license allows reusers to copy and distribute the material in any medium or format in unadapted form only, for noncommercial purposes only, and only so long as attribution is given to the creator, see http://creativecommons.org/licenses/by-nc-nd/4.0/.

# Neural Recordings, Implant Refinement, and Rethinking Sample Sizes in Non-Human Primate Research

Proefschrift ter verkrijging van de graad van doctor aan de Radboud Universiteit Nijmegen op gezag van de rector magnificus prof. dr. J.M. Sanders, volgens besluit van het college voor promoties in het openbaar te verdedigen op

> maandag 10 februari 2025 om 14.30 uur precies

> > door

Eleni Psarou

geboren op 7 juni 1991 te Athene (Griekenland)

#### **Promotor:**

Prof. dr. P. Fries

# **Copromotor:**

Dr. M.L. Schölvinck (Ernst Strüngmann Institut, Duitsland)

# Manuscriptcommissie:

Prof. dr. R.J.A. van Wezel

Dr. T.J. van Kerkoerle

Prof. dr. M. Wilke (Georg-August-Universität Göttingen, Duitsland)

# Neural Recordings, Implant Refinement, and Rethinking Sample Sizes in Non-Human Primate Research

Dissertation to obtain the degree of doctor from Radboud University Nijmegen on the authority of the Rector Magnificus prof. dr. J.M. Sanders, according to the decision of the Doctorate Board to be defended in public on

> Monday, February 10, 2025 at 2:30 pm

> > by

Eleni Psarou

born on June 7, 1991 in Athens (Greece)

# PhD supervisor:

Prof. dr. P. Fries

# PhD co-supervisor:

Dr. M.L. Schölvinck (Ernst Strüngmann Institute, Germany))

# **Manuscript Committee:**

Prof. dr. R.J.A. van Wezel

Dr. T.J. van Kerkoerle

Prof. dr. M. Wilke (University of Göttingen, Germany)

# **Table of contents**

Chapter 1	
General Introduction	11
Introductory Remarks	12
General Introduction	13
Chapter 2	
Modular, cement-free, customized headpost and connector-chamber	
implants for macaques	25
Abstract	26
Introduction	27
Materials and methods	28
Results	59
Discussion	64
Acknowledgements	71
Supplementary materials	72
Chapter 3	
Rethinking sample sizes in NHP research	81
Abstract	82
Introduction	83
Discussion	83
Conclusion	92
Acknowledgements	92
Chapter 4	
Repetition-related gamma plasticity in macaque V1 and V2 is highly	
stimulus specific and robust to stimulus set size	95
Abstract	96
Introduction	97
Materials and Methods	99
Results	113
Discussion	131
Supplementary materials	138
Acknowledgements	146

# **Chapter 5**

•	
General discussion	149
General Discussion	150
Summary of findings	150
Fostering methodological refinements in NHP research	151
Fostering statistical inference in NHP research	152
Repetition-related plasticity: open questions and outlook	153
Bibliography	157
Appendices	169
A1 - Dutch Summary	170
A2 - Abbreviations	172
A3 - Data Management	174
A4 - Acknowledgements	176
A5 - Curriculum Vitae	178
Donders Graduate School	180



# Chapter 1

# **General Introduction**

# **Introductory Remarks**

This thesis is the outcome of several years of experimental work with macaque monkeys in the Fries Lab. When I first joined the lab, I was fascinated by its multimethod approach and the dedication of my colleagues to continuously improve and refine their experimental techniques. This emphasis on methods refinement significantly shaped my PhD research.

Over the years, I had the opportunity to work and contribute to various projects that aimed at elucidating the role of neuronal oscillations in phenomena like attention, visual processing, and neuronal plasticity. These projects gave me the opportunity to gain hands-on experience with a variety of experimental methods, ranging from acute and chronic electrophysiological recordings to optogenetic manipulations.

Throughout this journey, I encountered numerous methodological challenges that motivated me to dedicate substantial efforts on the refinement and development of experimental techniques. My goal was to enhance both animal welfare and the quality of experimental results. Among others, I worked on improving cranial implants, refining implant maintenance, and developing methods for optogenetic manipulations in awake macaques.

Only a portion of this extensive work is presented in this thesis. The chapters are organized to reflect the typical steps involved in conducting experiments with non-human primates (or other animal models). After formulating a scientific question, one needs to choose and develop the required methodology. This includes methods for data acquisition, and the selection of an appropriate sample size.

Chapter 2 details the development of refined cranial implants, which are crucial for data collection and Chapter 3 offers a critical evaluation of the sample sizes typically used in non-human primate studies. These foundational efforts set the stage for the experimental work described in Chapter 4, which investigates the effects of stimulus repetition on neuronal responses in the early visual cortex. The following sections of Chapter 1 introduce key concepts and provide a general background for the work presented later in this thesis.

# **General Introduction**

#### The non-human primate model in neuroscience

The term non-human primates (NHPs) includes prosimians, such as lemurs and tarsiers, as well as simians, like apes and monkeys. Monkeys are subdivided into New World and Old World monkeys, with the latter being phylogenetically the closest to humans (Miller et al., 2016). Macagues, the animal model of this thesis belongs to the Old Word monkeys and have been pivotal in neuroscience research. Over the past ~ 90 years, studies with NHPs have been instrumental in elucidating the neuronal mechanisms underlying several processes in cognition (Passingham, 2009; Roelfsema and Treue, 2014) and particularly in vision (Picaud et al., 2019; Sincich and Horton, 2005).

The visual system of NHPs, particularly Old World primates, shares significant similarities with those of humans. Like humans, NHPs rely predominantly on vision, and a large portion of their cortex is devoted to the processing of visual information. Both NHPs and humans have forward-facing eyes, trichromatic vision, and high visual acuity due to their fovea and macula (Picaud et al., 2019). This high level of similarity make NHPs an unsurpassed model for the study of the primate visual system (Picaud et al., 2019; Sincich and Horton, 2005). Additionally, thanks to their cognitive abilities, studies with NHPs have greatly advanced our knowledge regarding the neural substrate of cognition (Roelfsema and Treue, 2014).

Besides its importance, brain research with NHPs comes with great responsibility as well as practical and ethical challenges for researchers. The following paragraphs summarize a widely accepted ethical framework for conducting animal research and highlights unique methodological challenges associated with the macaque model.

# The 3R principles: an ethical framework for conducting animal research

In 1959, Russell and Burch emphasized the importance of humane practices in animal research to minimize the suffering and distress of experimental animals (Russell and Burch, 1959). They introduced the 3R principles, an ethical framework for animal research. The 3Rs stand for replacement, reduction, and refinement.

Replacement encourages researchers to find alternative methods that do not require the use of living animals. Reduction aims to minimizing the number of animals used in each study to the necessary minimum, and refinement focuses on

improving and optimizing experimental procedures to reduce the suffering and distress caused by experimental intervention.

Today, the 3Rs are widely accepted by the scientific community and have been incorporated into legislation that regulates animal research at a national and international level (Prescott and Poirier, 2021). The adoption of the 3Rs has significantly advanced the conduct of animal research, fostering a culture of care and respect toward experimental animals. These principles also drive innovations that can enhance the quality of scientific research and animal welfare.

Chapter 2 and Chapter 3 of this thesis were motivated by the principles of Refinement and Reduction. In particular, Chapter 2 presents the refinement of cranial implants which are an integral part of data collection in NHP neurophysiology, as explained below.

#### The use of cranial implants in NHP neuroscience

The use of cranial implants in awake behaving animals revolutionized cognitive and systems neuroscience. Researchers were able for the first time to record neuronal activity from awake behaving animals which allowed them to study the neuronal activity that underlies distinct behavioural states (Adams et al., 2007; Johnston et al., 2016). To date, cranial implants are still required in order to record brain activity from awake animals. Invasive recording techniques, such as intracranial electrophysiological recordings, require implants that provide access to the brain, like recording chambers or chronically implanted electrode arrays. Similarly, noninvasive methods, such as functional magnetic resonance imaging (fMRI), typically require head-stabilizing implants to minimize motion artefacts and ensure highquality data acquisition (Ortiz-Rios et al., 2018; Prescott and Poirier, 2021).

The outcome of neurophysiological studies in awake animals depends substantially on the success of the employed cranial implants, and there is pressing need for implants that can remain functional for prolonged periods. Implant longevity is especially important in the context of NHP-neuroscience studies which often require long preparation and behavioral training periods. Behavioral training and neuronal recordings can often last up to several years, and the implants need to remain healthy throughout this period (Lanz et al., 2013). Additionally, the long lifespan of macagues1 (Colman and Anderson, 2011) often allows a single animal to participate in more than one projects, which can lead to a reduction of the number of animals used in research. This is only feasible if the animal and its implants remain in good health.

<sup>1.</sup> In captivity, macaques can live up to 25 years.

## Stimulus repetition in our visual experience

As we navigate and interact with our environment, we frequently encounter the same objects repeatedly. In familiar settings, such as our homes, we see and interact with the same items for extended periods of time. Even over shorter intervals, while performing simple tasks like preparing a meal, we primarily focus our eyes at objects that are relevant to our task (Hayhoe and Ballard, 2005). Thus, stimulus repetition is a fundamental aspect of our perceptual experience, taking place across various timescales ranging from seconds to years. Chapter 4 investigates the effects of stimulus repetition on the neuronal responses of the early visual cortex. The following sections provide a brief introduction into the connectivity of the visual cortex and gamma-band oscillations, a signature signal of the early visual cortex.

#### Information flow in the early visual cortex

The seminal work of Hubel and Wiesel on the visual cortex of cats revealed that neuronal receptive fields (RFs) in adjacent cortical areas exhibit a progressive increase in selectivity and complexity (Hubel and Wiesel, 1962, 1965). This discovery suggested a sequential processing of visual information across areas, leading to the proposal of a hierarchical model of the macague visual cortex by Felleman and Van Essen (1991).

The proposed visual hierarchy includes over 30 cortical areas, which are heavily interconnected through feedforward (ascending) and feedback (descending) projections. Feedforward connections (FF) originate from lower stages of the hierarchy and contact neurons in higher stages, while feedback projections (FB) originate from higher areas and target lower cortical areas (Felleman and Van Essen, 1991). At the base of this hierarchy is the primary visual cortex (V1) which together with area V2 is often collectively referred to as the 'early visual cortex'.

Visual information travels from the retina to the Lateral Geniculate Nucleus (LGN) of the thalamus before reaching V1 (Fig. 1.1A), the first cortical stage of visual processing. V1 predominantly projects to V2, which in turn sends strong feedback to V1 (Sincich and Horton, 2005).

V1 and V2 are organized into six layers, each with distinct neuronal populations and connectivity patterns. Extensive anatomical studies have revealed strong regularities in neuronal circuits across neocortical regions (Douglas and Martin, 2004; Markov et al., 2014b), leading to the formulation of the 'canonical microcircuit', a simplified model of cortical processing (Douglas and Martin, 2004).

Fig. 1.1B provides a schematic representation of the connections made by excitatory pyramidal neurons within the microcircuit. Feedforward input predominately originates from the superficial layers of the source area (Area A in Fig. 1.1B) and arrives in the granular layers of the target area (Area B in Fig. 1.1B). Granular layers then send outputs to superficial layers, which project to the deep layers of the same area as well as to the granular layers of the next area. Feedback connections primarily originate from the deep and superficial layers of the higher areas (Area B in Fig. 1.1B) and arrive outside the granular layer of the receiving area (Area A in Fig 1.1B).

Note that in primate V1, the granular layer (layer 4 or L4) has expanded and specialized into three distinct sublayers: L4A, L4B, and L4C. Fig. 1.1A illustrates the main pathways from LGN to V1. The majority of the thalamic input arrives in L4C and layer 6, with some additional inputs arriving in L3 and L1 (Hendrickson et al., 1978; Vanni et al., 2020).

Within each laminar compartment, information can also spread laterally. Excitatory pyramidal neurons send millimeter-long horizontal projections to other excitatory and inhibitory neurons within the same layer (Angelucci et al., 2002; McGuire et al., 1991). These horizontal projections connect neurons with different receptive fields but otherwise often similar feature preference. Combined anatomical and optical imaging studies have revealed that, in the superficial layers of V1, horizontal connections primarily link neurons with similar orientation preferences (Lund et al., 2003; Malach et al., 1993; Stettler et al., 2002). The frequency and the spread of horizontal connections vary across layers. As shown in Fig. 1.2A, in V1, horizontal connections are more prominent in L2/3 and L5 (Vanni et al., 2020).

Recent advances in electrophysiology have facilitated the study of neuronal activity across different cortical layers (Self et al., 2019). Using multi-contact electrode arrays, researchers can simultaneously record neuronal activity across the cortical sheet. Electrophysiological signals can be used to infer the location of the input layer and assign recording channels to different laminar compartments. Even though this grouping is tentative, these experiments provide valuable insights into layer-specific neuronal computations and inter-laminar interactions.

#### Gamma-band oscillations in the visual cortex

Neuronal networks often engage in rhythmic oscillatory activity across a wide range of frequencies. Since the late 1980s, oscillations in the gamma frequency range have gained significant attention in systems neuroscience (Engel et al., 1991; Gray et al., 1989; Gray and Singer, 1989). To date, gamma oscillations have A Thalamic inputs in area V1

#### Superficial 1 2/3 L4A Cortical layers Granular L4B **LGN** L4Ca Contra L4Cß K6 Ipsi = K5⊏ L5 Contra = K4 ⊏ Ipsi L6 КЗ Ipsi Μ K2

#### B Canonical microcircuit

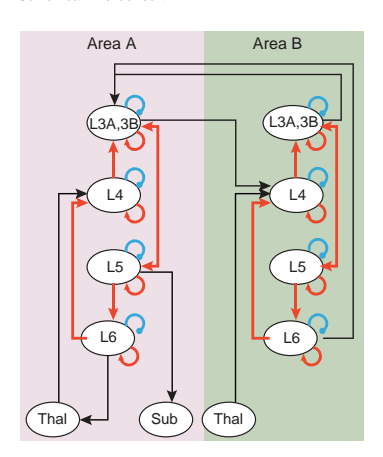


Figure 1.1. (A) Illustration of the thalamic pathways from LGN to V1. The thickness of the arrows indicate the relative projection strength of each pathway. The majority of LGN afferents from the Parvocellular (P) and Magnocellular (M) pathways terminate in L4, with L6 receiving some additional projections. The Koniocellular (K1-K6) pathway terminates in the superficial layers of V1 (L1- L2/3). Adapted from Vanni et al. (2020). (B) Illustration of the canonical microcircuit of Douglas and Martin (2004). Red (black) arrows depict intra-areal (inter-areal) connections. Abbreviations: Thal: Thalamus; Sub: subcortical areas. Adapted from Markov et al. (2013).

A Laminar distribution of horizontal connectivity in V1

B Laminar distribution of gamma power in V1

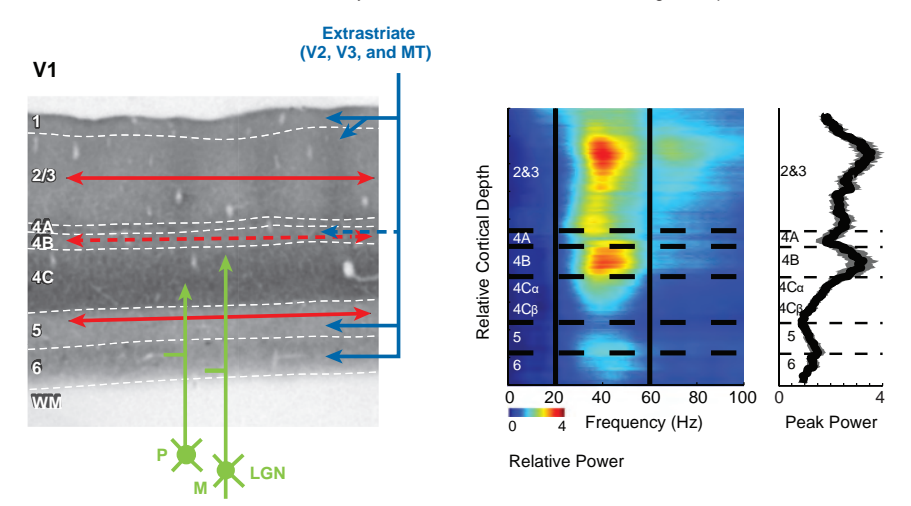


Figure 1.2 Laminar distribution of horizontal connections and gamma-band activity in area V1. (A) Graphical illustration of the horizontal connectivity (red arrows) in area V1 of the monkey. Solid (dashed) arrows indicate more(less) dense projections. Abbreviations: WM: white matter; P: Parvocellular pathway; M: Magnocellular pathway; MT: Middle temporal visual area. Adapted from Angelucci et al. (2017). (B) Left: Laminar distribution of spectral power in response to visual stimulation in area V1 of the monkey. Right: Mean power as a function of cortical depth averaged over a gamma frequency window (20-60 Hz). Adapted from Xing et al. (2012)

inspired extensive experimental research and theories on their functional role and implications (Fries, 2009).

In particular, gamma oscillations have been extensively examined in the context of visual processing. Upon appropriate visual stimulation, the visual cortex of several species including cats, humans and NHPs exhibit gamma oscillations (for a review see: Fries et al. (2007); Fries (2009)). The strength of these oscillations greatly depends on the characteristics of the visual input, with specific stimulus features being linked to stronger or weaker gamma power. The relationship between gamma power and stimulus characteristics has been primarily studied in area V1.

In V1, gamma power gradually increases with stimulus size (Gieselmann and Thiele, 2008, 2022; Jia et al., 2013; Peter et al., 2019) and contrast (Bartoli et al., 2019; Henrie and Shapley, 2005; Roberts et al., 2013). It also positively correlates with the input strength, with stronger input leading to higher gamma power (Lewis et al., 2021). Even though gamma-band oscillations have been extensively studied with achromatic stimuli, more recent studies showed clear gamma responses to chromatic stimuli (Peter et al., 2019; Shirhatti and Ray, 2018; Stauch et al., 2022).

There is also evidence that naturalistic images can induce conspicuous gamma activity in the early visual cortex under both passive fixation (Peter et al., 2021) and free-viewing conditions (Brunet et al., 2015). Gamma oscillations in response to both naturalistic and to artificial stimuli, such as oriented gratings, strongly depends on the structure of the image, with higher homogeneity leading to stronger gamma activity (Brunet and Fries, 2019; Gieselmann and Thiele, 2008; Peter et al., 2019; Uran et al., 2020).

Interestingly, the presentation of large, uniform stimuli leads to opposing effects on spike rates and gamma power. Large homogeneous stimuli tend to elicit strong gamma oscillations but weak spike rates (Gieselmann and Thiele, 2008). The reduction in spike rates with increased stimulus size and homogeneity is thought to result from 'surround modulation' (SM). SM refers to the phenomenon where the response of a neuron to a stimulus presented in the receptive-field (RF) center (also known as 'classical RF') is influenced by stimuli presented in the RF surround. In contrast, when the RF center and RF surround are activated by dissimilar stimuli, weak gamma power and strong spike rates are observed (Angelucci et al., 2017; Gieselmann and Thiele, 2008; Peter et al., 2019; Uran et al., 2020).

## Origins of gamma oscillations

Neocortical gamma oscillations are believed to arise from the dynamic interplay of reciprocally connected excitatory (E) and inhibitory (I) neurons. According to the E-I model of gamma, also known as 'pyramidal-interneuron network gamma' (PING), an input drives a wave of fast excitation which is then followed within few ( $\approx$ 2-4) milliseconds by feedback inhibition. The interplay between E-I neuronal pools leads to an alternation of excitation and inhibition that gives rise to rhythmic gamma oscillations (Buzsáki and Wang, 2012; Whittington et al., 2000).

Studies in rodents, leveraging genetic tools, have sought to elucidate the role of specific interneuronal classes in the generation of gamma synchrony. Gamma synchronization seems to depend on the activity of Parvalbumin-Positive (PV), and as shown more recently, Somatostatin-Expressing (SOM), and Vasoactive Intestinal Peptide (VIP) (Buzsáki and Wang, 2012; Cardin et al., 2009; Veit et al., 2017; Veit et al., 2021). Currently, cell-type specific genetic tools cannot be readily applied to the NHP model, and it remains unclear whether similar results hold true in the primate brain. Most of our knowledge regarding the generation of primate gamma comes from electrophysiological recordings, often combined with anatomical findings and (non-cell-type specific) causal manipulations. Here, I summarize some key findings regarding the origin and the anatomical distribution of gamma in the primate visual cortex.

In awake primates, neocortical gamma oscillations originate in the cortex rather than the thalamus (Bastos et al., 2014). Electrophysiological recordings in different layers of primate V1 revealed that gamma power varies between layers: it is strongest in the superficial layers (L2/3) and present, though less pronounced, in the deep layers (L5/6), while it is almost absent in the input layer L4C (Fig. 1.2B) ((Xing et al., 2012); see also: (Gieselmann and Thiele, 2022; Roberts et al., 2013; van Kerkoerle et al., 2014)).

Horizontal connectivity has been suggested to play an important role in the generation of gamma oscillations (Vinck and Bosman, 2016). These long-range connections can integrate information over extended parts of the visual field and are thought to mediate the effects of near-SM (Angelucci et al., 2017). In primate V1, horizontal connections primarily connect cortical columns with similar orientation preference (Lund et al., 2003; Malach et al., 1993; Stettler et al., 2002). This orientation selectivity could explain the findings that gamma synchrony is higher in response to homogeneous gratings while it breaks for non-matching orientations in the RF center and RF surround (Gieselmann and Thiele, 2008).

In addition to the role of horizontal connections, recent studies highlighted the influence of cortical feedback in gamma power (Hartmann et al., 2019). Hartmann et al. (2019) reversibly inactivated large parts of area V2 through cooling while recording in V1 the electrophysiological responses to a grating. The inactivation of the V2-to-V1 feedback resulted in a significant reduction of visually-driven gamma oscillations in V1, while spike rates remained largely unaffected.

#### A potential role of gamma oscillations in neuronal plasticity

Despite extensive research on gamma oscillations across various brain areas and in the context of different cognitive and sensory processes (for a review, see Fries (2009)), their functional role remains a subject of active debate (Buzsáki and Wang, 2012). Among the many hypothesized functional implications, gamma oscillations have been suggested to facilitate neuronal plasticity.

Neuronal plasticity refers to the remarkable ability of the brain to adapt its activity and structure in response to experiences throughout life (Voss et al., 2017). Gamma oscillations have been suggested to support a type of synaptic plasticity called 'Spike-Timing-Dependent Plasticity' (STDP). STDP is critically dependent on the temporal relationship between presynaptic and postsynaptic spikes (Caporale and Dan, 2008; Markram et al., 2012). When a presynaptic neuron repeatedly fires just before the postsynaptic one, synaptic strength typically increases. Conversely, if the presynaptic neuron repeatedly fires just after the postsynaptic neuron, synaptic strength usually decreases (Caporale and Dan, 2008).

Oscillatory synchrony seems to fulfill key prerequisites for the induction of synaptic plasticity as it promotes the alignment of spikes in time and involves the repeated occurrence of "change-inducing activity patterns" (Singer, 2021). Gamma oscillations, in particular, have been suggested to facilitate neuronal plasticity by synchronizing presynaptic spikes within short time windows, allowing them to arrive almost simultaneously at their common postsynaptic target. This could in turn increase the likelihood of a postsynaptic discharge (Fries, 2009; König et al., 1996), which is essential for the induction of STDP (Fell and Axmacher, 2011; Griffiths and Jensen, 2023). In addition, phase synchronization in the gamma frequency range between pre- and post-synaptic targets could also lead to precise time relations between the spiking of the two populations which is also important for STDP (Fell and Axmacher, 2011).

In vivo, neuronal plasticity is often investigated by manipulating sensory inputs. This can involve the repeated pairing of two sensory stimuli in time (Caporale and

Dan, 2008) or the repeated presentation of a sensory stimulus while monitoring changes in neuronal activity and/or feature preference of the recorded neurons, which could indicate structural plasticity. The following sections review studies that investigate the plasticity of neuronal responses as a function of stimulus repetition.

#### Repetition-related plasticity of neuronal responses

Several studies indicate that our brain builds on the redundancy of the visual input by adjusting its responses to repeated stimuli. At a perceptual level, stimulus repetition can lead to behavioral improvements (Gotts et al. (2012); though, as explained below, this is not always the case). At a neuronal level, the neuronal activity in many brain areas of humans and NHPs undergoes significant changes with the repetition of a visual stimulus.

In particular, stimulus repetition typically leads to pronounced stimulus-specific decreases in hemodynamic responses (Sawamura et al., 2005), and spike rate responses (Brunet et al., 2014; Li et al., 1993; Miller et al., 1993; Peter et al., 2021), a phenomenon called 'repetition suppression' (Grill-Spector et al., 2006). Repetition suppression has been investigated across various timescales, with neuronal response decreases occurring over short periods (seconds to minutes; Sawamura et al. (2005); Sobotka and Ringo (1994)) and longer periods (hours to days; van Turennout et al. (2000)).

Besides the pronounced decrease in spike rates and hemodynamic responses, stimulus repetition is often accompanied by stable (Peter et al., 2021; Stauch et al., 2021) or even improved behavioral performance, a phenomenon known as 'repetition priming' (McMahon and Olson, 2007; Wiggs and Martin, 1998). This observation contrasts the findings from other cognitive domains, such as attention, which associate increased spike rates with better behavior performance (Gotts et al., 2012). This raises an interesting question: how could the reduced spike rates maintain or even improve their impact on postsynaptic targets?

Gotts et al. (2012) suggested that this combination of decreased neuronal activity and improved behavioral performance could "reflect some kind of improved efficiency" mechanism. Increased efficiency of the remaining spikes could arise through enhanced neuronal synchronization. As mentioned earlier, increased oscillatory power at the presynaptic level could enhance the synchronization of the remaining spikes. This could allow them to arrive almost simultaneously at the postsynaptic target, thereby increasing their likelihood to evoke a postsynaptic response.

Interestingly, gamma activity has been found to undergo significant changes in response to stimulus repetition. Repeated exposure to a visual stimulus leads to significant increases in gamma power in the macaque (Fig. 1.3A-B) (Brunet et al., 2014; Peter et al., 2021) and human visual cortex (Stauch et al., 2021). This increase is mostly evident beyond the first few (up to 10) stimulus repetitions and builds over the course of multiple repetitions (see discussion in Chapter 4) (Peter et al., 2021; Stauch et al., 2021).

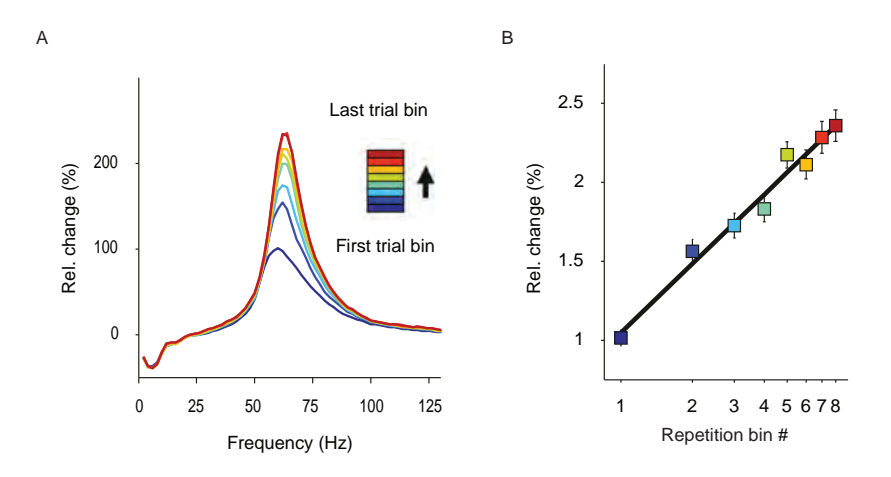


Figure 1.3. Repetition-related increase in LFP gamma power in macaque V1. (A) Power change relative to baseline in response to visual stimulation. Different repetition bins are color-coded as indicated in the figure. (B) Gamma power increases as a function of the number of repetition bins. Note that the x-axis is in logarithmic scale. Adapted from Brunet et al. (2014).

Recordings in the macaque brain revealed that the repetition-related increase in gamma was concomitant with a pronounced decrease in spike rates (Brunet et al., 2014; Peter et al., 2021). Yet, multi-unit activity (MUA) and putative interneurons exhibited increased synchronization in the gamma-band range (Brunet et al., 2014).

The repetition-related effects in gamma and spike rates are stimulus specific, i.e. they do not transfer to other (non-repeated) stimuli (Peter et al., 2021; Stauch et al., 2021). They are evident for gratings (Brunet et al., 2014; Peter et al., 2021; Stauch et al., 2021) and naturalistic images and are specific to the location where a stimulus was previously repeated (Peter et al., 2021).

#### Open questions on the repetition-related plasticity

To date, the mechanisms underlying the repetition-related changes in gamma and spike rates remain elusive. While the effects are well-documented in area V1

(Brunet et al., 2014; Peter et al., 2021; Stauch et al., 2021), their laminar specificity is unknown. Are the neuronal changes confined to specific layers or distributed across the cortical sheet? Understanding the laminar distribution of the effects could illuminate the local circuits that support these changes, offering insights into the mechanisms of neuronal plasticity in the early visual cortex.

Moreover, the stimulus specificity of the repetition-related effects has been exclusively tested with the repetition of stimuli designed to differ substantially between them (Peter et al., 2021; Stauch et al., 2021), Currently, it remains unclear if the stimulus specificity extends to stimuli that are more similar to each other.

Finally, the neuronal effects of stimulus repetition have only been studied with a limited number of interleaved stimuli (less than 4). What happens when more stimuli are interleaved? This question is crucial, as in our everyday life, we encounter a multitude of repeated visual stimuli that are processed by our visual cortex. Understanding these dynamics can provide deeper insights into how our brain adapts to complex visual environments.

#### Thesis outline

The first part of the thesis is inspired by the 3Rs, particularly focusing on the principles of reduction and refinement. Chapter 2 presents the refinement of chronic cranial implants for macague monkeys and their implantation techniques. It summarizes methodological improvements developed in the Fries lab over several years by various scientists, including myself. This chapter focuses on the development of cement-free modular implants and the refinement of implantation procedures. Presenting results from 12 macague monkeys implanted with similar methods, we demonstrate the suitability of these methods.

Chapter 3 explores the sample sizes that are traditionally used in NHP research and discusses the statistical inference derived from small samples, a topic often overlooked in the NHP literature. To enhance transparency, we estimate the typicality of an effect, i.e., its probability in the population, based on the number of animals showing an effect out of all tested animals.

Chapter 4 examines the effects of stimulus repetition on the neuronal responses of areas V1 and V2 of the macague brain. Using laminar electrophysiological recordings, this work aims to elucidate: 1) the laminar distribution, 2) the level of stimulus specificity, and 3) the robustness to set size of the repetition-related changes in gamma oscillations and spike rates.



# Chapter 2

# Modular, cement-free, customized headpost and connector-chamber implants for macaques

Published as: Psarou, E., Vezoli, J., Schölvinck, M.L., Ferracci, P.A., Zhang, Y., Grothe, I., Roese, R., and Fries, P. (2023). Modular, cement-free, customized headpost and connector-chamber implants for macaques. J Neurosci Methods 393, 109899.

#### Abstract

Neurophysiological studies with awake macagues typically require chronic cranial implants. Headpost and connector-chamber implants are used to allow head stabilization and to house connectors of chronically implanted electrodes, respectively. We present long-lasting, modular, cement-free headpost implants made of titanium that consist of two pieces: a baseplate and a top part. The baseplate is implanted first, covered by muscle and skin and allowed to heal and osseointegrate for several weeks to months. The percutaneous part is added in a second, brief surgery. Using a punch tool, a perfectly round skin cut is achieved providing a tight fit around the implant without any sutures. We describe the design, planning and production of manually bent and CNC-milled baseplates. We also developed a remote headposting technique that increases handling safety. Finally, we present a modular, footless connector chamber that is implanted in a similar two-step approach and achieves a minimized footprint on the skull. Twelve adult male macagues were successfully implanted with a headpost and one with the connector chamber. To date, we report no implant failure, great headpost stability and implant condition, in four cases even more than 9 years post-implantation. The methods presented here build on several related previous methods and provide additional refinements to further increase implant longevity and handling safety. Optimized implants can remain stable and healthy for at least 9 years and thereby exceed the typical experiment durations. This minimizes implant-related complications and corrective surgeries and thereby significantly improves animal welfare.

# Introduction

Understanding the primate brain requires neurophysiological studies with awake behaving macague monkeys. The majority of these studies so far requires head fixation that greatly eases the precise monitoring of eye position, and that is required for most recording approaches. The ability of head fixation also allows the experimenter to safely provide wound care to awake animals.

While conducting animal research, it is an ethical imperative to comply with the 3R principles: replacement, reduction, refinement. Refinement of procedures in the field of awake macague monkey research is particularly challenging, because most studies in the field typically include a very low number of animals. Therefore, even small refinements obtained in one laboratory should be shared and disseminated. This could help many researchers refine their techniques and promote the welfare of many experimental monkeys.

Research on the neural substrate of many higher cognitive functions builds on the ability of macaque monkeys to perform complex cognitive tasks. Such tasks often require extended training periods that can last up to several months. Moreover, in the case of studies with awake macagues, refinement can also lead to reduction. Given their long lifespan, one animal can often participate in several subsequent projects as long as the animal and the implants are in good health. Therefore, there is great need for long-lasting implants that can stay healthy over extended time periods.

In the last two decades, there has been a considerable effort to refine headpost implants and their implantation techniques. Several improvements have led to higher success rates and longer implant lives, e.g. through the customization of implant shapes (Adams et al., 2007; Chen et al., 2017; Overton et al., 2017), the use of more biocompatible materials (Adams et al., 2007; Lanz et al., 2013; Overton et al., 2017), the use of coatings to enhance osseointegration (Chen et al., 2017; Lanz et al., 2013), or the use of two-step implantation approaches (Betelak et al., 2001; Blonde et al., 2018). Here, we present our approach that builds on previously reported methods (Adams et al., 2007; Johnston et al., 2016; Lanz et al., 2013; Overton et al., 2017), and we describe additional refinements to the entire head fixation technique, including the implant itself, the surgical procedures and the everyday handling. We also present a connector-chamber implant that houses chronic electrode connectors. This connector chamber is inspired by our headpost approach and aims to reduce the overall footprint of the implant on the skull, and to facilitate its osseointegration.

Briefly, 1) we developed long-lasting modular implants that are implanted in a refined two-step approach, 2) we provide detailed protocols of our implant design, planning and production procedures, and of our implantation techniques, 3) we share the 3D models of the implants and tools we developed, so any lab can reproduce them, and 4) we present the results from twelve adult male macaque monkeys that were implanted with these techniques. Importantly, we experienced no implant failure and found the implants to last up to more than 9 years, i.e. until today.

### Materials and methods

#### **Animals**

Twelve male monkeys (Macaca mulatta) were implanted with headpost implants (see details in Table 2.1) and one with the connector chamber (Monkey C). All procedures and housing conditions complied with the German and European law for the protection of animals (EU Directive 2010/63/EU for animal experiments). All surgical and experimental methods were approved by the regional authority (Regierungspräsidium Darmstadt) under the following permit numbers: F149/01, F149/07, F149/08, F149/1003, F149/1007, F149/1008, F149/1010, and F149/2000.

# A two-piece headpost

We developed a cement-free, two-piece headpost that consists of a baseplate and a top part that are implanted in two separate surgeries. Figure 2.1 presents a graphical overview of our headpost methods. The baseplate is implanted first (Fig. 2.1A). It is customized to follow the skull surface of the individual monkey and is anchored onto the bone exclusively by means of titanium bone screws. The screw length is adjusted to match the skull thickness. At the end of this surgery, the baseplate is covered with muscle and skin, and the surgical site is allowed to heal for several weeks. During this period, the sterile conditions established by the closing of the skin provides optimal conditions for osseointegration. Following an adequate waiting period (see section 'Waiting time between surgeries'), the percutaneous part of the implant is added (Fig. 2.1B). In a short surgery, the central plate of the baseplate is exposed, and the top part is secured onto it using a screw (top-part screw). Finally, we also developed a headpost holder that allows remote headposting for increased safety during monkey handling (Fig. 2.1C).

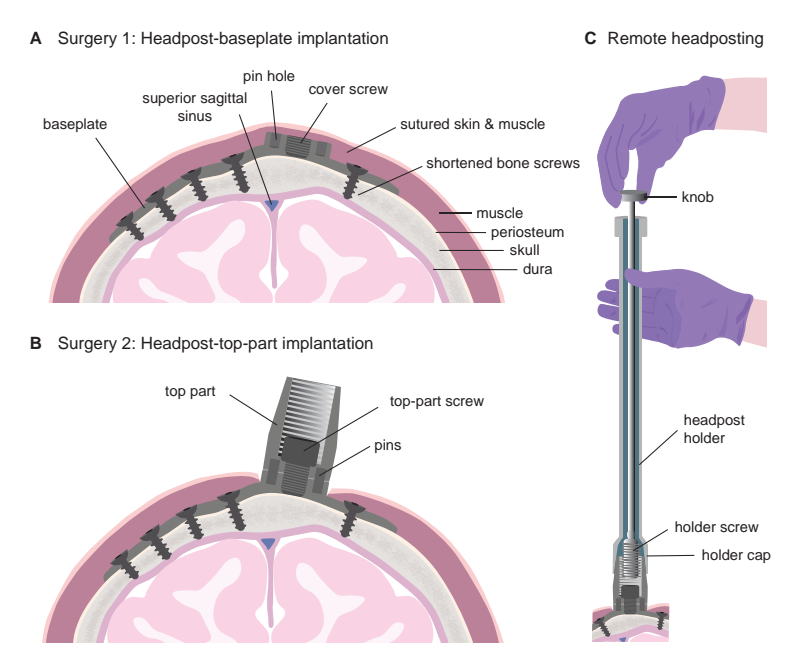


Figure 2.1. Illustration of headpost methods. (A) The baseplate is implanted first, secured to the skull with titanium bone screws, whose length has been adjusted to match the underlying bone thickness. At the end of this surgery, the baseplate is covered with muscle and skin, and the surgical site is allowed to heal for several weeks. (B) The top part is added in a separate short surgery. A circular cut is performed and the top part is secured onto the baseplate with a central screw. Two pins prevent the top part from rotating. (C) The headpost holder allows the experimenter to remotely fixate the animal's head. By turning a knob at the proximal end of the headpost holder, the holder screw at the distal end enters into the thread of the top part and thereby fixes the holder to the implant.

**Table 2.1.** *Monkey Information.* 

Monkey	Age*(year)	Weight* (kg)	
Monkey L	8	11.0	
Monkey Sk	8.8	11.5	
Monkey D	8.7	8.3	
Monkey G	8	11.2	
Monkey Hu	7	11.5	
Monkey Ch	12.3	16.0	
Monkey T	7.9	13.1	
Monkey St	12.5	15.0	
Monkey M	6.9	11.9	
Monkey H	15.4	15.0	
Monkey C	15.3	14.0	
Monkey K	15.4	13.0	

<sup>\*</sup> At the time of the headpost baseplate implantation. Animals are listed in the order of implant longevity until today or until sacrificed or deceased, as listed in Table 7.

#### **Headpost baseplate**

Two baseplate versions were used that differed in how they were shaped to follow the skull surface: one version was computer-numerical-control (CNC) milled in a flat shape and then customized by manual bending (referred to as "bent version", Fig. 2.2A); another version was CNC-milled directly to follow the skull shape (referred to as "milled version", Fig. 2.2B-C). Both versions are based on an overall similar design. Nine monkeys have been implanted with the bent version and three with the milled one (Table 2.2).

Both versions were produced from titanium Grade 2. The advantage of the bent version is that it is easy, cheap and fast to produce in larger numbers, and can be shaped to the individual skull of a monkey whenever its implantation is planned. The flat precursor of the bent baseplate (Fig. 2.2A) can be produced on a 3-axis CNC machine. The advantage of the milled version is that it provides a near perfect fit to the skull (Fig. 2.2B-C), which cannot be achieved by manual bending. The milled baseplate requires a 5-axis CNC-milling machine.

The baseplate contains a central plate, onto which the headpost top part is later mounted, and several "legs" that extend radially from this plate. The overall shape of the baseplate with its legs varied depending on the brain areas of interest. As described in Table 2.2, ten monkeys were implanted with a baseplate in the most anterior part of the skull (frontal version), and two with a more centrally located implant (central version).

The frontal baseplate version (Fig. 2.3A) was designed to allow later access to almost the entire left hemisphere (except the most frontal areas), and to occipital, temporal and part of parietal areas on the right hemisphere. The central version (Fig. 2.3B) was designed to allow later access to both frontal and occipital areas of the left hemisphere, and to occipital areas of the right hemisphere.

In planning the baseplate position and implantation, one needs to consider the underlying anatomy. The most anterior legs of the frontal baseplate version ran parallel to the supraorbital ridge, and we chose to have them run several millimeters behind this ridge. This had several reasons: 1) Screws placed even further anterior can connect to the frontal sinus, which can be a source of infection (though we note that several other labs have successfully implanted similar designs on top of the frontal ridge: Lanz et al. (2013), Overton et al. (2017), Adams et al. (2007), Adams et al. (2011), Ortiz-Rios et al. (2018)); 2) This position avoids the screws entering the eye socket; 3) This position coincides with the coronal section through the skull

with a particularly small radius, whereby the baseplate legs can "grab" particularly effectively around the skull, which in turn provides optimal anchoring in the bone at a relatively large angle relative to the pulling force on the headpost (note the two most lateral bone screws in Fig. 2.4C-D). The leg extending in the anterior-posterior direction, along the midline, was always placed slightly away from the midline, in order to avoid the screws damaging the superior sagittal sinus.

An earlier version of the frontal baseplate was anchored to the skull with twelve bone screws (Monkey Sk, Monkey D and Monkey T). Later, one screw hole was removed from the leg running between the most anterior and the one parallel to the midline. This allowed access to more brain areas of the right hemisphere. Nine monkeys received a baseplate with eleven bone screws.

#### **Headpost top part**

The headpost top part (Fig. 2.2A and 2.2C) is a separate CNC-milled piece (requiring 3 or more axes), made of titanium Grade 5, which is mounted on the baseplate (made from titanium Grade 2) in a second surgery. It is the percutaneous part of the implant that can be secured by the headpost holder to allow head fixation. The top-part is fixed to the central plate of the baseplate with a commercially available screw of size M5, whose head diameter is reduced in-house to fit within the top part. We refer to it as 'top-part screw' and it is also made of titanium Grade 5. Two stainlsess steel pins on opposite sides of the base of the top part fit into respective pinholes on the central plate of the baseplate (Fig. 2.2A). Those pins allow to define the precise orientation of the top part before its implantation, and they prevent any rotation of the top part after implantation. Due to a problem that occurred in one animal (see Results, section 2.3), we added two additional, spare, pin holes on the baseplate.

As can be seen in Figure 2.2C, the top part contains on its inside a 9 mm diameter hole with a screw thread, and on its outside a hexagonal surface that narrows conically towards the top. These features allow a connection to the headpost holder, as described below under section 'Headpost holder'.

#### Skull reconstruction

The implant planning starts with the acquisition of a preoperative computerized tomography (CT) scan in order to create a precise model of the individual animal's skull. The 3D model is then printed and used to guide individualized implant planning and production. Even though a skull model can be extracted from MRI

#### A Two-piece headpost

Bent baseplate







B CNC-milled baseplate on skull replica



C CNC-milled baseplate and top part on skull replica



Figure 2.2. The modular headpost implant. (A) The main parts of the headpost are shown: on the left, a baseplate (flat precursor of bent version shown as example) with the cover screw, and on the right, a top part and the titanium screw that secures the two parts together (top-part screw). (B) The CNC-milled version of the baseplate (frontal version) is shown on top of the 3D printed skull replica of Monkey H. (C) The top part is added on the baseplate.

scans, CT scans provide more precise information about the bone structure, yielding to an easier and more detailed skull reconstruction.

The scan is performed under ketamine-medetomidine anesthesia and in case the animal is placed in a stereotaxic frame, the anesthesia is combined with NSAIDs and the application of lidocaine ointment on the tip of the ear-bars. Seven monkeys were scanned in a Brilliance 6 scanner (Philips, Amsterdam, Netherlands) and five in a ProMax 3D Mid scanner (Planmeca Oy, Helsinki, Finland). For a detailed summary of the scanning parameters used per monkey refer to Suppl. Table 2.1.

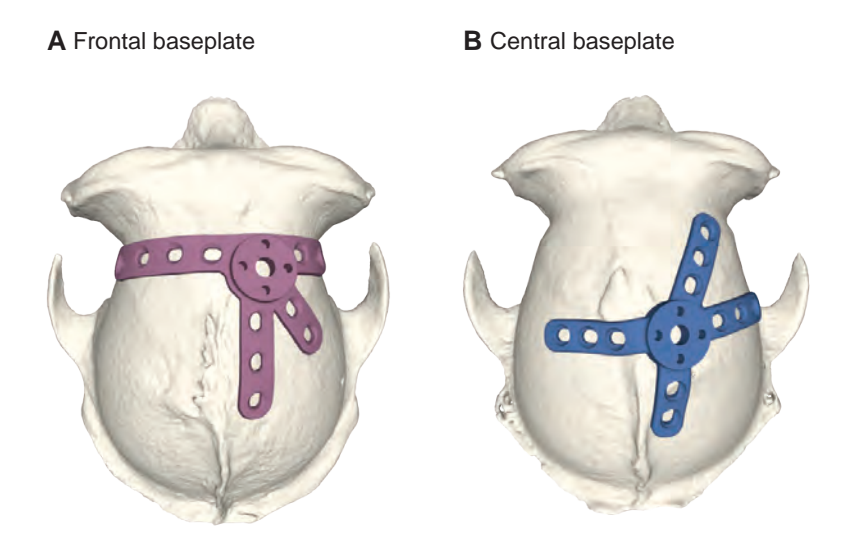


Figure 2.3. Versions of the CNC-milled headpost baseplate. (A) A frontal baseplate (Monkey H) and, (B) a central baseplate (Monkey C) allow access to different brain areas.

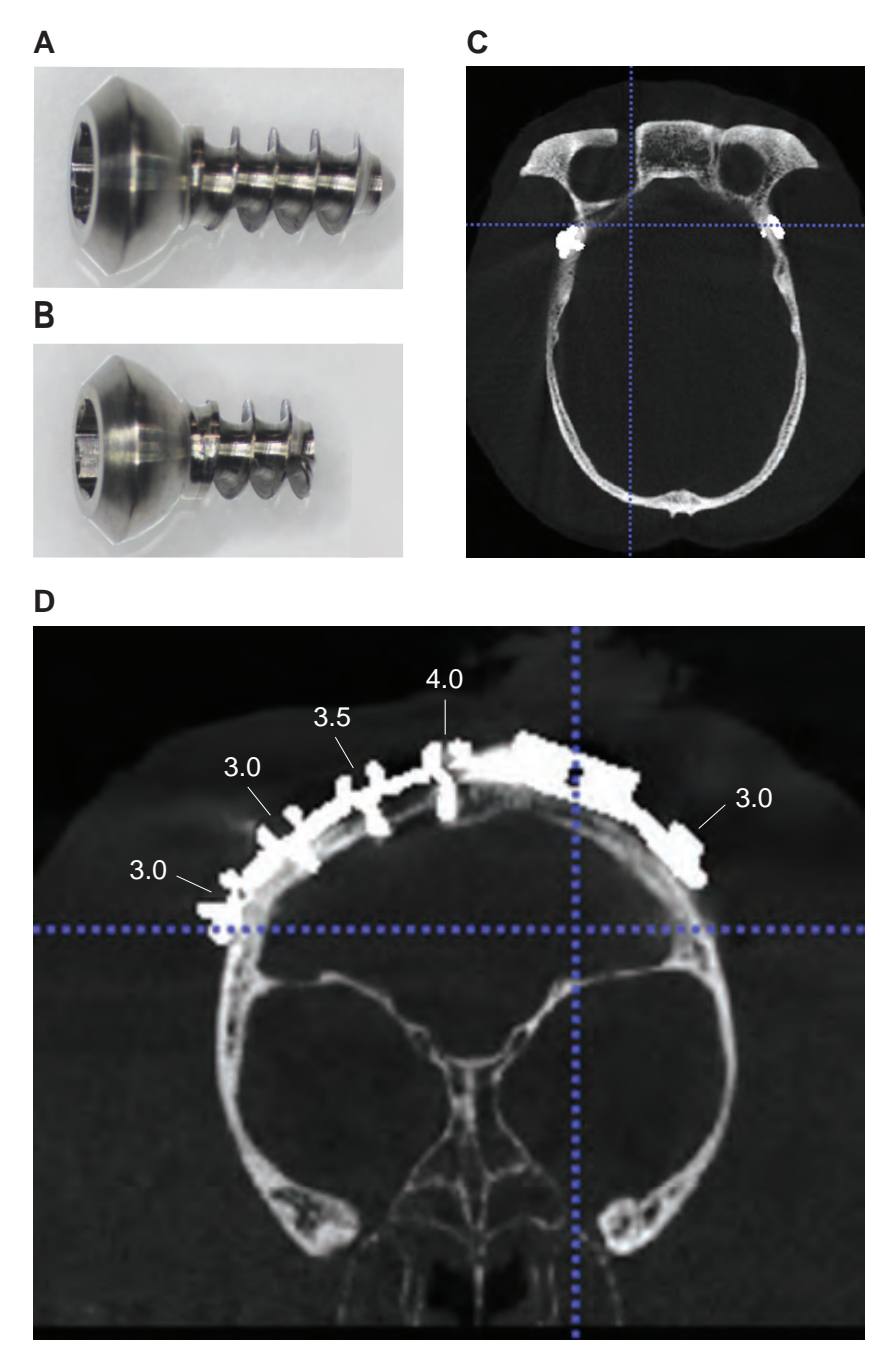


Figure 2.4. Length-adjusted bone screws. The original self-tapping, titanium bone screws (A) were cut (B) in order to match the thickness of the underlying bone. (C-D) Post-operative CT scan of Monkey St that shows the successful choice of screw lengths at the anterior legs of the baseplate implant. The thread length of the adjusted screws is indicated. Panel C shows the thread of the two more lateral screws of which the head is obvious in D.

**Table 2.2.** Software used for the planning of the headpost baseplate.

Monkey	Software	<b>Baseplate Version</b>
Monkey L	Brain Voyager QX	bent, frontal
Monkey Sk	BrainVoyager QX	bent, frontal
Monkey D	BrainVoyager QX	bent, frontal
Monkey G	Brain Voyager QX	bent, frontal
Monkey Hu	Brain Voyager QX, Image J	bent, frontal
Monkey Ch	Brain Voyager QX, ImageJ	bent, frontal
Monkey T	Brain Voyager QX	bent, frontal
Monkey St	3D Slicer 4.10.0	bent, frontal
Monkey M	Brain Voyager QX, ImageJ	bent, frontal
Monkey H	3D Slicer 4.10.0, Geomagic Design X, SOLIDWORKS	milled, frontal
Monkey C	3D Slicer 4.10.0, Geomagic Design X, SOLIDWORKS	milled, central
Monkey K	3D Slicer 4.10.0, Geomagic Design X, SOLIDWORKS	milled, central

The ProMax is a CBCT (Cone Beam Computed Tomography) scanner typically used in dentist and ear-nose-throat applications, where it provides an extended view of the maxillo-facial region. We used a slightly adapted version of such a system to obtain CTs of nearly the entire macaque skull in one volume. The system has a similar size as a surgical microscope, and is similarly mounted on a mobile platform and can thereby be easily used in a research setting (though the room needs to be specially equipped for the use of X-ray radiation). After positioning of the animal, the CT measurement is obtained within less than one minute; the calculation of the CT reconstruction on a regular PC takes few minutes.

To make optimal use of the high resolution of the CT scans, we recommend to place the animal's head into a stereotaxic frame. Also, such a frame provides ear bars and eye bars. The presence of ear bars in the CT images can be helpful in the determination of the inter-aural line (an imaginary line connecting the tips of the ear bars). The eye bars are used to define the inferior-orbital ridge. The inter-aural line together with the inferior-orbital ridges can be used to define the orbitomeatal plane, also referred to as Frankfurt baseline plane (Dubowitz and Scadeng, 2011) or Frankfurt zero plane. In the Brilliance 6 scanner, the head can be positioned in an MRI compatible stereotaxic frame that allows artifact-free CT scans.

In the ProMax (Planmeca) scanner, we have typically used a custom-built stereotaxic frame. This stereotaxic frame positioned the head above the lateral bars, which allowed the CT scan to contain most of the skull. The resulting volume did not reach down to the skull base, but it did contain all skull features relevant for the Frankfurt-zero alignment, namely the ear canals, the occipital ridge, and the complete eye sockets including the lower margin of the eye socket (see example scan in Fig. 2.4C-D). We strongly recommend to place a CT-visible marker on one side of the animal's head to avoid ambiguities with regard to the orientation of the images (see MRI-marker in Fig. 2.5A-C). We used one of the CT-visible markers that came with the MRI-compatible stereotaxic frame (see next paragraph).

As mentioned above, the ear bars of the stereotaxic frame can be used in determining the interaural line in the CT scans. The commercially available ear-bars of our MRI-compatible stereotaxic frame (Model 1430M MRI Stereotaxic Instrument, David Kopf instruments, Los Angeles, California, USA) were made of polyetherimide (PEI) which does not produce artifacts. However, the PEI also does not provide very good X-ray contrast (Fig. 2.5A-B), and the tips of the ear bars were relatively blunt/round (Fig. 2.5A-B), and not identical to the ear bars used later during implantation surgeries. Therefore, we used the opportunity to exchange the tips on those ear bars. We exchanged the tips with custom-built tips made of aluminum. The aluminum gives excellent X-ray contrast (Fig. 2.5A and 2.5C), and at the same time minimizes stray artifacts, and it was easy to produce tip diameters optimized for monkey ear canals and identical to those used during implantation surgeries. The use of identical tip diameters during CT scanning and surgery improves the alignment between the two head fixations.

From the CT based 3D volume, the skull was segmented using either Brain Voyager QX (Goebel et al., 2006) or 3D Slicer (Fedorov et al., 2012). Table 2.2 summarizes the software packages used per monkey for implant planning.

### Baseplate shaping to the skull

#### Shaping of the baseplate with manual bending

A 3D printed replica of the monkey's skull is used as template in order to prepare the manually bent baseplate preoperatively (for a similar approach see Overton et al. (2017)).

In the case of the anterior baseplate version, simple landmarks on the skull (like the supraorbital ridge and midline) can be used to guide the positioning of the implant. We used a simple paper version of the baseplate. We placed this paper onto the 3D skull replica and gently pushed it down, so it adapted to the shape of the skull. We then shifted it around to find the optimal position. In doing so, we took into account the considerations mentioned above, under section 'Headpost baseplate', namely

1) that the baseplate optimally "grabs" around the part of the skull with a relatively small radius, and 2) that the screws avoid the supraorbital ridge (and thereby the underlying sinus), the eye sockets, and the superior sagittal sinus in the midline. Note that we did not attempt the central plate to be positioned precisely on the midline, which would allow a vertical top part (see section 'Future refinements').

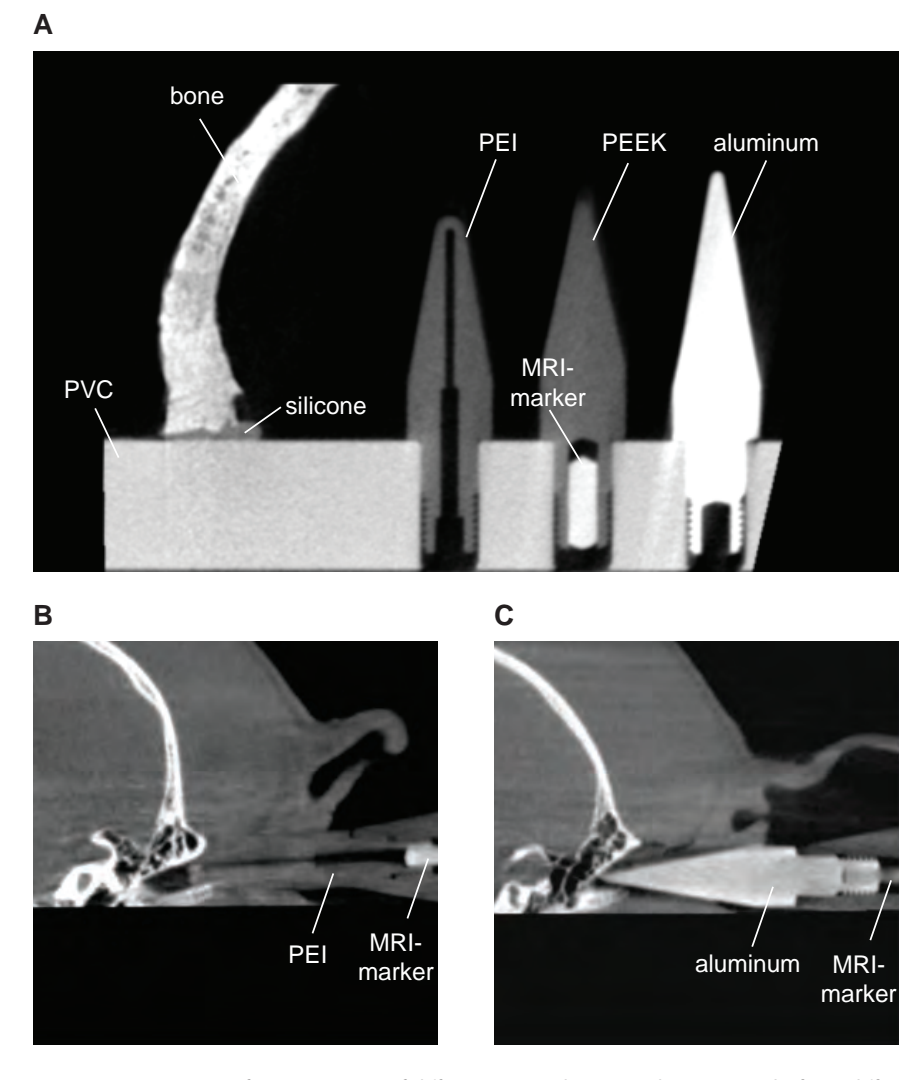


Figure 2.5. Comparison of X-ray contrast of different materials. (A) Ear-bar tips made from different materials and skull bone are shown for comparison. Aluminum gives stronger X-ray contrast compared to polyetherimide (PEI) and polyether ether ketone (PEEK). (B) CT scan of Monkey St with the PEI ear bar. (C) CT scan of Monkey C with the aluminum ear-bar tip mounted on the handle of the MRI-compatible PEI ear bar. The MRI marker was placed on one side only, to avoid ambiguities in the left-right orientation of the CT images.

Once the final location had been decided, an outline of the baseplate was drawn on the skull replica that later on guided the manual bending of the titanium implant. Careful bending of the baseplate legs to achieve an optimal fit can take up to several hours. For this reason, this procedure should be completed before the surgery. It is also much easier and safer to handle and bend the implant in a non-sterile setting. For the manual bending, we used tools from DePuy Synthes (Raynham, MA, U.S.A; see Suppl. Table 2.2).

The bending starts with the part of the legs proximal to the central plate. Once the proximal parts of each of the legs have been bent to fit to the skull as good as possible, bending proceeds to more distal parts of the legs. Each step of the bending procedure should progressively approximate the optimal shape in small steps, rather than using multiple forward-backward bends, which can lead to material weakening and breakage. In doing so, the baseplate will need to be repeatedly placed against the skull replica to visually check its fit.

We found that the central plate with the most proximal parts of the legs constitute a relatively large part that cannot be bent and sufficiently adapted to the skull, such that gaps of 1-2 mm in some animals could not be avoided. This and an improvement of the overall fit to the skull were the main motivations to move to the milled baseplate, described in the next paragraph.

#### Shaping of the baseplate with CNC-milling

Three monkeys were implanted with baseplate implants that were shaped to follow the individual skull geometry using CNC-milling (Table 2.2). Similar to the bent version described above, also the milled baseplates feature 1) four radially extending legs with eleven screw holes and, 2) a central plate that allows the top part to be mounted on it (the top part is identical to the one used with the manually bent baseplate).

Monkey H was implanted with the frontal version of the CNC-milled baseplate (Fig. 2.3A). While planning this implant, we aimed to produce a baseplate with similar design to the bent frontal version. To this end, our first implant planning steps were identical to the planning of the bent version (see section 'Shaping of the baseplate with manual bending'): the implant location was chosen using the skull replica and a paper version of the baseplate. The outline of the baseplate and each screw hole was then drawn onto the skull model. At this stage, one needs to translate the implant location into coordinates on the skull segmentation that can subsequently guide the implant design in the planning software. To do so, we

drilled small holes into the 3D skull replica at the center of each screw hole and then acquired a CT volume of it. In the resulting volume, one could easily see the screw holes. This volume was then aligned to Frankfurt-zero and segmented. By overlying this model with the segmentation obtained from the original CT-volume of the monkey's head, we could infer the target location of each screw and thus, the overall location and shape of the implant legs. Note that Ahmed et al. (2022) present a way to perform virtual bending of a headpost implant that could simplify this procedure.

Monkey C and Monkey K were implanted with a central CNC-milled baseplate version (Fig. 2.3B) whose position and shape were planned in a different way. First, the coordinates of the brain areas of experimental interest were estimated in the skull segmentation, and then the baseplate legs were designed to allow later access to those areas

In all cases, the skull was segmented from the CT volume using 3D Slicer (Fedorov et al., 2012). The resulting skull model was imported into the Geomagic Design X software (https://www.oqton.com/geomagic-designx/) for further processing that facilitated the overall planning procedure. An area of interest on the skull was chosen and isolated (Lasso selection). Then, the isolated surface was fitted with a mesh using the function "Mesh Fit".

An alternative to the Geomagic Design X software might be the FreeCAD software, an open-source parametric modeler (https://www.freecad.org/). It has not been used in the current experiments, but offers similar functionality. FreeCAD can be used for repairing and smoothing mesh data (with the "Mesh Workbench"), fitting a parametric surface to the skull model (with the "Surface Workbench"), and creating parametric models of solid parts (with the "Part Design Workbench"). Note that FreeCAD can also be an alternative for the SOLIDWORKS software.

In the case of Monkey C and Monkey K, two surfaces were created: a) a detailed one that closely follows the geometry of the skull (resolution by allowable deviation: 0.1 mm) and, b) a smoother version of it (allowable deviation: 1 mm). These two reconstructed surfaces were exported as parasolid surfaces which were then imported into SOLIDWORKS and used for the next planning steps. The detailed one was used to create the lower surface of the baseplate which provided a near perfect fit of the implant to the skull. The upper surface of the implant legs was based on the smoothed surface plus an offset to realize the thickness of the legs. This procedure led to uneven thickness along the implant legs (Table 2.3; Monkey C, Monkey K). To avoid weak points on the implant, the thickness of very thin parts was increased so that it was always more than 1.26 mm.

In the case of Monkey H, only the detailed surface was used for the implant planning. An offset was applied on this surface in order to achieve the desired implant thickness, and then, its upper surface was smoothed to avoid sharp features that could irritate the overlying muscle or skin.

### CNC-milling of the headpost baseplate

The CNC-milled headpost baseplates were in-house produced using a 5-axis CNC machine. During this process, material is progressively removed from a block of titanium until the final result is achieved. A crucial step is the clamping and thus, proper fixation of the titanium block throughout the milling procedure. We devised two different clamping approaches illustrated in Suppl. Fig. 2.1 and Suppl. Fig. 2.2, respectively. We recommend the approach illustrated in Suppl. Fig. 2.2, because it avoids the need to plan and mill an extra piece, and it avoids potential imprecisions incurred by re-clamping (see Suppl. Fig. 2.1 legend for details).

Baseplate version	Implant thickness (mm)			
	Leg		Central plate	
	min.	max.		
bent	1.70	1.70	4.5	
milled, Monkey H	1.70	1.75	3.6	
milled, Monkey C	1.67	2.80	4.0	
milled, Monkey K	1.26	2.50	4.0	

**Table 2.3.** Thickness of the different headpost baseplate versions.

## Planning and preparation of bone screws

The baseplate is secured to the skull only by means of titanium screws. Eleven monkeys were implanted with commercially available screws (Crist Instrument Company, Inc., Hagerstown, Maryland, USA) and one (Monkey Ch) with in-house made titanium bone screws.

The commercially available bone screws (Table 2.4) came with a total length of 8.1 mm, a thread length of 5.5 mm and a thread diameter of 2.6 mm. In our experience, the bone at many parts of the macague skull can be thinner than 5.5 mm. Therefore, in nine monkeys, we used the procedure described in the following.

We determined the optimal length of each screw preoperatively. This allowed to preadjust a drill stop for each screw (see below), and it removed the need to manually measure the bone thickness during the surgery. This screw-length adjustment was done on a lathe. Figure 2.4 (A-B) shows an original and an example shortened screw. We prepared screws with several thread lengths, from 3 mm to 5.5 mm, in steps of 0.5 mm. For each screw position, we used the CT to estimate the bone thickness (see below for more details), and used the next longer available screw length.

Importantly, even though the original tip of the screw was removed, we were still able to use these screws as self-tapping screws. However, it should be noted that the first few turns are more difficult than with un-modified screws, and special attention is required to make the screw find its way into the pre-drilled bone hole and to make sure the screw thread starts cutting into the bone. It might be helpful to practice this on a skull of a cadaver.

To measure the bone thickness for each screw location, the screw positions need to be defined in the CT reconstruction of the skull. For the milled version, one can directly overlay, in the planning software, the baseplate model with the skull reconstruction, and measure the bone thickness at each screw hole.

For the bent baseplate, different strategies can be used in order to infer the planned position of the screws. Following baseplate bending, one can mount the skull replica in the stereotaxic apparatus and measure the stereotaxic positions of the screw holes. The bone thickness can then be measured in the planning software at these pre-specified locations, after alignment of the skull reconstruction to the stereotaxic Frankfurt-zero. These measurements were done using one of the following software packages (see Table 2.2): 3D Slicer (Fedorov et al., 2012), Brain Voyager QX (Goebel et al., 2006), or ImageJ (Schneider et al., 2012).

One can also use the skull replica and the drawing of the baseplate outline to estimate the general location of the implant. Using landmarks on the skull, one can infer the respective CT slice and rough location of the screw. We have noticed that in most parts of the skull, the bone thickness changes smoothly, such that an approximate estimate of the screw position is sufficient.

Note that the measured bone thickness should then correspond to the length of the screw that extends below the baseplate leg into the bone; if at a particular screw position, the baseplate could not be perfectly adapted to fit the skull (primarily with the bent version), this distance needs to be added to the screw length.

## A two-step implantation approach

## **Headpost-baseplate implantation**

For the baseplate implantation, following general anesthesia induction, the monkey is intubated and placed into the stereotaxic apparatus. The skin is shaved, thoroughly disinfected and the surgical site is surrounded with sterile drapes. Different approaches can be used in order to find the target location. For the milled baseplate, the stereotaxic coordinates are simply read from the CAD drawings. For the manually bent baseplate, a 3D printed skull replica can be fixed in a stereotaxic apparatus to read off the corresponding coordinates. Note that both approaches provide an initial positioning, yet the final adjustments (millimeter or less) are done manually in order to achieve the best fit to the underlying bone.

Another option is to use anatomical landmarks palpable through the skin for the approximate estimation of the position. For example, the frontal baseplate version is close to the supraorbital ridge. The distance from the supraorbital ridge to the intended position can be measured pre-surgically on a skull replica. In the surgery, the supraorbital ridge can be palpated, and the intended position thereby found.

Note that the baseplate is manually bent or directly milled to fit the skull, but the skull is covered with substantial muscle and skin, such that the baseplate seems to not fit until skin and muscle are removed.

Once the approximate baseplate position has been found, a sterile pen is used to draw a line on the skin to guide the skin cut. For frontal implants, a coronal incision is made that is placed about 1.5-2 cm posterior to the intended position of the central plate, to minimize the overlap between the later suture line and the implant. The skin is cut down to the fascia using a scalpel.

We use a periosteal elevator to detach the muscle from the skull (Fig. 2.6A), starting at its middle and frontal insertion and then working lateral and posterior. We minimize muscle detachment to the area covered by the baseplate legs and central plate. To this end, we repeatedly insert the baseplate underneath the partly detached muscle, onto the bone, to test whether muscle detachment is sufficient. Note that the periosteal elevator is only used to detach the muscle from the periosteum. In other surgeries, these instruments are typically used to clean the skull from the periosteum. However, in the baseplate implantation, we try to keep the periosteum intact, since it is the source of bone growth, respectively regrowth (Lin et al., 2014). It is crucial to keep the fascia and the skin moist during the whole procedure. They can be covered with gauzes that are regularly flushed with sterile saline.

Once the skull is exposed, the baseplate position can be tested. Both the manuallybent and the milled baseplates fit so well to the skull that their final position is obvious simply from their fit. This is particularly evident for the milled baseplate. We experienced that even careful stereotaxic positioning was not able to place the baseplate into the position of optimal fit to the bone; therefore, after stereotaxic positioning, and drawing the pre-final position onto the bone, we removed the baseplate from the stereotax and left the final, minute, adjustment to the fit between implant and bone.

In case that parts of the underlying bone show sharp features (typically at the medial ridge), a small part of the bone can be slightly smoothed away by drilling. Unless really necessary, this step is avoided and the bone is kept as intact as possible. Note that these sharp features are typically visible in the CT. They can be taken into account during the planning procedure (only realistic for the milled version), or they need to be drilled away during the surgery.

In Monkey St, the medial ridge was very pronounced, which would have made it difficult to obtain a good fit of the bent baseplate. Therefore, during preparation of the bent baseplate, we smoothed the medial ridge of the skull replica using an electric drill (see Table 2.4). During the implantation surgery, we drilled the corresponding part of the bone ridge; to avoid removing too much of bone, this was done in several small steps, interleaved with fitting the implant to the skull, until the fit was optimal.

Once the optimal fit between baseplate and bone is found, the surgical assistant fixes the baseplate in this position by firmly pressing onto the central plate, and the surgeon adds the bone screws one by one. The bone screws are placed insideout, i.e. starting with the screws close to the center (Fig. 2.6B-E) and then moving peripheral on the legs of the baseplate. Special care should be taken to insert the bone screws perpendicular to the skull surface to achieve the best possible grab and longer interaction surface. The bone holes for the screws are drilled with a manual hand drill combined with a drill stop (Fig. 2.6B) that prevents accidentally drilling too deep. The following procedure is followed:

1. We prepare the drill stop to accommodate the thickness of the baseplate. The length of the exposed drill is adjusted to correspond approximately to the

- thickness of the baseplate plus the expected skull thickness at the targeted screw position. In this, we take a conservative approach, aiming at leaving a very thin bone layer at the bottom of the drill hole.
- 2. The baseplate is positioned in its final position as explained above, and the drilling takes place through the holes of the baseplate. With the adjusted screw lengths, and the correspondingly adjusted drill depths, we found that we typically left the inner corticalis layer of the skull intact. This cautious approach has not led to any screw loosening (see Results, section 2.3).
- 3. We drive the screw into the bone and initially tighten it only loosely (Fig. 2.6C-E).
- Once all screws are in place, they are fully tightened (Fig. 2.6F). 4.

The screw hole in the central plate of the baseplate is then blocked with a cover screw (Fig. 2.6F-H) that prevents bone growth within it. One should make sure that this screw is sufficiently tightened against the bone, 1) to avoid that the screw is getting loose under the closed skin, 2) to ensure that the whole length of the screw hole is covered in order to prevent the bone from growing into this area.

When all bone screws are tightened and the cover screw is in place, the fascia and muscles are brought back above the baseplate and sutured together (Fig. 2.6I). In our experience, covering the implant with the fasciae and muscles improves the healing and prevents potential skin retraction following the later top-part implantation. The animals used in our experiments had guite extensive muscles, and this might have contributed to successful healing by forming a buffer between titanium and skin. Finally, the skin is sutured and the monkey stays on antibiotic treatment and painkillers for the following days. Table 2.4 summarizes the implant parts and special instruments that are used in the baseplate implantation.

|--|

Implanted parts	Material	Production/ source
Baseplate	titanium Grade 2	in-house
self-tapping bone screws	Titanium	Crist Instrument
cover screw	stainless steel, A2	commercially available
Implantation instruments	Specifications	
manual drill system: manual drill & drill guide with stop	Ø1.8 mm drill bit	DePuy Synthes
electric drill (in case of bone smoothing)	electric pen drive, Ø3-4 mm drill bit	

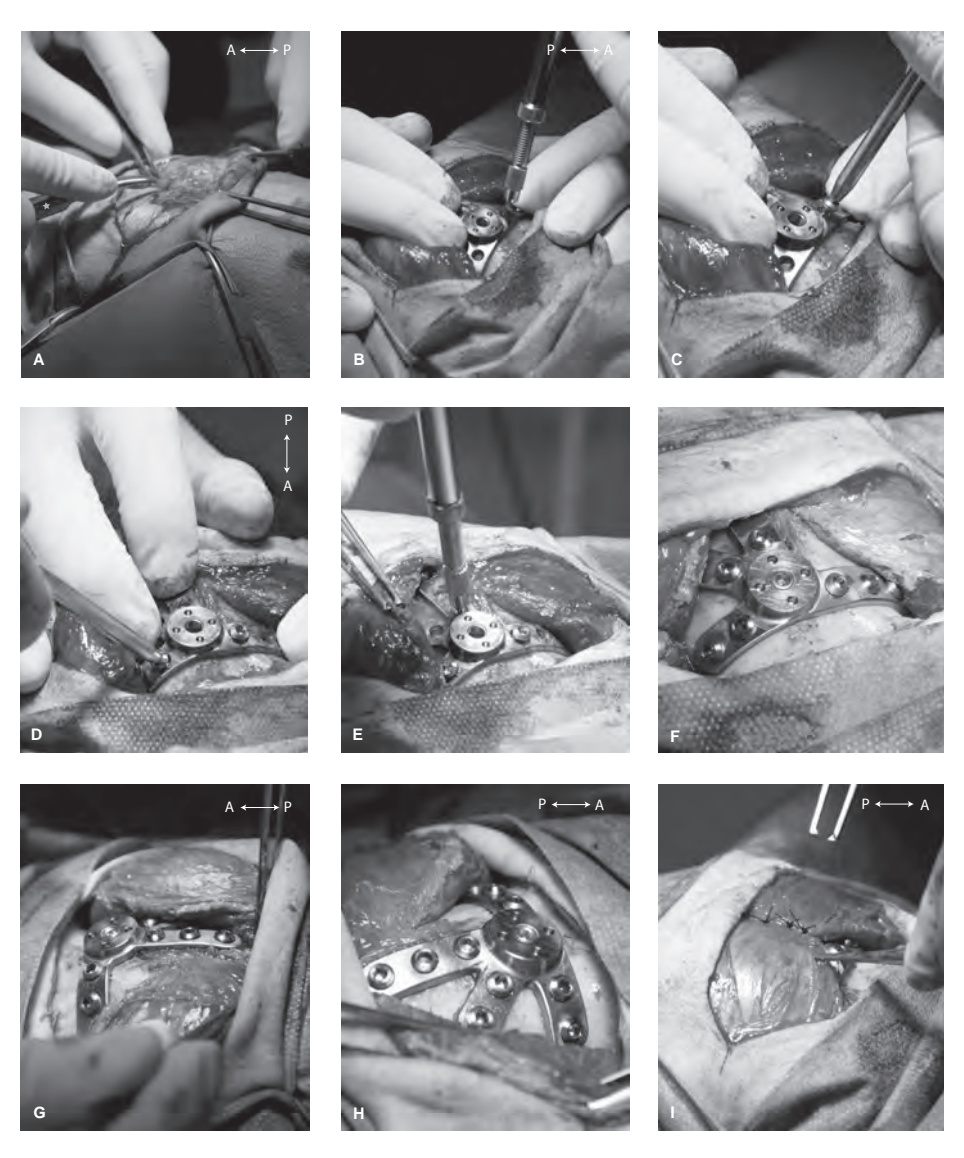


Figure 2.6. Implantation of headpost baseplate. (A) The skin is cut and the muscle is detached laterally to expose the skull. (B) When the implant position is found, the assistant firmly holds the baseplate onto the final location, and the surgeon drills the first bone hole using a manual drill combined with a drill-stop. (C) The first bone screw is placed, and the same procedure is followed for each screw (D-E). Generally, the central screws are placed first, followed by the more lateral screws. Once two to three screws have been placed, the baseplate is sufficiently fixed to the bone so the assistant can release it. (F-H) All bone screws are in place, and the cover screw has been added in the central plate. Note the essentially perfect fit of the CNC-milled implant to the skull. (I) The muscle is brought back to completely cover the implant, and it is sutured together, followed by suturing of the skin. The approximate anterior (A) - posterior (P) orientation is indicated in the upper right corner of some panels. All photos in this figure show the implantation of Monkey H.

#### Waiting time between surgeries

Following complete wound healing after the baseplate implantation, the top part is implanted. During this period, the baseplate implant is protected from the outside world, minimizing the danger of postsurgical infections that could jeopardize its osseointegration and the integrity of the underlying bone.

The waiting period between the two implantations differed substantially across monkeys (Table 2.5), ranging from 7.7 to 80.9 weeks (median: 37 weeks). The extent of the waiting period was mostly imposed by the needs and the progress of the respective experimental projects. Note that implant osseointegration takes 6-12 weeks (Hacking et al. (2012); also see discussion). Accordingly, we recommend a minimum waiting period of about 8 weeks, yet longer periods likely increase the probability and extent of osseointegration.

Importantly, during this period, there is no percutaneous implant and thus, no wound care is needed. We typically used this waiting period to train our animals in necessary procedures that do not require head-fixation, like chair training, acclimatization with the experimental set-up, initial head-free training in the recording booth.

#### **Top-part implantation**

An important goal in this surgery is to produce a perfectly round hole in the skin that fits precisely around the top-part implant. In our experience, this is not feasible by manually cutting the skin, with or without adding sutures. Rather, we adopted an approach to punch a hole using a circular knife ("punch tool"; see Fig. 2.7). In this section, we present step-by-step the procedure and the tools we developed over the years. Table 2.6 provides a summary of the implant parts and special instruments used in this implantation.

The implantation of the headpost top part is a short surgery and can be performed under ketamine-medetomidine anesthesia and NSAIDs. Typically, the use of a stereotaxic frame is not necessary unless one needs to rely on stereotaxic coordinates in order to find the central plate of the previously implanted baseplate (different approaches are discussed below).

First, the skin is shaved and thoroughly disinfected and then, the central part of the baseplate has to be found. After shaving, one can typically see the healed suture line from the baseplate implantation which can help estimate the approximate position of the baseplate. If the baseplate is close to a bone landmark that can be

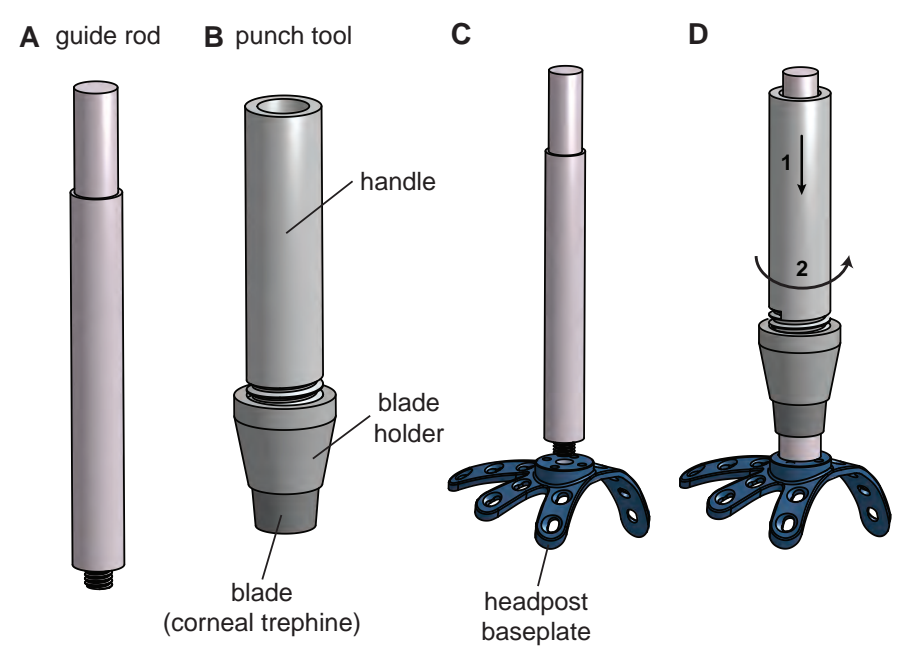


Figure 2.7. Illustration of the punch tool and its use in the top-part implantation. (A) Guide rod. (B) Punch tool. (C) The guide rod is screwed into the central plate of the previously implanted baseplate. (D) The punch tool slides on the rod to achieve a perfectly aligned and round cut through the scalp and muscle. Note that during the actual punching, the punch tool must not be merely pushed against the skin (illustrated with arrow 1), but it needs to be slowly rotated (illustrated with arrow 2). Different colors are used to illustrate the baseplate, the guide rod and the punch tool, even though they were all from metal.

palpated through the skin (like the supraorbital ridge), and/or if the muscle above the baseplate is thin, then the baseplate can be simply localized by palpation. If this is not the case, the central plate needs to be located by other means. In Monkey C, which was implanted with the central baseplate version, finding the central plate during the top-part implantation was difficult and time consuming, yet in the end successful. A way to facilitate this step could be to rely on stereotaxic coordinates; another option might be to leave a mark on the skin after the baseplate implantation, e.g. a tattoo; or position the central plate over the midline where typically there is no or only a thin layer of muscle. Placing the central part over the midline of Monkey K greatly facilitated this step. When the baseplate has been located, a small incision is made to expose the central cover screw, which is then removed (Fig. 2.8A-C).

To perform the circular skin incision at the area where the top part will be implanted, we developed a custom-made punch tool with a circular sharp tip. For a similar result, a commercially available corneal trephine was integrated into the end of the punch tool (Fig 2.7B and Fig. 2.8E). A guide rod that fits within the punch tool is used to perfectly position the circular blade relative to the central part of the baseplate. To do so, the guide rod (Fig. 2.7A) is screwed into the central screw hole of the baseplate (Fig. 2.7C and Fig. 2.8D) and then, the punch tool can easily slide on it (Fig. 2.7D). Note that our version of this guide rod needs to be aligned very precisely to the baseplate to allow screwing it in. Finding the right angle might take a few minutes. This could be potentially improved by small modifications of the screw thread.

Before the punch tool touches down on the skin, the assistant stretches the skin in all directions away from the guide rod (Fig. 2.8E). During the actual punching, the punch tool must not be merely pushed against the skin, but it needs to be slowly rotated, such that its circular blade can actually cut the skin and the underlying muscle, down to the central part of the baseplate. After the punching (Fig. 2.8F), the guide rod is removed (Fig. 2.8G).

Over time, we noticed some skin retraction around the top-part implant. To compensate for it, we use a punch tool that allows us to make a cut that is a bit smaller than the diameter of our implant, providing a tight fit. A trephine (Beaver-Visitec International, Waltham, Massachusetts, USA) with diameter of 11 mm was used in Monkey H for a top-part implant of 14 mm diameter. The use of the commercially available corneal trephine was inspired by a post in the NC3Rs Chronic Implants Wiki (NC3Rs, 2015) which presented their suitability for performing circular cuts through the scalp. Note that the corneal trephines are disposable and have to be discarded after a single use, because they are not sharp anymore. Similarly, our in-house punch tool becomes blunt during the process and needs to be resharpened after each surgery.

After performing the circular incision, the top part is implanted onto the baseplate (Fig. 2.8H), by inserting the two guide pins of the top part into the respective holes in the baseplate. The "top-part screw" is inserted and loosely tightened, such that there remains a little gap between the lower surface of the top part and the baseplate central plate. At this point, it is typically challenging to get all soft tissue (skin/fascia/muscle) out of this gap. We go around the top part with a pair of Dumont tweezers, at each angle pulling out any soft tissue. Subsequently, we apply a first, gentle, tightening of the top part.

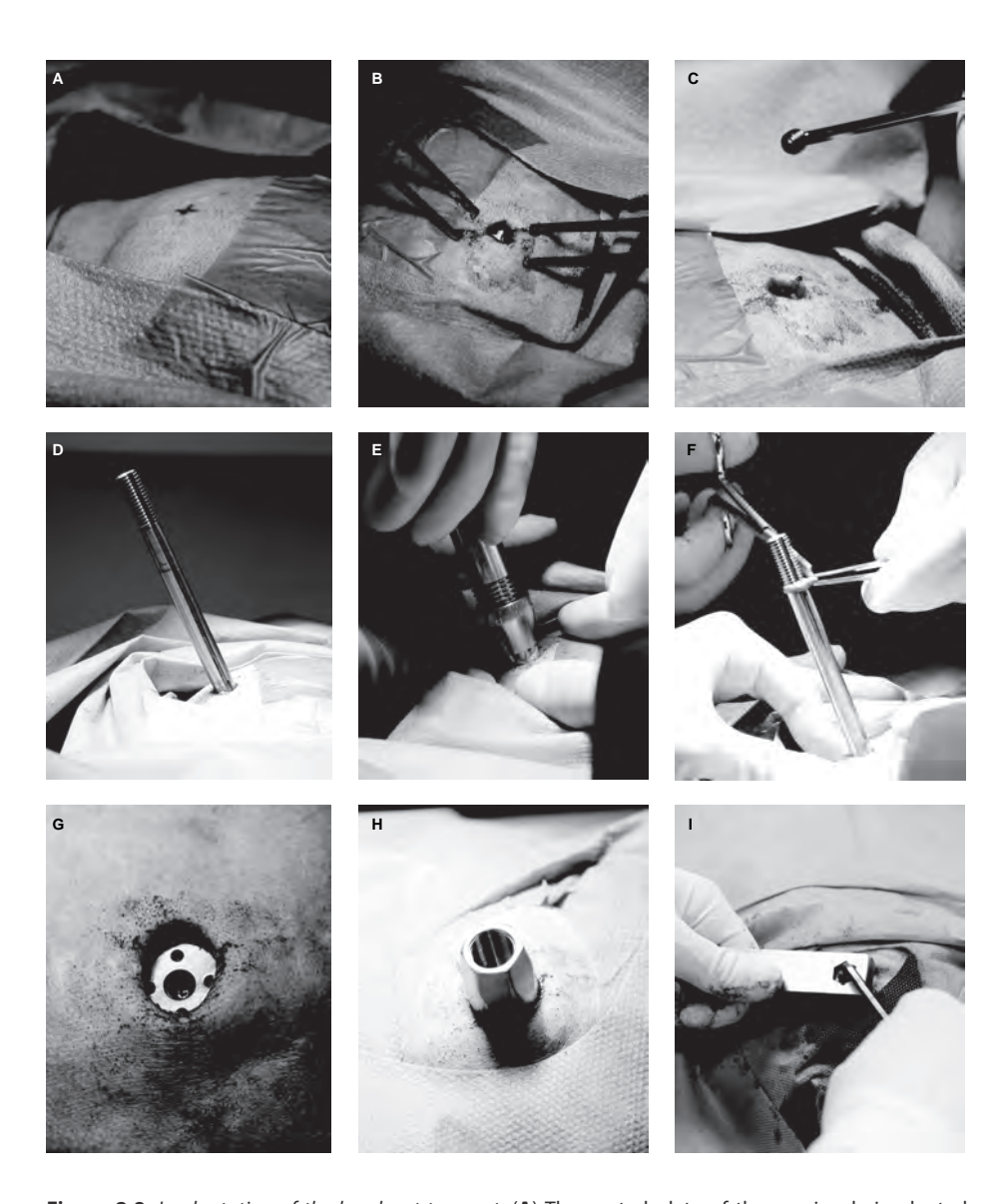


Figure 2.8. Implantation of the headpost top part. (A) The central plate of the previously implanted baseplate is found, and a mark is made on the skin. (B) At this location, a small incision through the skin is performed to access the cover screw. (C) The cover screw is removed from the central plate, and (D) the guide rod is screwed in this screw hole. (E) The punch tool is sled onto the guide rod. While the assistant stretches the skin around the guide rod, the surgeon punches a hole into the skin by gently pushing and rotating the punch tool with the trephine blade. In the illustrated surgery, a corneal trephine blade was incorporated in a custom-made handle. (F) The ring of cut skin is removed. (G) The resulting hole in the skin is circular and centered on the central part of the baseplate. (H) The top part is added. (I) The central screw is tightened, while holding the top part with the holding tool. Panels A-H show the implantation of Monkey H, panel I shows Monkey C.

For the final tightening, the head must not be in the stereotaxic apparatus. Otherwise, there is danger of damaging of the ears or the teeth. To be able to exert sufficient force for the final tightening, a holding tool with hexagonal cut-out is placed on top of the top part (Fig. 2.8I). A hex key is inserted into the top-part screw which is then tightened (by applying force between the holding tool and the hex key) with substantial force. Given the considerable force that is required, the tightening should not be done without the holding tool: in this case, the force would also be seen by the bone screws; by contrast, with the holding tool, the force is between the holding tool, the top part and the top-part screw, i.e. it remains within the metal structures of the implant. So far, we used a normal hex key and manual force estimation; yet the use of a torque screwdriver would likely be advantageous to ensure that the top-part screw is sufficiently tightened without applying unnecessary excessive force that could damage the thread.

**Table 2.5.** *Waiting time between headpost-baseplate and top-part implantations.* 

Monkey	Waiting time (weeks)
Monkey L	20.9
Monkey Sk	10.9
Monkey D	21.6
Monkey G	68.6
Monkey Hu	37.1
Monkey Ch	72.7
Monkey T	80.9
Monkey St	7.7
Monkey M	50.6
Monkey H	76.9
Monkey C	8.3
Monkey K	36.9

**Table 2.6.** List of implant parts and implantation instruments used in the headpost top-part implantation.

Implanted parts		Material	Production
top part		titanium Grade 5	in-house
top-part pins		stainless steel, Ø 2mm	commercially available
top-part screw		titanium Grade 5	in-house
Implantation Instruments			
guide rod		stainless steel	in-house
punch tool (I)		stainless steel	in-house
punch tool (II):	blade holder	stainless steel	in-house
	corneal trephine blade	stainless steel	commercially available
holding tool		stainless steel	in-house

## **Headpost holder**

In order to increase handling safety, we developed and produced a headpost holder that allows remote posting (Fig. 2.1C). This holder is ≈31 cm long. The experimenter needs to touch and operate merely the proximal end, whereas the distal end attaches to the top part of the implant on the monkey's head. In this way, the experimenter's hands always remain at a safe distance from the animal's head.

The holder, at its distal end, contains a central screw and a cap that fits onto the implanted headpost top part. When the headpost-holder screw is screwed into the top-part screw hole, this essentially pulls the hexagonal conus of the top part into the cap and thereby firmly secures the top part to the holder. Figure 2.1C graphically demonstrates an experimenter tightening the holder screw by turning the knob at the end of the holder. During this procedure, we found it useful to slightly wiggle the holder, such that the cap would "find" the optimal orientation to fit to the hexagonal conus of the top part.

The holder is produced by assembling the following independent pieces of stainless steel: 1) a "top-part cap" that fits onto the hexagonal surface of the headpost top part, 2) a tube, 3) a rod with a thread (M9 x 0.75) at its distal end, 4) a knob, and 5) a retainer cap. The top-part cap is welded onto the distal end of the tube, and the rod is inserted in the tube. At the proximal end, a retainer cap keeps the rod from slipping out while allowing it to freely rotate inside the tube. A knob welded at the proximal end of the rod allows the experimenter to comfortably rotate it during head (un)posting. The hexagonal shape of the top-part cap is cut using electrical discharge machining, because this achieves a perfect fit of the cap on the implanted top part with its fine and straight, i.e. non-rounded, edges.

In our setup, the headpost holder is secured to a headpost-holder mount (Suppl. Fig. 2.3), which is attached directly to the primate chair. This mount can be adjusted to hold oblique headpost-holder orientations, and thus, it accommodates a slightly oblique orientation of the headpost top part. This in turn allows to place the central plate of the baseplate away from the midline.

## A three-piece connector chamber

### **Design considerations**

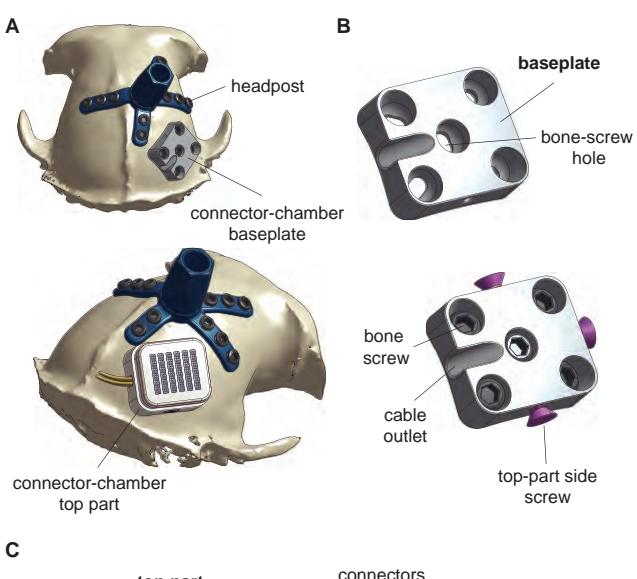
Inspired by the two-piece headpost, we developed a connector chamber that consists of three separate pieces: a baseplate, a top part and a lid (Fig. 2.9). This modular connector chamber houses the connectors of multiple chronic electrode arrays and is implanted in a two-step implantation approach. The baseplate is the piece that comes into direct contact with the bone. It is implanted first and then covered with muscle and skin (see section 'Implantation of the connector-chamber baseplate'). Following an adequate healing period of a few weeks that ensures initial osseointegration, the chronic microelectrode arrays are also implanted. During their implantation (see section 'Implantation of the connector-chamber top part and electrode arrays'), the baseplate is exposed and the top part that contains the array connectors is mounted and secured onto the baseplate. Finally, the lid is added to keep the connectors dry and protected outside of the experimental set-up.

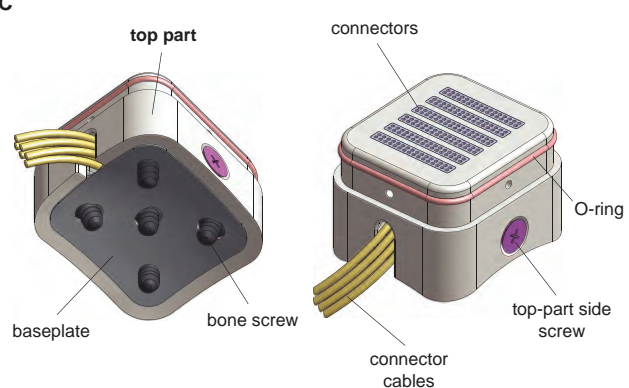
Two monkeys (Monkey C and Monkey K) were implanted with the central headpostbaseplate version. These animals are intended to be chronically implanted with microelectrode arrays in areas V1 and V4 of the left brain hemisphere. Each monkey would be implanted with six floating microelectrode arrays in total (Microprobes for Life Science, Gaithersburg, Maryland, USA), each consisting of 36 channels. The connector chamber was planned to be implanted over the right hemisphere, just posterior and close to the headpost baseplate (Fig. 2.9A) while it had to be large enough to house six Omnetics connectors (32-channel each; Omnetics Connector Corporation, Minneapolis, Minnesota, USA).

This type of arrays typically comes with a commercially available Crist Instrument titanium connector chamber (sometimes referred to as "pedestal") that features radially extending legs that are fixed onto the skull with titanium bone screws. However, we had to develop a custom design for the

following reasons; 1) these commercially available connector chambers could only house up to 4 Omnetics connectors, and 2) due to the proximity of the chamber to the headpost baseplate, the implant size had to be minimized. In fact, in none of the two monkeys there was enough space to fit a chamber with extending legs. Thus, we developed a new design that prioritized the reduction of implant size. This was achieved by planning an implant with the following main characteristics:

1) It is a footless implant. The titanium bone screws are incorporated within the connector-chamber baseplate (Fig. 2.9B). In other words, the size of the implant mainly depends on the number and the size of the electrode connectors that are planned to be housed within it.





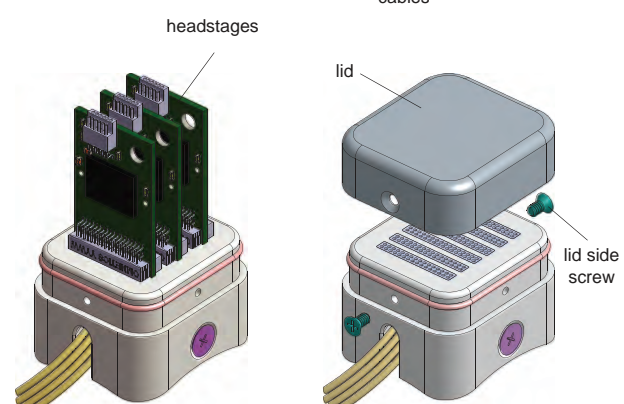


**Figure 2.9.** The modular connector chamber. (A) Illustration of the twostage implantation of the connector chamber (Monkey C). The baseplate is implanted first. Several weeks later, the top part that houses the electrode connectors is implanted in another surgery together with the electrode arrays (not shown here). Panels (B-C) show in detail the baseplate and the overall implant, respectively. Note that all main parts of the implant (baseplate, top part and lid) are made of titanium; different colors are used for illustration purposes.

- 2) It is a cement-free implant that is secured to the bone merely by five titanium bone-screws, without the need of an additional cement-cap. Such caps typically extend around the implant occupying considerable space on the skull.
- 3) Both the top part and its lid are mounted (to the baseplate and the top part, respectively) with side-screws (Fig. 2.9B-C), that do not significantly increase the implant's footprint. In an earlier design version (that was not realized in the end), the top part was mounted on the baseplate with two vertical screws. By switching to side screws, the overall size of the baseplate was decreased from 39 x 23 mm to 21 x 19 mm. In addition, its thickness was reduced by 4 mm, which is beneficial for muscle and skin healing during the waiting period. This thickness reduction was possible, because the baseplate did not have to accommodate anymore the thread length of the vertical screws above the skull.
- 4) The implantation of the baseplate in a separate surgery significantly reduces the duration of the later electrode-implant surgery. Electrode implantations can be long and demanding, so they benefit strongly from deferring part of the efforts into a separate surgery.

### Planning and manufacturing

The first planning step was the estimation of the minimum implant size that was required in order to fit the number of the connectors that were planned for our experimental needs. The connector chamber should house six 32-channel Omnetics connectors and allow enough space for three dual-64 channel headstages (Intan Technologies, Los Angeles, California, USA) to be comfortably connected onto them on a daily basis. For the top part, an additional wall thickness of 2 mm was included in our estimation. A rectangular box of these dimensions was fitted onto the skull model of the individual monkey and the three implant parts were subsequently designed: the baseplate, the top part and, the lid. All parts were produced from titanium Grade 2 and CNC-milled in a 5-axis machine. Here we provide a detailed description of each piece of the connector chamber.

#### Baseplate (Fig. 2.9B):

The bottom surface of the baseplate is planned to follow the geometry of the underlying bone, while its upper surface is flat in order to allow the top part to tightly sit against it. The baseplate incorporates five screw holes that are perpendicular to the bone surface and an outlet to allow the connector cables to leave the chamber. Finally, it includes three screw holes on the sides that allow the top part to be secured to it.

### Top part (Fig. 2.9C):

The lower end of the top part slides over the baseplate, such that the baseplate almost completely disappears inside the lower end of the top part (a small gap between the lower surface of the top part and the bone was introduced to allow for potential bone growth). The top part is then fixed to the baseplate with lateral screws. Similar to the baseplate, the top part incorporates a cable outlet on its left side. On the upper surface of the implant, there are six slits that would allow the experimenter to connect the headstages to the electrode connectors.

The top part was first produced in-house and then, it was sent to the company that produced the electrode arrays (Microprobes for Life Science). They incorporated the Omnetics connectors into our top part and the free space was filled up with epoxy (Suppl. Fig. 2.4A-B). Subsequently, we applied a thin layer of bone cement (Super-Bond, Sun Medical Co. Ltd., Moriyama-shi, Japan) at the bottom of the top part, covering completely the epoxy (Suppl. Fig. 2.4C and 2.4E), as a protection layer against fluids.

Three titanium side screws (M 2.5) fix the top part to the baseplate. During implantation, the cable outlet is also filled with Super-Bond to achieve proper sealing. An additional thin layer of cement (Super-Bond) is applied between the top part and the baseplate, preventing liquid from entering the implant.

The top part also features two pairs of screw holes for securing the lid. A spare pair of screw holes was added that could be used in case that the first set gets worn out after repetitive use.

#### Lid (Fig. 2.9C):

The lid is mounted on the top part with two titanium side screws (M 1.6). An O-ring is added at the interface between the top part and the lid to provide additional sealing.

### Implantation of the connector-chamber baseplate

The implantation of the connector-chamber baseplate is a very similar procedure to the headpost-baseplate implantation that has been extensively described in section 'Headpost-baseplate implantation'. Here, we present the main steps of this surgery and indicate the main differences to the headpost implantation. Monkey C was implanted with the connector-chamber baseplate 28 weeks after the headpost baseplate and 19.7 weeks after the top-part implantations.

The location of the skin incision was defined based on the planned stereotaxic coordinates of the central bone screw of the implant. We tried to keep the size of the incision and the area of exposed skull minimal in order to make sure that the skin and the muscle surrounding the neighboring headpost would stay as intact and healthy as possible. The muscle was cut down to the level of the bone, and the skull was cleaned from connective tissue without removing the periosteum. The baseplate was inserted through the incision to test whether the size of the exposed skull was big enough.

The planned stereotaxic coordinates of the five bone screws were used to find the exact position of the implant. Note that this step differs from the implantation of the headpost baseplate, especially the milled version. In the latter case, one can use the stereotaxic coordinates as a first approximation to the target location. Then, thanks to its bigger size and long radially extending legs, one can manually adjust its position and find its optimal fit on the skull. In contrast, the connector-chamber baseplate is way smaller and footless which renders it infeasible to manually find its best fit. Instead, one needs to almost exclusively rely on the planned stereotaxic coordinates of the bone screws.

We used a sterile pen to draw the position of each of the bone screws based on these coordinates and then, we positioned the implant according to the marks and tested its fit against the skull. When the target location was found, the assistant held the baseplate in place and the surgeon started implanting the length-adjusted bone screws one by one, adding first the central screw and then the lateral ones. See section 'Headpost-baseplate implantation' for a detailed description of the drilling and screw implantation steps.

Even though the bottom part of the connector-chamber baseplate was planned to follow the skull surface, its top surface was designed to be flat so that the top part can later on sit on it. This led to two important differences compared to the headpost baseplate implantation. First, when drilling using the drill stop, we had to find the proper angle that aligned the stop with the angle of the respective screw hole while ignoring the angle of the top surface of the implant. We found this step to be more difficult than in the implantation of the headpost baseplate. Second, the heads of the implanted screws were completely hidden within the screw holes. The gaps between the screw heads and the upper surface of the implant were filled with Super-Bond (see graphical illustration in Suppl. Fig. 2.4E) in order to avoid connective tissue growing there.

The top part of the connector chamber is mounted on the baseplate with three side screws. These screws were placed temporarily at the end of the baseplate implantation (as shown graphically in Fig. 2.9B), to avoid bone or connective tissue from blocking the screw holes. They have been removed and replaced by new ones during the top-part implantation. Finally, the muscle and the skin were closed up and sutured.

### Implantation of the connector-chamber top part and electrode arrays

During this surgery, the previously implanted connector-chamber baseplate is exposed, the chronic electrode arrays are implanted in the brain, and the connector-chamber top part housing the electrode-array connectors is mounted and secured onto the baseplate. Here, we provide a detailed description of the steps towards the implantation of the connector-chamber top part. For simplicity, we use in this section the terms 'baseplate' and 'top part' to refer to the main parts of the connector-chamber implant. The implantation is performed under general anesthesia. The monkey is intubated and positioned in the stereotaxic frame. Monkey C was implanted with electrode arrays and the top part 10 months after baseplate implantation.

Following anesthesia induction, the surgical site was shaved and thoroughly disinfected. The previously implanted baseplate could be located by palpation. A large coronal incision through the scalp exposed both the left and the right hemispheres. This provided access to both the previously implanted baseplate (right hemisphere), and the area where the electrode arrays were to be implanted (left hemisphere). Part of the muscle covering the baseplate was cut and removed to expose the baseplate.

The three side screws (graphically depicted in Fig. 2.9B) on the baseplate, which were used to block bone and tissue growth within the screw holes, were removed, and the baseplate was cleaned with saline. There was pronounced bone growth around the baseplate. On some places, the new bone had almost reached the lower part of the side-screw holes. At this stage, the top part was mounted onto the baseplate in order to test its fit. Due to the extensive bone growth, the top part did not fit onto the baseplate and we had to remove some part of the new bone (using the Piezosurgery 3, Carasco, Italy). We repeatedly tested the fit of the top part onto the baseplate to limit bone removal to the required minimum. Note that even if the top part slides and fits onto the baseplate, it is still crucial to also test the fit of all three side screws that secure the two pieces together. We noticed later (see below) that even small misalignments due to the bone growth can prevent some of the screws to be properly mounted. The top part was then removed from the surgical area and stored in a sterile container.

Then, the muscle over the left hemisphere was detached from the skull using a periosteal elevator, the periost was removed, and a trepanation was performed. Then, the top part was placed onto the baseplate and the electrode arrays were implanted. The trepanation was covered with the bone flap, which was then sealed with bone cement (Super-Bond).

While mounting the top part onto the baseplate, we noticed that two out of the three side screws that were planned to secure the top part onto the baseplate (see Fig. 2.9B) did not fit, because we had only tested the fit of the top part, but we had not test-placed the screws. Some additional drilling allowed placement of the second screw. Further drilling was avoided to limit the time of dura exposure. To ensure proper stability of the top part, the empty space in the third screw hole was filled with bone cement. Bone cement was also applied to cover the other two side screws to ensure proper sealing. The cable outlet (see Fig. 2.9B-C) and all of the cables between where they exit the connector chamber and where they disappear under the bone flap were covered with bone cement. Finally, bone cement was also applied around the connector chamber to fill any small gaps between the bone and the top part.

The skin around the wound margin can often be swollen for some days or weeks postoperatively. In our case, this complicated the use of the connector-chamber implant during the first postoperative week due to: a) the overall low profile of the implant and, b) the use of side screws that secured the lid onto the baseplate. To solve this problem, some skin was removed one week later under a short ketaminemedetomidine anesthesia. This allowed us to securely open the lid in the next days. See section 'Future refinements' for a future refinement of our approach that will allow us to remove precisely as much skin as needed using a punch tool similar to that used in the case of the headpost top part.

### Wound care

We followed a similar wound care approach for both the headpost and the connector-chamber implants. Following the top-part implantation, the postoperative treatment was typically minimal. It included frequent hair-cuts around the wound margin and occasionally flushing with saline to clean the surrounding area. If the tissue looked irritated or slightly infected, the wound was flushed with

antiseptic liquids. See Figure 2.11 and section 2.3 for later assessment of skin condition around the headpost.

## Results

Twelve macague monkeys were successfully implanted with headpost implants following our two-part design and two-step implantation approach. To date, there has been no implant failure or loosening from the bone in any one of the monkeys, in four cases more than 9 years after top-part implantation. The only failure that occurred so far was that in one animal (Monkey T), the top-part screw (located completely outside of the bone) partially loosened, such that the top part was not any more fully fixed to the baseplate, leading to small rotations. In this animal, we placed a new top part with new pins. This fixed the problem, and it did not reoccur. During the exchange, we found that the small movements of the top part had partially worn out at least one of the pin holes in the baseplate. Crucially, the baseplate remained firmly fixed to the bone. In order to prepare for any similar future cases, we then added two additional, spare, pin holes on the baseplate design. Yet, so far, we never had to use them. Note that in none of the animals, we observed any wearing out of the threads that connect the top part with the headpost holder, probably because these threads are relatively coarse.

Table 2.7 summarizes the longevity of the headpost for all implanted monkeys. Implant longevity was defined as the number of years from the top-part implantation until today or until the end of the respective animal's life (Monkey T was sacrificed, Monkey M died; both unrelated to the headpost). Monkey L has been successfully implanted for 9.7 years. In total, four out of the twelve monkeys have been implanted for more than nine years showing no implant-related problems. Monkeys H, C and K are the most recently implanted.

Nine monkeys underwent an additional CT scan following the baseplate implantation. These CT volumes were used to assess the long-term stability of the implanted bone screws. The time of assessment ranged from 0.1 to 7.9 years (Table 2.8). We found that at the time of the scan, there was no post-operative screw loss in anyone of the nine monkeys.

Monkey T was sacrificed due to reasons unrelated to the headpost. At that time, the baseplate had been implanted for 6.3 years. All bone screws were in place and high levels of osseointegration were observed above the legs of the implant (Fig. 2.10). Note that a bone screw was removed post mortem in the context of investigating the implant (see stars in Fig. 2.10).

Different levels of skin retraction were observed across animals. Figure 2.11 shows recent photos of the wound margin of three example monkeys. Skin retraction could not be assessed in monkeys M and T that were not alive at the time of evaluation. None of the ten monkeys showed extensive granulation tissue, or signs of infection like puss. Six monkeys showed no significant skin retraction, of which two example cases are shown in Fig. 2.11A-B. In Monkey G (Fig. 2.11A), the skin tightly followed the implant and looked dry and healthy even 8.7 years post implantation (when the photo was taken). Four of the monkeys implanted with the manually bent baseplate showed some level of skin retraction. Interestingly, in all of them the skin had almost exclusively retracted on top of the long anterior leg running over the left brain hemisphere. Figure 2.11C shows an example case of skin retraction (Monkey L), where the head of one bone screw has been exposed. Of the four monkeys with some skin retraction, three had only one bone screw exposed (Monkey D, Monkey Hu, and Monkey L), and one had two screws exposed (Monkey Sk). Importantly, in all four monkeys, the wound margin was dry, with no indication of ongoing retraction or bone exposure. The implants were stable and none of the animals showed any sign of discomfort.

While reviewing the post-operative CT volumes, we noticed that in two out of the four monkeys that showed some skin retraction, there was a small gap between the left anterior leg of the implant and the underlying skull (Monkey Sk and Monkey L; Note that there was no post-operative CT scan of Monkey D). This slight gap might have contributed to the observed skin retraction. However, skin retraction can be caused by many factors (see Discussion, section 'Skin Retraction'). Given that the implant longevity for these four monkeys with some skin retraction ranges from 8.7 to 9.7 years, we can conclude that the skin retraction has not affected the stability of the implant.

Three monkeys were implanted with headpost implants that were CNC-milled to closely match the skull surface. CNC-milling allowed us to improve the fit of our implants especially at the central plate of the baseplate. This central plate was difficult to fit to the skull in the version with the manually bent baseplate.

Finally, a novel connector-chamber implant was designed, produced and implanted in Monkey C. The baseplate was implanted first. Ten months later, the top part and the electrode arrays were implanted in a second surgery. During the

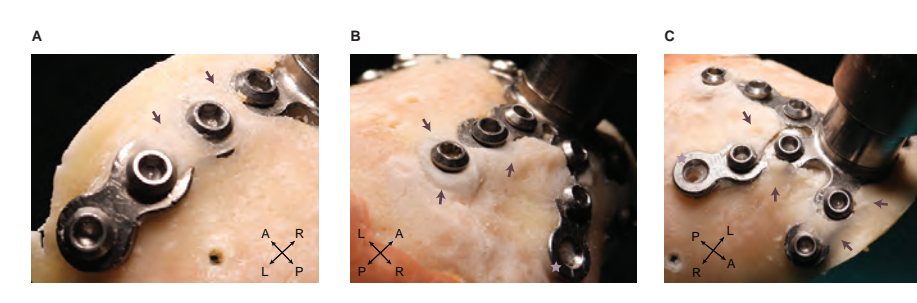
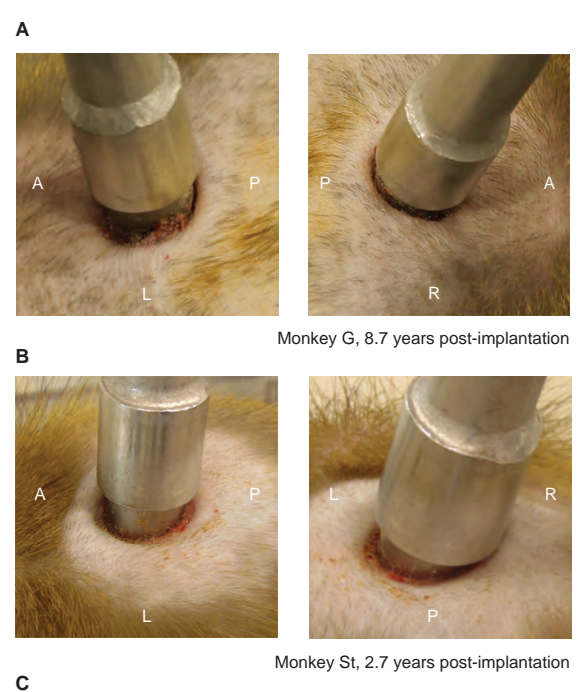
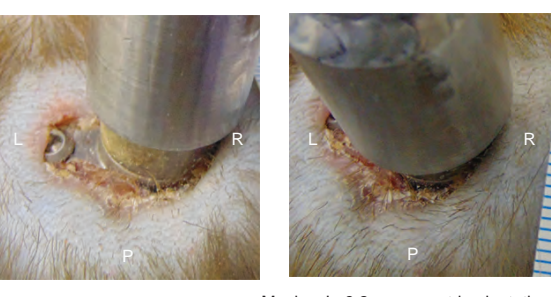


Figure 2.10. Osseointegration of the headpost baseplate. Pronounced bone growth over the implant legs 6.3 years after its implantation (Monkey T). Arrows point to areas of prominent bone growth. Stars indicate a bone screw that was removed post mortem. Bone holes outside the area of the implant were drilled post mortem for training purposes.





Monkey L, 9.2 years post-implantation

Figure 2.11. Skin condition around the headpost implant. The wound margins of three example monkeys are shown. (A-B) Two example cases with no skin retraction. (C) In Monkey L, the skin has retracted above one of the baseplate legs exposing the head of one bone screw. All photos were taken without prior wound cleaning on the same day. The anterior (A), posterior (P), left (L) and right (R) orientation is indicated with white letters on each photo.

top-part implantation, we observed: a) that the muscle covering the baseplate had completely healed since the baseplate implantation and, b) very pronounced bone growth around the baseplate. In several parts surrounding the baseplate, the new bone had grown for ≈2 mm reaching the side-screw holes. Parts of the new bone had to be drilled away to allow for the top part to slide and fit onto the baseplate. We expect that additional bone remodelling had taken place around the bone screws and underneath the baseplate which provides additional stability to the implant. At the time of writing this text (2.6 months post-implantation), the implant is stable, and the signal quality of the electrode arrays is good.

The skin around the implant is dry without signs of infection. The monkey shows no signs of discomfort. As expected, the skin has retracted over the bone cement that was applied to seal the cable outlet, exposing the bone cement in this area. There is no significant skin retraction around the rest of the implant. Due to the low overall profile of the connector chamber, we noticed that the lid and its side screws that secure it onto the top part might not be the optimal choice for the following reasons: a) the side screws are very close to the skin which makes it more difficult to remove them on an everyday basis and, b) because the lid is so close to the skin, it needs extensive cleaning every time it is removed. Based on this experience, we improved the connector-chamber design in order to surpass the difficulties we faced during implantation and to facilitate its everyday use. The new design is described in detail in section 'Future refinements of the connectorchamber implant'. Monkey K will be implanted with this new design.

**Table 2.7.** *Headpost implant longevity.* 

Monkey	Years	
Monkey L	9.7	
Monkey Sk	9.3	
Monkey D	9.1	
Monkey G	9.2	
Monkey Hu	8.7	
Monkey Ch	5.0	
Monkey T	4.8***	
Monkey St	3.2	
Monkey M	2.0***	
Monkey H	1.4	
Monkey C	1.0	
Monkey K	0.3	

Number of years from top-part implantation until today or until sacrifice/death, the latter indicated with three stars (\*\*\*).

**Table 2.8.** *Time of implant assessment.* 

Monkey	Years	
Monkey L	7.9	
Monkey Sk	7.5	
Monkey G	7.0	
Monkey Hu	7.2	
Monkey Ch	5.7	
Monkey T	3.9	
Monkey St	0.1	
Monkey M	2.6	
Monkey H	1.4	

Years between the implantation of the headpost baseplate and the acquisition of the CT volume used for the implant assessment.

## Discussion

We described the planning, production and implantation of modular and cementfree cranial implants made of titanium. The modular nature of our implants allowed us to perform a two-step implantation approach that led to long-lasting, healthy implants even more than 9 years post implantation. To our knowledge, these are the longest follow-up cases reported for headpost implants. By reviewing postoperative CT scans, we also demonstrated the safety of using length-adjusted bone screws that are shortened to follow the thickness of the skull.

The two-step implantation approach combined with the introduction of a punch tool achieved a tight fit around the headpost top part without the need of additional sutures. This solved a frequent post-operative problem, namely the opening of sutures around the percutaneous part of the implant.

Overall, we describe several modifications with respect to previously developed methods, which likely contributed to our observations that the implants were surrounded by relatively irritation-free wound margins, and that they all lasted through the entire observation period. Together, those modifications therefore constitute an implementation of the 3R principles. In particular, we consider it a refinement if, in a given animal, the wound margin is free of irritation, and the headpost is long-term stable without the need of reimplantations. We also consider it a refinement that the screws are adjusted to the skull thickness, such that the risk of irritation or damage to the dura is minimized. Finally, we consider it a potential for reduction in animal numbers, if a given animal is in a healthy state with a stable headpost, such that it can potentially be used for further experiments.

We provide access to the drawings and models of our implants and the specialized tools that we developed over the years. We believe that sharing the methodological details and the long-term results from a significant number of animals can promote animal welfare by helping other labs to improve their methods.

## The two-step implantation approach

Several previous studies have described a two-step implantation approach. For example, Pfingst et al. (1989) and Betelak et al. (2001) implanted titanium fixtures (anchor screws) that they let osseointegrate before securing cranial implants on them in another surgery. Blonde et al. (2018) implanted a large skull cap made of PEEK on which they subsequently added headpost and recording chamber implants.

Finally, Chen et al. (2017) reported a two-step implantation of a footed titanium connector chamber.

Here, we further establish the suitability of this approach for the case of headpost as well as connector-chamber implants. The two-step approach allows to cover the implant with muscle and skin, protecting it from bacterial colonization. It also minimizes the risk of micro-movements of the implant relative to the bone, which might happen for one-piece implants with a percutaneous part, when the animal bumps with it against the chair or the home cage. Together, these factors likely promote the start of osseointegration, which seems essential for its later success. We think that the two-step approach was a crucial ingredient for the longterm stability that we observed for all implanted headposts, and we therefore recommend it as standard procedure. We estimate that the gain in animal welfare exceeds the "cost" incurred by the need for a second surgery; note that the top-part implantation is a short procedure that does not require intubation and typically lasts less than an hour.

Additionally, the two-step approach does not necessarily extend the overall time of preparation, because it is anyhow common practice to not place load on the implant for some period after implantation to allow sufficient osseointegration, also with one-step approaches. For example, Adams et al. (2007) waited two weeks, Hacking et al. (2012) six weeks, and Overton et al. (2017) four to twelve weeks between headpost implantation and first head fixation, depending on the age of the animal. Similarly, Lanz et al. (2013) mention that their monkeys were not headposted during the entire training period, until the recording chamber was implanted.

Adams et al. (2007) reported the formation of woven bone at the implanted area four weeks after the implantation of a footed, cement-free headpost implant. Hacking et al. (2012) showed new bone formation 14 weeks after the implantation of both textured and polished cement-free, titanium plates.

The two-piece design inherent to the two-step approach has a few additional advantages: The top part can be temporarily removed to fix other parts to the baseplate. We have used this option to place CT markers for stereotaxic calibration into well-defined and reliable positions. The top part could in principle also be removed if an animal has a very long "holiday" or is not anymore used for experiments. Finally, the top part could also be exchanged for a modified piece if helpful for the experiment.

## Shortened bone screws and the choice of screw type

The use of shortened bone screws did not compromise implant stability. In fact, we experienced no post-operative screw loss. Several other studies have supported the use of length-adjusted bone screws. Mulliken et al. (2015) presented a recording chamber in which the bone screws were counter-sunk into chamber walls such that only 2.5 mm of the screw thread entered into the skull. Similar to our approach, Pfingst et al. (1989) shortened bone screws according to skull thickness, and Overton et al. (2017) used commercially available bone screws that came in different lengths according to pre-surgical measurements of the bone thickness. In accordance with our experience, Betelak et al. (2001) reported that the skull thickness of macaque monkeys (Macaca mulatta and Macaca nemestrina) ranges from 2.5 to 4 mm, and they used a screw length of 3 mm (see also section 'Considerations regarding the age and sex of animals'). Note that we have successfully used the same screw planning approach (section 'Planning and preparation of bone screws') for the implantation of other implants like recording and chronic connector chambers. which we have so far embedded in bone cement (not described here).

The choice of the type of bone screw used can play a crucial role in the implant success. We believe that part of the long-term success of our implants was due to the use of the specific self-tapping bone screws employed here. We have experienced screw loss in earlier experiments (not described here) involving other types of screws. Note that screws can differ substantially with regard to the depth and shape of their screw thread.

### Bent versus CNC-milled baseplate

We described two approaches to arrive at the individually shaped baseplate, namely the manual bending approach and the CNC-milling approach. Manually bent baseplates can be produced on 3-axis CNC machines from relatively thin titanium sheets in larger numbers, while discarding relatively little material, which makes them substantially cheaper. The CNC-milled baseplate version requires a 5-axis CNC machine and more planning and material, leading to substantially higher production costs. Together, these factors might limit availability of CNCmilled baseplates. Yet, while the manually-bent version provided an acceptable fit, this fit was essentially perfect with the CNC-milled version.

A promising alternative approach to CNC-milling is 3D metal printing. Titanium 3D printing has been successfully employed to produce headposts (Ahmed et al., 2022; Chen et al., 2017) and connector-chamber baseplates (Chen et al., 2017). The main advantage of 3D printing over CNC-milling is the lower production cost. However,

note that 3D printing cannot so far produce the required precision for screw threads and very smooth surfaces. Therefore, in the case of our headpost implant, the following post processing would be required; 1) creation of internal screw threads at the central plate of the baseplate and at the top part, 2) smoothing of the external surface of the top part to avoid accumulation of dirt on its bottom part, and to ensure good fit to the headpost holder on its upper part. One potentially attractive option is to combine 3D printing of the monkey-individual baseplate (adding the central screw thread via post processing) with CNC-milling the top part, which anyhow remains constant. Yet, one noteworthy concern about 3D printed metal implants is that the metallic structure of the printed, i.e. successively deposited metal, is different from the structure of the metallic blocks that form the basis of milled pieces; how these structural differences affect suitability for use as implants will require further exploration.

#### Skin retraction

Similar to previous studies, the extent of skin retraction varied across monkeys (Overton et al., 2017), likely due to several factors: 1) The degree of manipulation of the wound margin by the individual monkeys, particularly during the days immediately following the top-part implantation; 2) Potential wound-margin infections at some point after top-part implantation; 3) The fit between the baseplate and the bone varied, with improvements in fit seemingly leading to reductions in skin retraction; 4) The degree of any early gap between the top part and wound margin, which we reduced by decreasing the diameter of the trephine below the diameter of the top part, leading to a tight fit both early after the toppart implantation and also later on. Regarding the latter point, note that in the NC3Rs Chronic Implants Wiki (NC3Rs, 2015), a similar approach is recommended, i.e. a 7.5 mm diameter trephine for a 10 mm diameter implant.

The combination of several refinements most likely contributed to the fact that our most recently implanted animals (Monkey Ch, Monkey St, Monkey H, Monkey C, Monkey K) so far show no significant skin retraction (range of years since top-part implantation; 0.3 to 5 years).

## The three-piece, footless connector chamber

Chen et al. (2017) described a similar cement-free, two-step implantation approach of a footed connector chamber. The baseplate was implanted first and let to osseointegrate for several weeks. An important refinement in our design is the incorporation of the bone screws within the baseplate that led to a significant reduction of the overall footprint of the implant on the skull. Additionally, the footless design might reduce the risk of skin retraction that often occurs on top of implant feet (Mulliken et al., 2015).

Our connector chamber also features several improvements over the commercially available chambers that accompany the floating microelectrode arrays that we used. The commercially available options can only house up to four Omnetics connectors, are implanted in a one-step approach and are typically attached to the skull with bone cement. Our refined version can house six connectors. It is also friendlier to the bone thanks to its cement-free nature and the two-step implantation.

## Considerations regarding the age and sex of animals

All animals reported in this study were male macaques that received headpost or connector-chamber implants during adulthood (range: 7-15.4 years of age). We estimate our approach to be similarly successful in the case of younger and/or female conspecifics. However, there are important differences between animals of different sexes and age groups that should be considered during implant planning.

For instance, in the case of young animals one should take into account developmental changes of skull morphology. Such changes are typically more pronounced in earlier developmental stages. To adapt the implant to the current skull shape, the preoperative imaging should happen close in time to the actual implantation. Longer waiting periods could lead to an imprecise fit. Overton et al. (2017) kept this time period to less than six months (range of ages at the time of implantation: 6.9-29.3 years). Interestingly, Chen et al. (2017) implanted partly juvenile monkeys (range at the time of implantation: 4-7 years) with a time period of up to ten months between implant planning and implantation. These authors did not report problems with the fit of the implants to the skull.

The skull thickness in the area of the implant is an additional factor that can affect the stability of implants and can vary with age and/or between sexes. Adams et al. (2007) compared the thickness of the frontal skull between a 26-month old male macaque monkey, two adult male and four adult female macaques. They report a mean skull thickness of 1.95 mm for the juvenile monkey, 2.93 mm for the male and 2.23 mm for the female monkeys. Based on these measurements, they concluded that one can safely implant juvenile monkeys with titanium headposts. They report the successful implantation of two juvenile monkeys (29 and 38 months olds) with one-piece headpost implants.

The adult male animals used in our experiments had guite extensive muscles (see Fig. 2.6), and this might have contributed to successful healing of the skin, by forming a buffer between the baseplate and the skin. Female and/or young animals might have less muscle. In any case, we recommend to cover as much area as possible of the baseplate implant with muscle and fascia. Even if parts of the implant are not completely covered by muscle, but only by skin, we expect the skin to heal normally, as long as the surgical site is free of infection.

At the same time, both female and/or younger animals typically weight less than their male and/or older conspecifics. Thus, the implant needs to sustain less overall load. In the case of young animals, as they gain weight with age, we expect that the osseointegration will also proceed and sustain more weight. Overton et al. (2017) waited longer periods before loading their headpost implants in the case of larger, stronger or geriatric animals and in cases that the bone might have been previously compromised. In our approach, one can accommodate these aspects by adjusting the waiting period between the implantation of the baseplate and the top part.

#### **Future refinements**

### Future refinements of the headpost implant

In the future, if the overall headpost position allows, we aim to place the central plate, and thereby the percutaneous top part, precisely on the midline. This had been technically difficult or impossible with the manually bent versions, yet has now become possible with the CNC-milled version and was the case in Monkey K (central baseplate version). We believe that this modification has the following advantages: 1) It avoids partly oblique top parts, requiring correspondingly oblique headpost holders, with corresponding technical challenges in fixing them to the chair; 2) It provides identical top part and thereby headpost-holder orientations across monkeys, easing the sharing of equipment across animals; 3) It allows to place the circular skin cut for the top part precisely into the midline, which is expected to be the ideal position with regard to the pattern of scalp vascularization, i.e. with blood supply running from lateral to the midline. While we plan to place the central plate on the midline, we will keep the legs with their screw holes away from the midline, to avoid screws from damaging the superior sagittal sinus. Note that in many animals, there is a bone ridge in the skull midline; if this ridge is very pronounced, it probably has to be drilled away at the position of the central plate.

Another potential refinement is the application of surface treatment on the implant baseplates to promote their osseointegration. Note that we did not apply any surface treatment to the titanium baseplates after CNC-milling and, for the manually bent version, after the manual bending. Thus, there was neither a polishing nor an extra roughening step. Surface roughening (Hacking et al., 2012) and/or coating with hydroxyapatite (Chen et al., 2017; Lanz et al., 2013; Ortiz-Rios et al., 2018) have been successfully employed before and might be considered to further promote osseointegration.

### Future refinements of the connector-chamber implant

Regarding the footless connector chamber, based on our experience from its first use in Monkey C, we have already implemented the following refinements for the implant of Monkey K:

In an attempt to minimize even further the risk for skin retraction, our future connector chamber is designed with a cylindrical shape, thus allowing for a circular skin incision to be performed, in a similar fashion to the method described for headposts in this paper, that is with a punch tool (see section 'Top-part implantation' and Fig. 2.7). We expect this improvement to lead to a better skin incision and to prevent the need for any corrective procedure (such as the one described in section 'Implantation of the connector-chamber top part and electrode arrays').

The baseplate side screws are designed to be inserted at a 25-degree angle above the skull surface, rather than horizontally. This will ease the handling of the screwdriver during surgery, allowing the screw to find its thread axis without having the screwdriver pressing too much downwards on the surrounding soft tissues.

As discussed in section 2.3, the cap will in the future be fastened exclusively from the top of the implant, without the use of any side screw. The O-ring will also be moved to the upper face, leaving the sides of the implant free of any design feature apart from the baseplate side-screw holes. We expect those smoother side walls to facilitate the daily cleaning procedure and improve the wound margin condition.

Finally, the cable outlet of the pedestal will be horizontal rather than vertical. The wires will therefore leave the pedestal side by side, as close as possible to the skull surface, minimizing the amount of bone cement needed to embed them.

These design changes have allowed to reduce the implant footprint to 531 mm<sup>2</sup>, to be compared with the 546 mm<sup>2</sup> of the previous design iteration. The maximum baseplate height was reduced from 7.0 mm down to 5.6 mm.

## **Supplementary materials**

To facilitate the transfer of our methods to other laboratories, we share the models of the implants and tools that we developed (https://doi.org/10.5281/ zenodo.7300042). Suppl. Table 2.3 provides a summary of the shared files and formats. For an easy and interactive visualization of the models, open the respective "eDrawings" files (.html format).

#### **Author Contributions**

Eleni Psarou: Conceptualization, Methodology, Investigation, Visualization, Writing - original draft, Writing - review & editing. Julien Vezoli: Methodology, Writing review & editing. Marieke Schölvinck: Conceptualization, Methodology, Writing – review & editing, Supervision, Project administration, Resource, Funding acquisition. Pierre-Antoine Ferracci: Methodology, Visualization, Writing – review & editing. Yufeng Zhang: Visualization, Writing – review & editing Iris Grothe: Methodology, Writing – review & editing. **Rasmus Roese**: Investigation, Writing – review & editing. Pascal Fries: Conceptualization, Methodology, Investigation, Writing – original draft, Writing - review & editing, Supervision, Project administration, Resources, Funding acquisition.

## **Declaration of Competing Interests**

P.F. has a patent on thin-film electrodes (US20170181707A1) and is beneficiary of a respective license contract with Blackrock Microsystems LLC (Salt Lake City, UT). P.F. is member of the Advisory Board of CorTec GmbH (Freiburg, Germany). The authors declare no further competing interests.

# **Acknowledgements**

We thank the technical service team of the Ernst Strüngmann Institute and especially David Konietzny, Georg Haas, Thomas Bischoff, Joscha Schmiedt and Kai Rönnburg for their exceptional technical support and valuable contribution to all technical advances described in this work. We also thank Marianne Hartmann, Julia Hoffmann, Sabrina Wallrath, Olga Arne, and Johanna Klon-Lipok for their assistance in surgical procedures and animal care. We are grateful to Dr. Christa Tandi, Dr. Alf Theisen and Dr.Christiane Kiefert who provided excellent veterinary care and advice. We thank Alina Peter, Georgios Spyropoulos, Jarrod Dowdall and Tommaso Tosato who were involved in some of the experiments with the monkeys on whom this paper reports.

### **Supplementary materials**

#### **Supplementary tables**

**Suppl. Table 2.1.** Specifications of CT scans used in headpost planning per monkey.

Brilliance Scanner								
Monkey Name	Scan Options	Protocol Name	Slice Thickness					
M.L.	helix	Felsenbein kinder/Ear*	0.8					
M. Sk.	u .	И	0.8					
M. D.	II .	и	0.8					
M. G.	II .	и	0.8					
M. Hu.	u	и	0.8					
M.T.	II .	И	0.8					
M. M.	II .	И	0.8					
Planmosa Scannor			-					

#### **Planmeca Scanner**

Monkey Name	Body Part Examined	Slice Thickness	Height	
M. Ch.	head	0.4	500	
M. St.	ıı .	0.15	1068	
M. H.	ıı .	0.15	1068	
M. C.	и	0.2	1001	
M. K.	ıı .	0.15	1068	

<sup>\*</sup> The protocol has the German name "Felsenbein Kinder", which in English corresponds to "petrous part of the temporal bone in children"

Spacing between slices	KVP (kV)	X-ray Tube Current (mA)	Rows/ Columns	Pixel Spacing
0.4	90	53	1024	0.1953
0.8	90	53	768	0.2357
0.8	90	53	768	0.1745
0.4	90	53	768	0.2422
0.8	90	53	768	0.1927
0.4	90	53	768	0.2031
0.8	90	107	768	0.2604

Width	KVP (kV)	X-ray Tube Current (mA)	Rows/ Columns	Pixel Spacing
500	90	5	500	0.4
1068	90	8	1068	0.15
1068	90	5	1068	0.15
1001	90	5	1001	0.2
1068	90	5	1068	0.15

**Suppl. Table 2.2.** Bending tools used to pre-surgically customize the headpost baseplate.

Tool name	Manufacturer	System	Code	Comments
bending iron	DePuy Synthes	Compact 2.4	397.371	-
bending pliers with nose		UniLOCK	329.142	Used only for acute angles.

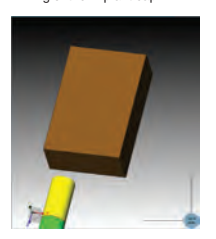
**Suppl. Table 2.3.** List of shared files.

	File for	mat		Comments	
Implants/Tools	.STEP	.STL	Technical drawing	eDrawings (.html)	
Headpost implant					
bent baseplate	✓	✓	✓	✓	
CNC-milled, frontal baseplate	$\checkmark$	$\checkmark$		✓	Monkey H
CNC-milled, central baseplate	$\checkmark$	$\checkmark$		✓	Monkey C
top part	✓	$\checkmark$	✓	✓	
Connector-chamber Implant	✓	✓		✓	*
Implantation instruments					
punch tool- version 1	✓			✓	
punch tool- version 2	✓			✓	Punch tool with corneal trephine.
holding tool	✓	✓		✓	Used in top-part implantation.
ear-bar tip	✓	$\checkmark$		✓	
Lab tools					
headpost holder	✓			✓	
headpost-holder mount	✓			✓	Mounted on primate chair.
tightening tool	✓			✓	For the headpost- holder mount.

<sup>\*</sup>Note that the bone screw models in the connector-chamber assembly are only a coarse approximation of the employed screws, and they cannot be used for screw manufacturing.

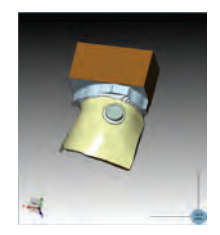
#### Supplementary figures

Sten 1: Milling of the implant cap

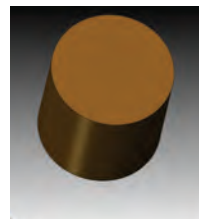
















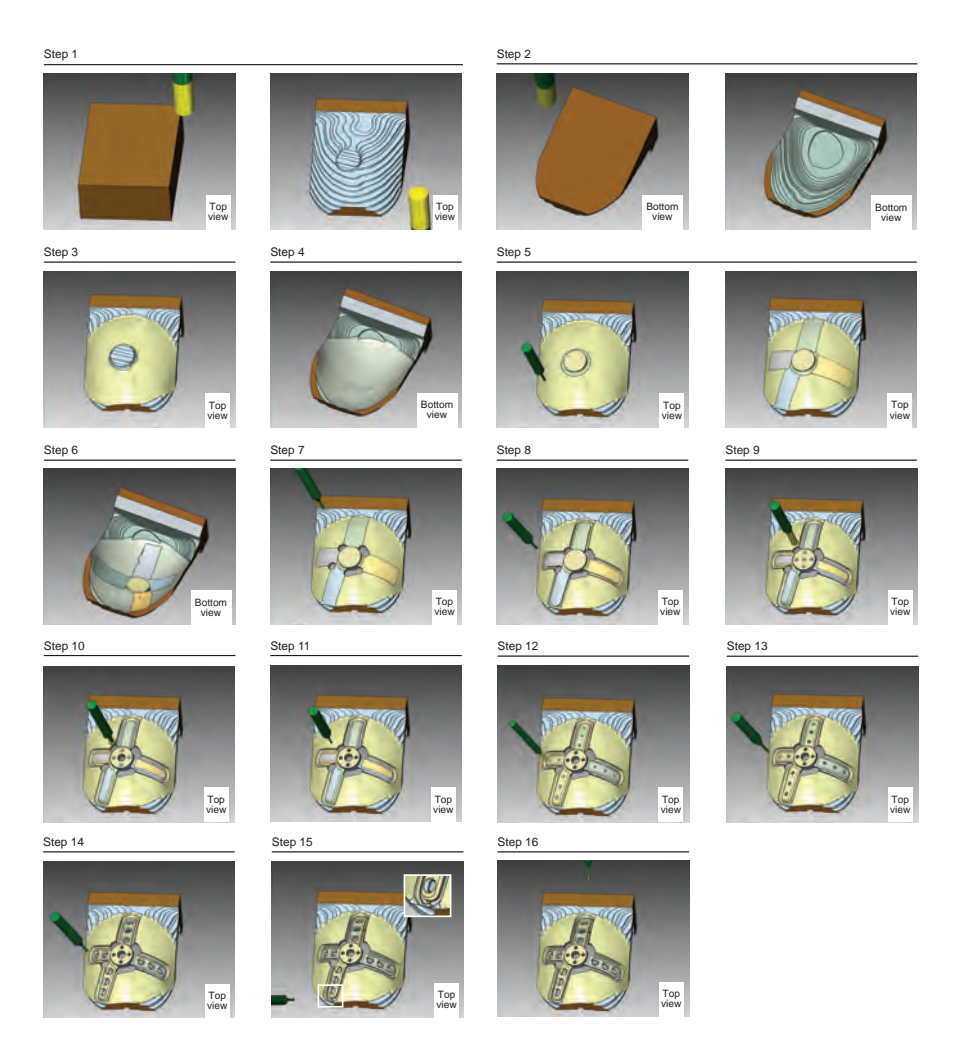


Step 3: Mounting of the implant cap



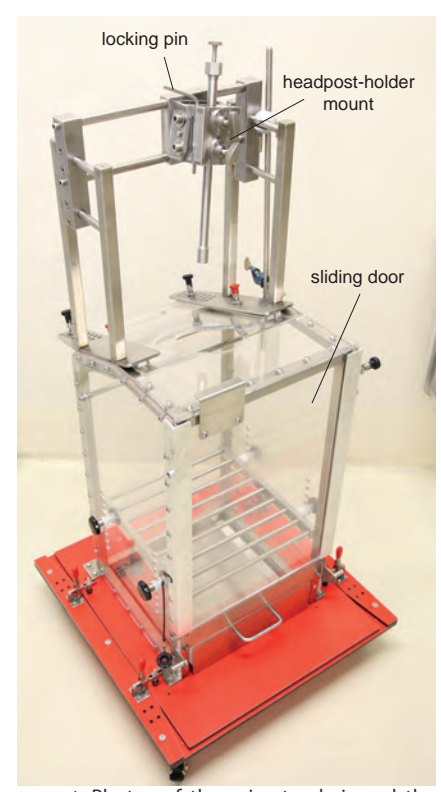


Suppl. Figure 2.1. CNC-milling of a headpost baseplate using the "fake skull" approach. This figure presents a clamping approach that was used to CNC-mill the frontal headpost baseplate for Monkey H (see implant in Fig. 2.2B-C, Fig. 2.3A and Fig. 2.6). Step 1: An "implant cap" was milled which incorporated the overall area of the baseplate implant. At this stage, the baseplate was milled in all details, except for its contour. Thus, the implant cap included: a) the precise geometry of the bottom and upper implant surfaces, b) the central plate and c) the bone screw holes (as shown in Step 3). Step 2: In order to ensure proper clamping and support of the thin implant cap while milling its implant contour, we devised the following approach: A head model (referred to as "fake skull") was produced 1) which served as a base on which the implant cap was mounted, 2) which provided sufficient support to the implant legs while milling their contour, 3) which was easily clamped. The fake skull was milled from stainless steel and featured screw holes that were used to attach the implant cap on it using its bone-screw holes. Step 3: The implant cap was secured on the fake skull and its contour was milled. The final baseplate implant was then released from the fake skull. With this approach we were able to produce a headpost baseplate that showed an excellent fit both on the 3D skull replica of the monkey (Fig. 2.2B-C) and on the real monkey skull during implantation (Fig. 2.6). Nevertheless, it had two main disadvantages; 1) it was time consuming because it required the planning and milling of an additional piece (fake skull); 2) special attention had to be given to avoid imprecisions that could emerge while re-clamping the implant cap using the fake skull. For these reasons, we moved to the simplified approach presented in Suppl. Figure 2.2.

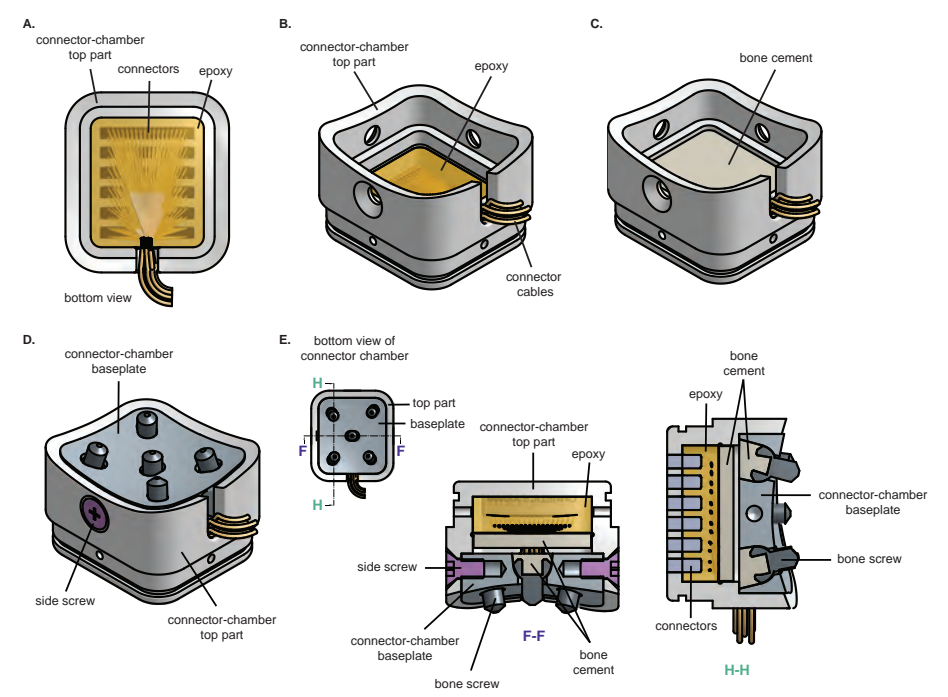


Suppl. Figure 2.2. Supplementary Figure 2. CNC-milling of a headpost baseplate without a "fake skull". Graphical illustration of the CNC-milling steps of a headpost baseplate without the use of a "fake skull", illustrated here for the central headpost-baseplate version (see Fig. 2.3B). The CNC-milling procedure contained the following steps: (1-2) A block of titanium was clamped from one side and a relatively thick cap was milled on the top and then on its bottom surface; this cap coarsely followed the outer skull surface in the overall implant area. More precisely, the cap corresponded to this surface plus 0.5 mm of material on the concave surface, and plus 0.5 mm of material on the convex surface. (3-4) Additional milling produced a more detailed surface (target implant surface plus 0.1 mm on the top and bottom surface). (5-6) In the next steps, the area of the implant was precisely milled to match the final surface. (7) The contour of the implant central plate was milled and then, (8) the upper part of the contour of the implant legs. (9-11) The central screw hole and the pin holes of the central plate were drilled. (12-14) The bone-screw holes were milled. (15) The baseplate was then partially detached from the cap by milling along its contours, while leaving four bridges, one bridge between each baseplate leg and the cap (see inset). These bridges ensured that the implant stayed attached to the cap. (16) In a final step, those bridges were milled away; to keep the baseplate in place during this procedure, highperformance tape (gaffer tape) was applied away from the bridges.





Suppl. Figure 2.3. Primate chair and headpost-holder mount. Photos of the primate chair and the headpost-holder mount. The headpost holder is secured to a mount that is attached to the primate chair. The orientation of the mount can be adjusted to accommodate oblique headpost-holder orientations.



Suppl. Figure 2.4. Sealing of electrode connectors in the connector-chamber top part. (A-B) The Omnetics connectors were incorporated in the top part, and the free space was filled with epoxy. (C) Subsequently, the epoxy was covered with a thin layer of bone cement to provide an extra layer of sealing against fluids. (D) The connector-chamber top part is shown mounted onto the baseplate. (E) Cross-sections (F-F and H-H) of the connector-chamber implant.



# Chapter 3

# Rethinking sample sizes in NHP research

In preparation as: Psarou, E., Katsanevaki, C., Maris, E.\*, and Fries P.\*. Would you agree if N is three? On statistical inference for small N.

\* These authors contributed equally to this study.

#### **Abstract**

Non-human primate studies traditionally use two or three animals. Fries and Maris (2022) previously used standard statistics to argue for using either one animal, for an inference on that sample, or five or more animals, for a useful inference on the population. A recently proposed framework argued for testing three animals and accepting the outcome found in the majority as the outcome that is most representative for the population. The proposal tests this framework under various assumptions about the true probability of the representative outcome in the population, i.e. its typicality. On this basis, it argues that the framework is valid across a wide range of typicalities. Here, we show (1) that the error rate of the framework depends strongly on the typicality of representative outcomes, (2) that an acceptable error rate requires this typicality to be very high (87% for a single type of outlier), which actually renders empirical testing beyond a single animal obsolete, (3) that moving from one to three animals decreases error rates mainly for typicality values of 70-90%, and much less for both lower and higher values. Furthermore, we use conjunction analysis to demonstrate that two out of three animals with a given outcome only allow to infer a lower bound to typicality of 9%, which is of limited value. Thus, the use of two or three animals does not allow a useful inference on the population, and if this option is nevertheless chosen, the inferred lower bound of typicality should be reported.

#### Introduction

Fries and Maris (2022) have recently argued that a sample of two or few (less than five) subjects allows useful inferences only on that sample but not on the population. On this basis, the authors recommended to either use a sample of one and make an inference on that sample, or to use a sample of five or more animals and make a useful inference on the population. They also discouraged using the traditional approach in non-human primate (NHP) research of using two or three animals, because this doubles or triples the number of animals, while the inference remains limited to the sample.

Subsequently, a framework was suggested that attempts to draw an inference on the representativeness of an outcome in the population by studying a small number of animals. This framework (1) suggests to "assume that, in each animal, an experiment can lead to a number of qualitatively distinct outcomes", (2) suggests to "assume a prior distribution across all possible outcomes", calling "the most likely outcome the 'representative' outcome and other 'outliers'", (3) considers outlier proportions in the range of 10 to 20%, (4) considers an outcome as representative when the outcome is present in the majority of the tested animals, (5) concludes that requiring two out of three subjects to show an effect strikes an efficient balance between the proportion of correct conclusions and inconclusive outcomes, (6) claims that this conclusion holds "across a wide range of prior distributions" (Laurens, 2022). Here, we critically discuss the proposed framework and conclude that it has serious shortcomings. We note that the term "prior distribution" should not be confused with a prior distribution in a Bayesian framework, and that the framework of Laurens actually does not allow to specify a prior distribution in the Bayesian sense. Most importantly, we show that the framework will only produce an acceptable inference for a narrow range of outcome distributions. We also present a way to estimate a lower bound to the representativeness of an outcome, the so called typicality, for a range of M animals tested and N animals showing the outcome. We recommend that this lower bound of typicality is reported in studies that try to draw an inference on the population based on a small number of animals.

#### Discussion

#### The concept of typicality

The probability of a given test outcome in a population is referred to as the typicality of that outcome in that population. The concept of typicality is central to a technique that has been called conjunction analysis (Friston et al., 1999). A conjunction analysis first tests for a given outcome (e.g. an effect or a trait) in each subject of a sample. It then uses the proportion of the sample with a given outcome to draw an inference on the proportion of the population that would give the same outcome. This proportion of the population is called typicality y. A useful lower bound to typicality, yc, can be estimated if the false-positive and false-negative rates of the employed tests are specified (Friston et al., 1999), and this is explained in more detail below.

#### The N-oo-M framework

The framework proposed by Laurens (2022) starts with tests for each investigated subject and counts in a sample of M subjects the number N of subjects showing a given test outcome. The framework refers to this as N-out-of-M, or NooM, and refers to e.g. 2 out of 3 tested subjects showing a given outcome as 2003. By counting the number of animals with a given outcome, the framework aims at drawing a binary inference on whether the outcome is representative of the population or not. An outcome is considered representative when it is present in the majority of the tested subjects, i.e. at least two subjects should show the effect in the 2-oo-3 case.

Importantly, the N-oo-M framework suggests to "assume a prior distribution across all possible outcomes", calling "the most likely outcome the 'representative' outcome and other 'outliers'". Note that assuming "a prior distribution across all possible outcomes" is not an assumption in the usual sense, because an outcome always has some probability/typicality, and this just follows from the fact that it is a random variable. Conjunction analysis considers one such probability as the parameter of interest and derives a lower bound for this probability/typicality.

The use of the term "prior distribution" may cause confusion among readers that are familiar with Bayesian inference. The framework of Laurens (2022) is not Bayesian, because if it were Bayesian one would have to specify a prior probability distribution for the parameters, and here this would be typicality y (which in turn specifies the distribution of the outcomes, with probability v for the representative outcome, and 1-y for the outlier). Because this is a probability, the prior distribution would have a support over the interval (0,1), and usually this is the beta distribution. Combining this prior with the information in the data produces a posterior distribution (via Bayes' rule) that is a reweighting over the interval (0,1): segments that were a priori likely/unlikely to contain the true typicality value can be down/ upweighted according to the information in the data. Crucially, if this prior were not an interval but a fixed value (e.g.: γ=0.8), there would be no space for down/

upweighting. If y is a fixed value and it is known, then one also knows the most representative outcome, and no data are required. If, on the other hand, y is a fixed unknown value, then data can be used to estimate its value (e.g., by means of a confidence interval).

#### Probability of incorrect conclusions depends on assumed probability of outliers

If the N-oo-M framework correctly identifies the representative outcome, it defines this as "correct conclusion". Here, we refer to the probability of correct conclusions as  $\pi$ , to the probability of incorrect conclusions (excluding cases considered "inconclusive" by Laurens (2022)) as  $\delta$  and the probability of outliers as  $\omega$ . The N-oo-M framework suggests to specify the probability of outliers as a "prior" (in the sense of Laurens (2022), see above) and claims that "the N-out-of-M model leads to a similar conclusion across a wide range of prior distributions." However, Laurens (2022) considers  $\omega$ -values merely in the relatively narrow range of 10% to 20%, with percentages able to accumulate over different outlier types, including experimental errors. We argue that both, the distributions of outlier probabilities over outlier types, and the total outlier probability, considered by Laurens (2022) are arbitrary.

Fig. 1C of Laurens (2022) shows that with a single type of outlier and with  $\omega = 10\%$ , 2003 reaches  $\delta$  =2.8%. However, our Fig. 3.1A shows that for larger values of  $\omega$ , the  $\delta$  increases steeply (light blue curve in Fig. 3.1A). Already for an  $\omega$  value of 20%, the  $\delta$  rises to 10.4%, which is more than twice the generally accepted error rate of 5%. Laurens (2022) actually rejected 1-oo-1 at  $\omega = 10\%$ , because of  $\delta = 10\%$ . Laurens (2022) does actually consider an example with a total  $\omega = 20\%$ , yet this  $\omega$  is distributed over three types of outliers occurring at 10%, 5% and 5%, respectively (Fig. 2A of Laurens (2022)), and this specific distribution leads to an  $\delta$  just below 5%, namely at 4.3%. However, we note that this scenario entails an additional possibility of inconclusive cases, which occur at 6.1%. Even more worrisome is the fact that this still favorable outcome depends on the precise distribution of  $\omega$  over several outlier types. If a total  $\omega$  of 20% were due e.g. to two types of outliers of 15% and 5%, then  $\delta$  would be 6.8% and thereby higher than the accepted error rate of 5%.

#### A high and immutable prior on the typicality of representatives renders experiments obsolete

Considering all possible combinations of several outlier types is intractable, so we focus in the following on the simple case of one outlier type, yet the reasoning holds for more than one outlier type with correspondingly adjusted numerical results. The blue line in Fig. 3.1A shows that  $\delta$  starts exceeding the generally accepted error rate of 5% for a probability of outliers ( $\omega$ -value) above 13%, corresponding to a typicality of representatives below 87%. Thus, the 2-oo-3 framework only produces an acceptable error rate for a typicality of representatives of 87% or higher. Here, we point out that if the typicality of representatives has to be >87%, this makes it meaningless to collect empirical data beyond a single animal. Remember that the framework aims at a binary decision about which outcome is representative for the population. Yet, for a typicality of representatives >87%, this decision is obsolete.

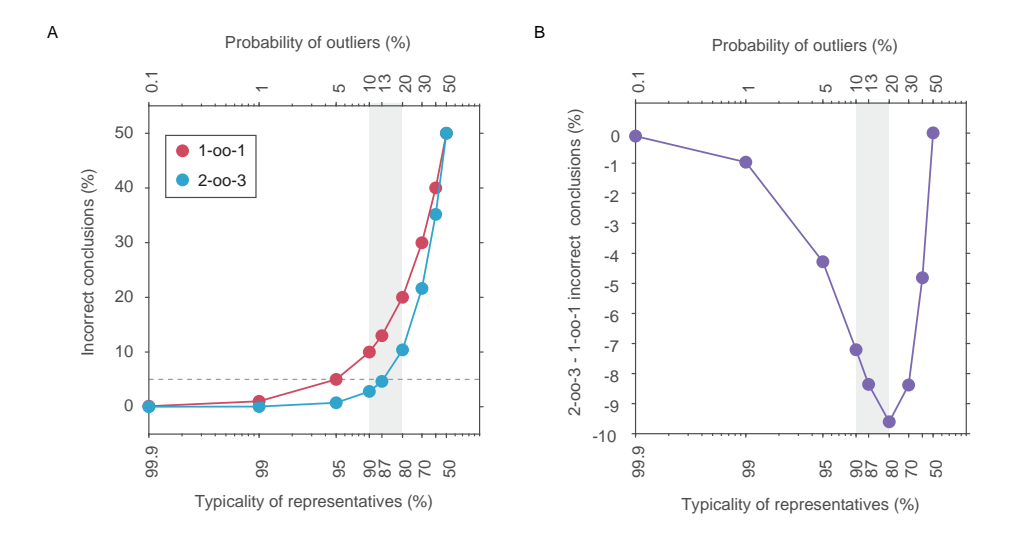


**Figure 3.1.** (**A**) The percentage of incorrect conclusions ( $\delta$ ) as a function of the percentage of the assumed typicality of representatives (bottom x-axis) and the assumed typicality of outliers ( $\omega$ , top x-axis), for a single type of outliers, and separately for 2003 (blue), and 1001 (red). (**B**) The reduction in  $\delta$  for 2003 versus 1001. The grey shading indicates the range of outlier proportions considered in Laurens (2022)

#### 2-00-3 versus 1-00-1

The core of the argument presented in favor of the proposed 2-oo-3 framework is a reduction of  $\delta$  for 2-oo-3 compared to 1-oo-1. The  $\delta$  values for 1-oo-1 are shown in Fig. 3.1A as red line, for 2-oo-3 as blue line, and their difference is shown in Fig. 3.1B. Here, we point out that the reductions of  $\delta$  that are obtained by moving from 1-oo-1 to 2-oo-3 are a function of  $\omega$ , and they peak at  $\omega$  values around 10-30%, close to the ones chosen by Laurens (2022), but they strongly diminish for both larger and smaller  $\omega$  values.

#### Two to three animals allow only limited inferences on the population

The N-oo-M framework can be evaluated through the perspective of conjunction analysis. Conjunction analysis makes no assumption about the typicality of an outcome, but instead it makes an inference on the typicality. More specifically, conjunction analysis uses the proportion of the sample that shows an outcome to infer the lower bound of typicality (Friston et al., 1999). This inference is directly related to the statistics of a binomial distribution, which is defined as follows:

$$P(N = i) = {M \choose i} p^{i} (1 - p)^{M - i}$$
 [1]

A binomial distribution with parameters M and p is the discrete probability distribution of the number of successes N in a sequence of M independent experiments, each asking a yes-no question, and each with its own Boolean-valued outcome: success (with probability p) or failure (with probability q = 1 - p) (adapted from Wikipedia contributors (2023)).

When p is not known, but M and N are known, we can calculate a confidence interval for p (Clopper and Pearson, 1934). Fig. 3.2A shows the two-sided 95% confidence intervals for the success rate p as a function of the ratio of animals showing the effect, for M = 1, 2, 3, 4, 5, 10 tested animals (for  $M \ge 10$ , see Fig. 4 of Clopper and Pearson (1934)). This figure nicely illustrates that increasing numbers of animals lead to decreasing widths of the confidence intervals, and an infinite number of animals would let the confidence interval shrink to the diagonal.

We now have to consider that the outcomes of empirical tests in individual subjects are imperfect and are characterized by (1) the false-positive rate,  $\alpha$ , of the individual tests, and (2) the true-positive rate,  $\beta$ , of the individual tests, also referred to as sensitivity. Thus, the probability p of a significant statistical test is not identical to the true typicality y in the population, but is a monotone function of this typicality:

$$p = (\gamma \beta) + ((1 - \gamma \gamma) \alpha)$$
 [2]

, leading to

$$p = \alpha + (\beta - \alpha)\gamma \tag{3}$$

, and then to

$$\gamma = \frac{p - \alpha}{\beta - \alpha} \tag{4}$$

For  $\alpha$  and  $\beta$ , standard assumptions are:  $\alpha = 0.05$ ,  $\beta = 1$ . The sensitivity  $\beta$  can neither be controlled nor is it known; If we assumed  $\beta$  to be less than 1, the equation shows that the estimate for  $\gamma$  would increase without limit, which is meaningless, and therefore the conservative assumption has to be made that  $\beta$  is one, as has been discussed previously (Fries and Maris, 2022; Friston et al., 1999).

By plugging the standard assumptions for  $\alpha$  and  $\beta$ , and the 95% confidence intervals for the success rate p (see Fig. 3.2A), into equation [4], we obtain the two-sided 95% confidence intervals for the typicality, expressed as a function of the ratio N/M (Fig. 3.2B).

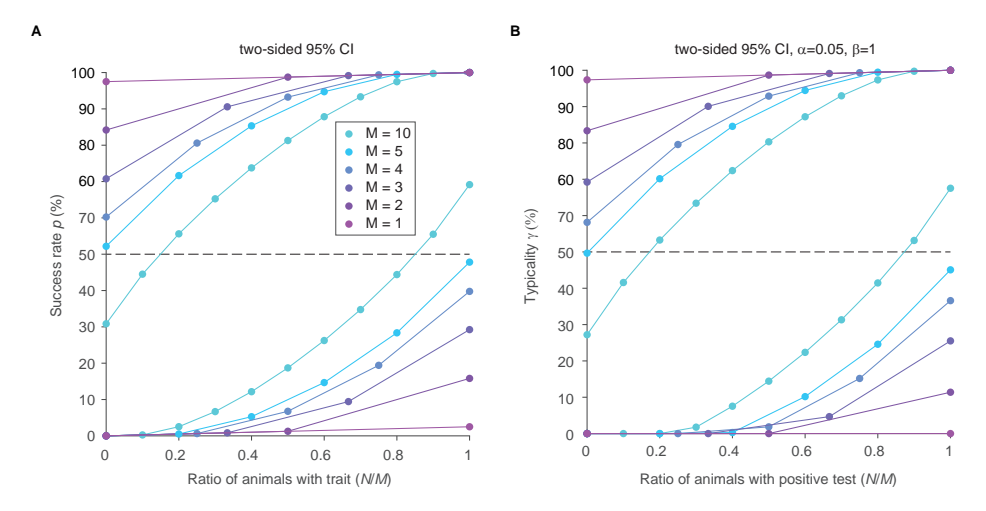


**Figure 3.2. (A)** Two-sided 95% confidence intervals (CI) for the success rate (p, expressed in percentage) as a function of the ratio of animals with the trait, following Clopper and Pearson (1934). The color legend specifies the different numbers M of tested animals. For each M, two lines are plotted, corresponding to the upper and the lower limit of the two-sided 95% confidence interval. (**B**) Same as (A), but for the typicality  $\gamma$ .

Because we want a conservative estimate, from these confidence intervals, we need to use the lower bound for typicality, which we refer to as  $\gamma_c$ . Fig. 3.3A and Table 3.1 show  $\gamma_c$  as a function of N given different values of M, and reveal that  $\gamma_c$  for 2002 is merely 11%, and  $\gamma_c$  for 2003 is merely 5%. Fries and Maris (2022) have previously proposed that 50% is the lowest useful value for typicality, because it corresponds to the expected presence of an effect in a simple majority of the population (Fries and Maris, 2022).

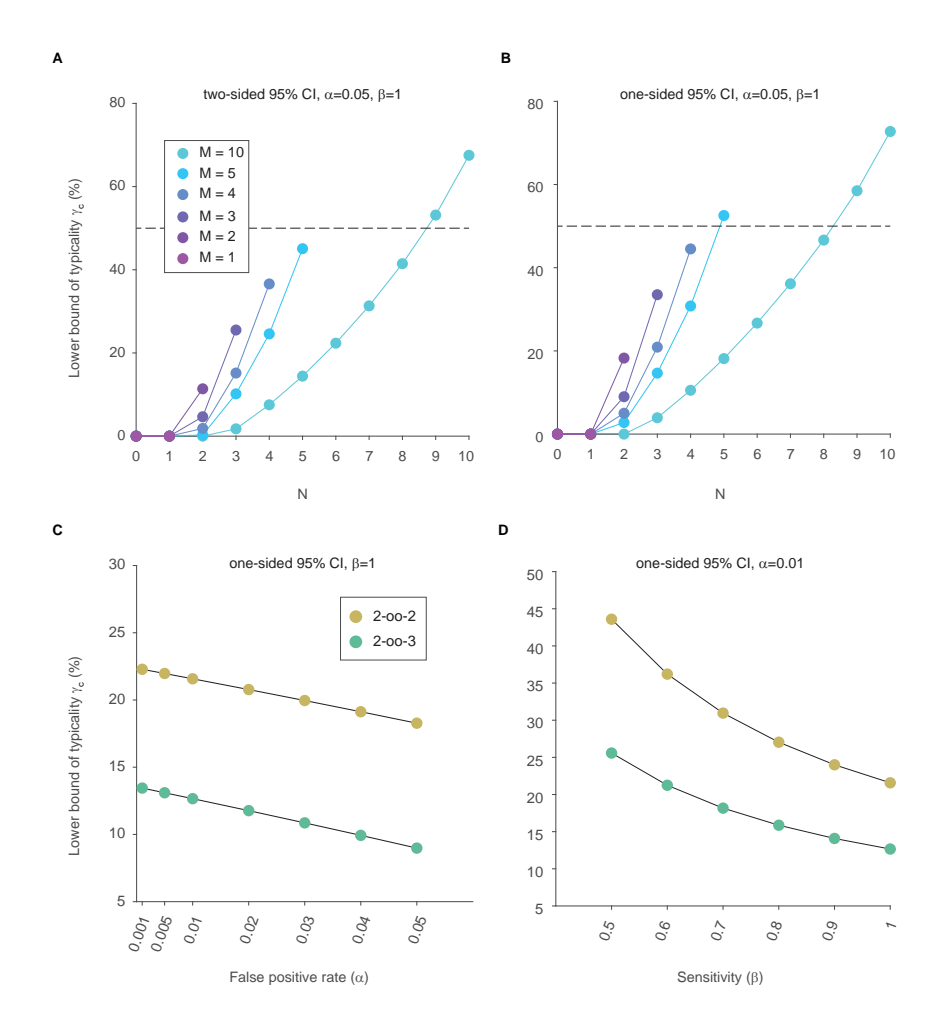


**Figure 3.3. (A)** The lower bound ( $\gamma_c$  expressed as percentage) of the two-sided 95% confidence interval for the typicality ( $\gamma$ ), as a function of N, the number of animals showing an effect (i.e. an individually significant test), and M, the number of animals tested. The false-positive rate  $\alpha$  was set to 0.05, and the sensitivity  $\beta$  was assumed to be 1, as explained in the main text. (**B**) Same as (A), but using one-sided 95% confidence intervals. (**C**)  $\gamma_c$  as a function of the false-positive rate  $\alpha$ , with the sensitivity  $\beta$  fixed at a value of 1, and using one-sided 95% confidence intervals. (**D**)  $\gamma_c$  as a function of the sensitivity  $\beta$ , with the false-positive rate  $\alpha$  fixed at a value 0.01, and using one-sided 95% confidence intervals. Higher values of  $\alpha$ , like the standard value of 0.05, would lead to even lower  $\gamma_c$ . This plot of  $\gamma_c$  as a function of decreasing  $\beta$  is merely to illustrate the effect, while we maintain that  $\beta$  needs to be assumed to be 1, as previously discussed (Fries and Maris, 2022; Friston et al., 1999). For (**C**) and (**D**): If we had assumed two-sided 95% confidence intervals, the values of  $\gamma_c$  would be even lower.

We so far only used two-sided confidence intervals. However, even when using onesided confidence intervals (Fries and Maris, 2022; Friston et al., 1999), γ<sub>c</sub> for 2002 is merely 18%, and  $\gamma_c$  for 2003 is merely 9%, thus far below 50% (Fig. 3B and Table 2).

Table 1 and Table 2 report the precise  $\gamma_c$  values for all possible outcomes up to N=M=10, to aid the reporting of  $\gamma_c$  values in studies that opt for this approach.

Investigators might choose a lower false-positive rate  $\alpha$  for their individual tests, and this will increase the resulting  $\gamma_c$ . However, even strong reductions of  $\alpha$  leave  $\gamma_c$ far below 50%, for both 2002 and 2003 (Fig. 3.3C).

Thus, the 2003 framework leads to  $\gamma_c$  values that correspond to inferences on very limited proportions of the population. Useful inferences based on 2002 or 2003 remain limited to the sample of investigated animals (Fries and Maris, 2022). Such an inference on the sample of animals is also reached with 1001. Therefore, compared to 1001, the proposal of 2002 or 2003 does not provide a gain in the quality of the inference, while at the same time doubling or even tripling the number of animals used.

It might be argued that the assumption of  $\beta = 1$  is necessary on theoretical grounds (see above), but that this assumption will also be wrong, because the true sensitivity will most likely never be perfect. Therefore, we explored the influence of lowering the assumption for  $\beta$ . As mentioned above, reducing  $\beta$  to arbitrarily low values will increase  $\gamma_c$  without limit and is therefore meaningless. Nevertheless, we considered reductions of  $\beta$  to a value of 0.5, which means that the test in individual subjects is so insensitive that it misses half of the subjects with an effect (or trait). Even with such strong reductions of  $\beta$ , the estimate of  $\gamma_c$  remains below 50% (Fig. 3.3D), both for the 2002 and for the 2003 case, and with  $\alpha$  already reduced to 0.01.

 $\textbf{Table 3.1.} \ \text{The lower bound } (\gamma_{c'} \ \text{expressed as percentage}) \ \text{of the two-sided 95\% confidence interval for } (\gamma_{c'} \ \text{expressed as percentage}) \ \text{of the two-sided 95\% confidence interval for } (\gamma_{c'} \ \text{expressed as percentage}) \ \text{of the two-sided 95\% confidence interval for } (\gamma_{c'} \ \text{expressed as percentage}) \ \text{of the two-sided 95\% confidence interval for } (\gamma_{c'} \ \text{expressed as percentage}) \ \text{of the two-sided 95\% confidence interval for } (\gamma_{c'} \ \text{expressed as percentage}) \ \text{of the two-sided 95\% confidence interval for } (\gamma_{c'} \ \text{expressed as percentage}) \ \text{of the two-sided 95\% confidence interval for } (\gamma_{c'} \ \text{expressed as percentage}) \ \text{of the two-sided 95\% confidence interval for } (\gamma_{c'} \ \text{expressed as percentage}) \ \text{of the two-sided 95\% confidence interval for } (\gamma_{c'} \ \text{expressed as percentage}) \ \text{of the two-sided 95\% confidence}$ the typicality (y), as a function of the number of animals showing an effect (N) out of the number of tested animals (M), with  $\alpha$ = 0.05 and  $\beta$ =1.

N M	0	1	2	3	4	5	6	7	8	9	10
1	0	0									
2	0	0	11.4								
3	0	0	4.7	25.5							
4	0	0	1.9	15.2	36.6						
5	0	0	0.3	10.2	24.6	45.1					
6	0	0	0	7.2	18.2	32.5	51.7				
7	0	0	0	5.2	14.1	25.3	39.1	56.9			
8	0	0	0	3.7	11.3	20.5	31.5	44.6	61.1		
9	0	0	0	2.6	9.2	17.1	26.2	36.8	49.2	64.6	
10	0	0	0	1.8	7.5	14.4	22.4	31.3	41.5	53.2	67.5

**Table 3.2.** The lower bound ( $\gamma_c$ , expressed as percentage) of the one-sided 95% confidence interval for the typicality (y), as a function of the number of animals showing an effect (N) out of the number of tested animals (M), with  $\alpha$ = 0.05 and  $\beta$ =1.

N M	0	1	2	3	4	5	6	7	8	9	10
1	0	0						,	,		
2	0	0	18.3								
3	0	0	9.0	33.5							
4	0	0	5.0	20.9	44.5						
5	0	0	2.8	14.7	30.8	52.6					
6	0	0	1.4	10.9	23.3	38.8	58.6				
7	0	0	0.4	8.3	18.5	30.7	45.2	63.4			
8	0	0	0	6.4	15.0	25.2	36.9	50.5	67.1		
9	0	0	0	5.0	12.5	21.2	31.0	42.1	54.8	70.2	
10	0	0	0	3.9	10.5	18.2	26.7	36.1	46.6	58.5	72.8

#### Conclusion

In summary, the framework proposed by Laurens (2022) has been an unconventional and welcome addition to the discussion about statistical inferences based on small numbers of animals. However, our analysis revealed that it has serious shortcomings and limitations. If studies nevertheless report the individual outcomes of two or three animals, they should also report the corresponding lower bound of typicality (see Tables 3.1 and 3.2) to avoid the common misconception that the inclusion of a second or third animal would allow a general inference on the population. We maintain the previous conclusion that a useful inference on the population requires at least five animals (Fries and Maris, 2022). This number is currently not realized in typical NHP experiments. Therefore, any useful inference will remain limited to the investigated sample, and this will hold for a sample of three or two animals, or even a single animal. Consequently, we argue that the minimum required number for the publication of a typical NHP study should be one animal, to minimize the use of animals in research

#### **Author Contributions**

Eleni Psarou: Methodology, Software, Formal analysis, Visualization, Writing -Original Draft, Writing - Review & Editing. Christini Katsanevaki: Methodology; Software; Formal analysis; Visualization; Writing - Original Draft; Writing - Review & Editing. Eric Maris: Conceptualization; Methodology; Software; Supervision; Writing - Original Draft; Writing - Review & Editing. Pascal Fries: Conceptualization; Methodology; Resources; Supervision; Project administration; Funding acquisition; Writing - Original Draft; Writing - Review & Editing.

#### Declaration of Interests

P.F. has a patent on thin-film electrodes and is member of the Advisory Board of CorTec GmbH (Freiburg, Germany). The other authors declare to have no competing interests.

#### **Acknowledgements**

We thank Jean Laurens for helpful discussions.



## Chapter 4

# Repetition-related gamma plasticity in macaque V1 and V2 is highly stimulus specific and robust to stimulus set size

In preparation as: Psarou, E., Parto-Dezfouli, M., Grothe, I., Peter, A., Roese, R., and Fries, P. Repetition-related gamma plasticity in macaque V1 and V2 is highly stimulus specific and robust to stimulus set size.

#### **Abstract**

When a visual stimulus is repeated, the cortex has the opportunity to adjust its processing. Indeed, repeated stimuli induce reduced neuronal spike rates and increased neuronal gamma-band synchronization. Previous studies found the repetition-related gamma increase to occur both in human and non-human primates, for artificial and natural stimuli, to persist for minutes and to not transfer between strongly differing stimuli. Here, we further investigated the repetitionrelated effects using laminar recordings of multi-unit activity and local field potentials from awake macaque areas V1 and V2. We find that the effects on spike rate and gamma occur in all laminar compartments of V1 and V2. We quantify the degree of stimulus specificity with oriented gratings and find that the repetitionrelated gamma increase does not transfer to gratings differing by merely 10°, the smallest difference tested. Furthermore, we find that the repetition-related effects are robust to stimulus set size, occurring both when one stimulus was repeated and when eighteen different interleaved stimuli were repeated. Finally, we show that alpha-beta activity increases and remains elevated when a stimulus is repeated, and decreases sharply when an unexpected stimulus is presented. These results suggest that repetition-related plasticity leads to changes in spike rates and rhythmic neuronal synchronization in different frequency bands that adjust the cortical processing of repeated stimuli.

#### Introduction

Under natural conditions, we often stay in a given environment for some time. During such periods, surrounding stimuli typically do not change radically, and thus, the visual input we receive is constrained, i.e. not fully random, but repeating. Additionally, we often revisit with our eyes parts of the visual field that are of particular behavioral interest. For instance, while executing everyday tasks like preparing a cup of tea, we almost exclusively and repeatedly fixate task-relevant objects and parts of the visual field (Hayhoe and Ballard, 2005). All this creates a considerable redundancy in our visual input, and the brain could build on this redundancy in order to optimize the processing of those repeated stimuli.

Previous studies have reported repetition-related plasticity in neuronal activity. Repeated stimuli have been shown to typically induce less spiking (Brunet et al., 2014; Li et al., 1993; Miller et al., 1993; Peter et al., 2021), and reduced hemodynamic responses (Grill-Spector et al., 2006; Sawamura et al., 2005). Interestingly, this repetition-related suppression is not linked to reduced behavioral performance. Instead, behavioral accuracy of both humans (Murakami and Okada, 2015: Stauch et al., 2021) has been found to remain stable or even improve with stimulus repetition; a phenomenon called 'repetition priming' (McMahon and Olson, 2007; Wiggs and Martin, 1998). How could a significant decrease in spiking activity go hand in hand with sustained or even improved behavioral performance? In other words, what is the mechanism that allows the smaller number of spikes to maintain or even improve their downstream impact?

Increased synchronization at the neuronal network level has been proposed to allow fewer spikes to be transmitted in a more efficient way (Gotts et al., 2012). Indeed, several studies have linked stimulus repetition to increased synchronization (Brunet et al., 2014; Gilbert et al., 2010; Peter et al., 2021; Stauch et al., 2021). In particular, the repetition of visual stimuli has been linked to a profound increase in gamma-band activity within early and mid-level visual areas, as well as gammaband synchronization between them, both in awake macagues (Brunet et al., 2014; Peter et al., 2021) and in human participants (Stauch et al., 2021). Between human visual areas, stimulus repetition predominantly increases bottom-up influences, consistent with increased or maintained information transfer. The abovementioned repetition-related changes have been shown to persist for several minutes (Peter et al., 2021; Stauch et al., 2021), and to be stimulus specific (Peter et al., 2021; Stauch et al., 2021), i.e. they do not transfer to other stimuli that have not been repeated.

So far, the stimulus specificity of the effects has been shown both for gratings (Peter et al., 2021; Stauch et al., 2021) and naturalistic stimuli (Peter et al., 2021). These studies demonstrated that repetition-related plasticity did not transfer between gratings or natural stimuli that had been designed to differ strongly from each other. What happens when the repeated stimuli are more similar to each other? In this study, we systematically investigated the level and extent of stimulus specificity of the repetition-related plasticity. To do so, we used black-and-white gratings whose characteristics can be easily controlled and parameterized. By manipulating in fine steps one dimension, the stimulus orientation, we were able to quantify the specificity of repetition-related plasticity. Importantly, all other stimulus characteristics remained unchanged. At the same time, this paradigm entailed blocks in which a larger number of different stimuli were repeated in an interleaved manner, whereas previous studies had interleaved maximally two to three stimuli (Peter et al., 2021). This enabled us to test whether the repetitionrelated plasticity is also present under those conditions.

Furthermore, repetition is important in the context of theories on predictive coding. Those theories propose that feedforward circuits signal prediction errors, and feedback circuits signal predictions (Friston, 2005; Mumford, 1992; Rao and Ballard, 1999). Feedforward signals emerge primarily from superficial layers of a given area and target granular layers of higher areas (Cragg, 1969; Rockland and Pandya, 1979; Wong-Riley, 1978); feedback signals arise from deep and superficial layers and target deep and superficial layers of the lower areas (Anderson and Martin, 2009; Markov et al., 2013; Rockland and Pandya, 1979; Rockland and Virga, 1989; Wong-Riley, 1978). Thus, prediction/prediction-error related processes might show laminar specificity. Previous studies have shown that cortical rhythms also show a laminar pattern: alpha and beta is more prominent in deep layers (Bastos et al., 2020; Buffalo et al., 2011), while gamma is more prominent in superficial layers (Bastos et al., 2020; Buffalo et al., 2011; Gieselmann and Thiele, 2022; Xing et al., 2012), though some studies report additional gamma peaks in Layer 4B(Xing et al., 2012) and deep layers (Gieselmann and Thiele, 2022; Xing et al., 2012). In agreement with this and the laminar origins of feedforward versus feedback projections, interareal directed influences in gamma are stronger in the feedforward than feedback direction, and influences in alpha/beta are stronger in the feedback than feedforward direction (Bastos et al., 2015; Buschman and Miller, 2007; Michalareas et al., 2016; van Kerkoerle et al., 2014; Vezoli et al., 2021). To investigate whether stimulus repetition leads to distinct changes between layers, we used the abovementioned repetition paradigms while performing laminar recordings using linear probes in the monkey early visual cortex targeting areas V1 and V2.

#### **Materials and Methods**

#### Animals

Electrophysiological recordings were performed in one monkey. The rationale for using a single monkey is explained in more detail in section 'Sample size' of this chapter and Chapter 3. The monkey was implanted with a recording chamber over the occipital pole that allowed laminar access in areas V1 and V2. At the time of electrophysiological recordings, the monkey was 17 years old and weighed 15 kg. All procedures and housing conditions complied with the German and European law for the protection of animals (EU Directive 2010/63/EU for animal experiments). All experimental procedures were approved by the regional authority (Regierungspräsidium Darmstadt, Germany).

#### **Implants**

The implant planning was based on pre-operative MRI (MAGNETOM Trio scanner, 3.0T; Siemens, Munich, Germany) and CT scans (Brilliance 6 scanner, Philips, Amsterdam, Netherlands; and ProMax 3D Mid scanner, Planmeca Oy, Helsinki, Finland) that allowed the extraction of the brain and skull models. First, the monkey was implanted with a cement-free headpost implant over the frontal brain areas (Psarou et al., 2023). A recording chamber was later implanted over the occipital pole. The location and angle of the recording chamber were planned according to the MRI scan. Special care was given so that the angle of the recording chamber allowed perpendicular access to the surface of areas V1 and V2 and thus, laminar cortical access. The bottom surface of the chamber was CNC-milled to follow the underlying skull geometry. A trepanation through the skull was performed 2.4 weeks after chamber implantation, which allowed access to brain areas V1 and V2. For the needs of another experiment (not reported here), a single virus injection was performed at one cortical location (at four different depths) within the trepanation. None of the recording sessions reported here overlapped with the injection site.

#### Data collection

#### Experimental setup

During the experiments, the monkey was head fixed and sat comfortably in a primate chair that was placed in a dimly lit Faraday cage that eliminated powerline noise and attenuated potential external sounds. All behavioral paradigms were designed and controlled by ARCADE, a stimulus presentation software written in MATLAB (Dowdall et al. (2018); https://github.com/esi-neuroscience/ARCADE). All stimuli were presented on an LG 32GK850G-B monitor (LG Electronics Inc., Seoul, South Korea.) with a resolution of 2560 x 1440 (16:9), a size of 697.34 x 392.256 mm, and a refresh rate of 143 Hz. The following 'default picture settings' of the monitor were used: R/G/B: 50/50/50, Gamma Mode 2, Brightness 100, Contrast 70, Color Temperature Custom. The distance from the screen was 83.5 cm. Gamma correction was applied (gamma: 1.57). The exact timing of the stimuli was measured with a photodiode that was attached to one of the corners of the monitor (invisible to the monkey).

#### **Eve position monitoring**

Eye signals of the left eye were recorded at 1 kHz using an Eyelink 1000 system (SR Research, Ottawa, Canada). The system was calibrated at the beginning of each recording session.

#### Behavioral tasks

The stimuli used in the main experimental paradigm were circular patches of static black-and-white grating that always had the following features: diameter of 6.6°, centered at 3 ° to the right of the vertical meridian and 3 ° below the horizontal meridian, spatial frequency of 2 cycles/°, contrast of 100%. Grating orientation varied from 0 ° to 170 ° in steps of 10 °. One orientation was presented per trial. For a given recording session, one orientation was randomly selected as the conditioned orientation and presented in a fixed-orientation block, in which this orientation was presented for 90 consecutive trials; this block is referred to as FIX. Before and after this conditioning, the orientation tuning of the recorded neuronal populations was assessed by presenting all employed orientations in a pseudorandomly interleaved manner, with each orientation being presented 10 times; these trial blocks are referred to as variable-stimulus blocks, VAR1 and VAR2. This allowed us to compare the two orientation tunings, before and after conditioning, and quantify the specificity of conditioning-related changes.

In any given recording session, the monkey completed the following sequence of tasks: 1) Receptive field mapping, 2) Pre-conditioning orientation tuning (VAR1), 3) A block of approximately 10 minutes during which the monkey saw full-field flashes (intended for current-source density analysis, see below), and then could watch natural scenes or close his eyes, 4) Conditioning, i.e. repetition of the conditioned stimulus (FIX), 5) Post-conditioning orientation tuning (VAR2). In all tasks, the monkey was rewarded for maintaining central fixation throughout the trial without additional task requirements. For every correct trial, the monkey was rewarded with a drop of grape juice. While advancing the recording probe into the brain, the monkey occasionally performed additional blocks of full-field flashes.

#### Receptive field mapping

The receptive fields (RFs) were measured using a black moving bar stimulus (bar width: 0.12 °, bar length: 15 °) that was presented on a grey background. In each RF-mapping trial, the bar was presented in one out of four orientations and was moved in one out of two possible directions, both orthogonal to the selected orientation. The bar moved at a speed of 8 °/s and covered the lower right visual quadrant, where the recorded RFs were expected, based on the known retinotopy of the recorded cortex. The monkey had to complete at least 80 correct trials, i.e. ten trials per condition.

#### First and second variable-stimulus repetition block

The first and second variable-stimulus blocks were identical, and are referred to as VAR1 block and VAR2 block, or as VARX when referring to both. A grey background was presented throughout. Each trial started with the presentation of a white fixation point at the center of the screen. To perform a correct trial, the monkey had to turn his eyes towards the fixation point and maintain his gaze within a fixation window of 1-1.2 °radius around it throughout the trial.

Upon entering the fixation window, a baseline period of 0.8-0.9 s started. Then, an oriented grating was presented for 0.9 to 1 s. At the end of the stimulation period, the grating and the fixation point turned off, and a reward period of 0.8 s started during which the monkey received a drop of grape juice as a reward. Then, an intertrial interval (ITI) of 0.5 s followed before the beginning of the next trial (Fig. 4.1A).

On any given trial, the orientation of the presented grating was randomly selected from a pool of 18 possible orientations (0 ° to 170 ° in steps of 10 °; Fig. 4.1B). When a given orientation was presented and the trial was successfully completed, that orientation was removed from the orientation pool. If the monkey broke fixation during a trial, the presented orientation remained in the pool. When all 18 orientations had been successfully presented, this set of trials constituted a completed mini-block. The pool was then refilled with all 18 orientations, and the procedure was repeated. This approach ensured that there were no immediate repetitions of the same orientation.

In VAR1, 10 mini-blocks were collected, so that 10 correct trials per orientation were acquired. In VAR2, at least 10 mini-blocks were collected, and then additional miniblocks were collected until the monkey stopped working.

VAR2 followed immediately after FIX (Fig. 4.1C), i.e. there was only a regular ITI between the last trial of FIX and the first trial of VAR2.

#### **Fixed-stimulus repetition block**

On each recording day, the monkey completed one fixed-stimulus block, referred to as FIX, during which a grating of a fixed orientation was repeated for 90 consecutive trials (Fig. 4.1B). At the beginning of this block, one orientation was randomly selected from the orientation pool (18 possible orientations; same as in VARX). We refer to this stimulus as the "conditioned" stimulus. The trial structure was identical to that of VARX, with the only differences that the baseline period was 1-1.1 s, and the stimulus period was 11.3 s. FIX ended when the monkey had successfully completed 90 correct trials. In case the monkey broke fixation during a trial, the trial was aborted and a period of 0.5 s was followed by the ITI (0.5 s). As mentioned above, the conditioning block was immediately followed by VAR2.

#### **Electrophysiological recordings**

Laminar recordings were performed using linear multi-contact arrays. We used V-probes (Plexon Inc, Dallas, Texas, US) with 24 or 32 contacts and an inter-contact spacing of 100, 125, or 150  $\mu$ m. All electrode arrays had a contact-site diameter of 15  $\mu$ m and a tip-to-first contact distance of 300  $\mu$ m. The diameter of the probes differed depending on their number of contacts. The 24-channel and 32-channel probes had a diameter of 210 and 260 um, respectively. In our analysis, we pooled data from all recording probes. For more details see section 'Laminar Alignment of Recording Sessions'.

On any given recording day, a grid was added in the chamber and a laminar probe was advanced perpendicularly to the brain surface to target area V1. The probe was advanced through a guide tube using a precision hydraulic micromanipulator (MO-972A; Narishige, Tokyo, Japan). The guide tube featured a blunt tip that rested against the dura and provided extra stability to the recording probe. The probe was advanced with a speed of 10  $\mu$ m/s until the first few electrode contacts showed brain activity in the LFP signals. Then, the probe was advanced further at a lower speed (1  $\mu$ m/s) until neuronal activity was present on several recording contacts covering all V1 layers. A few of the most superficial contacts were intentionally kept outside of the brain to ensure coverage of the most superficial cortical layers.

When the target position of the probe was found, the probe was slightly retracted (for 500-1000  $\mu$ m, with a speed of 1  $\mu$ m/s) in order to compensate for and help release potential tissue dimpling. This allowed us to approximately preserve the

target recording position. A similar procedure has been described by Nandy et al. (2017). Probe retraction was followed by a waiting period of 30 minutes to allow the tissue to stabilize before recording. During this period, the monkey could watch videos of natural scenes or sleep.

#### **Electrophysiological signals**

The recording ground was connected to the metal guide tube that protected the probe from bending and stayed outside of the brain with its flat tip resting firmly on the dura. The recording reference was connected to the shank of the linear probe.

Electrophysiological data were acquired with Tucker Davis Technologies systems (TDT, Alachua, Florida, United States). Raw data were recorded and digitized at 24414.0625 Hz using a TDT PZ2 preamplifier. Offline, the raw data were downsampled to 1000 Hz. For the LFP, this was achieved by first upsampling to 3,125,000 Hz, then downsampling to 25,000 Hz, applying an IIR filter with a stopband at 500 Hz and downsampling to 1000 Hz. For the MUA, this was achieved by first upsampling to 3,125,000 Hz, band-pass filtering between 300 and 12000 Hz, rectification, IIR-filtering with a stop-band at 500 Hz and downsampling to 1000 Hz. Note that there was no line-noise removal, because the recordings were done in a Faraday cage that completely avoided line noise.

To give similar weight to each electrode, the LFP and MUA signals were z-standardized before combining data over recording sites and sessions. For this, we first defined all data periods that were later used in the analysis (see below for details). Then, for each electrode and signal type (LFP and MUA), we calculated the mean and SD over all baseline-period data points, and subsequently all data points were z-standardized by subtracting this baseline mean and dividing by this baseline SD.

#### Data analysis

Data analysis was performed with MATLAB (Mathworks, Boston, USA) using the FieldTrip toolbox (Oostenveld et al., 2011).

#### Bipolar derivation

To reduce the influence of volume conduction on the LFP signals, local bipolar derivation was performed and used for all LFP analyses. The bipolar derivation was computed sample-by-sample as the value measured on a given electrode minus the value on the next-lower electrode, and we refer to a bipolar derivation as a (recording) site. We refer to the unipolar LFP as uLFP, and to the bipolar-derived LFP as bl FP.

#### Receptive field analysis

RFs were estimated for each recording site, using similar approaches for MUA and bLFP signals. The MUA signal was low-pass filtered (Butterworth, order 2, backward and forward, low-cut at 100 Hz). For the bLFP signals, the time-resolved power at 40-100 Hz was estimated in time windows of 0.1 s length and in steps of 0.01 s. These neuronal signals were averaged over trials. Average MUA and bLFP responses were then baseline corrected and shifted in time according to the latency that gave the maximum response. We tested latencies between 0.04 and 0.07 s from stimulus onset, in steps of 0.005 s. The resulting responses were back-projected and plotted as activation maps (Fiorani et al., 2014).

#### Estimation of receptive field centers

The centers of MUA and bLFP- RFs were estimated as follows. First, the RF maps were z-scored and then thresholded in order to eliminate noise. In particular, all RF-map elements below 5 SD were set to zero. The resulting RF maps were fitted with 2D-Gaussians (Suppl. Fig. 4.1A). The coordinates of the Gaussian peak were then used to define the x and y coordinates of the RF center. Note the strong correspondence between MUA- and bLFP-RF centers (Suppl. Fig. 4.1B). See Figure 4.1G for an overview of all V1- and V2-RF centers of the recording sessions included in the analysis.

As shown in Figure 4.1G, in two V2 sessions, the RF centers were located just outside of the grating stimulus. Note, however, that portions of these RFs still overlapped with the grating. Thus, these sessions were included in our analysis. Suppl. Figure 4.1C shows the MUA-RF centers of all sessions with simultaneous recordings in V1 and V2.

#### **Laminar Alignment of Recording Sessions**

On any given day, recording channels were first assigned to area V1, area V2, outside of the brain or within the white matter, based on their MUA- and bLFP-RF maps. The most superficial channels on the linear recording probes, which lacked clear RFs and showed less variability in the LFP signal, were considered to be located outside of the cortex. On some recording days, some of the deepest channels on the linear probe reached the underlying area V2. Channels were assigned to V2 when there was an abrupt shift in the eccentricity and an increase in the size of the RF compared to the RFs of the more superficial V1 channels (see example in Fig. 4.1E-

F). Any deep channel (below V1 or between V1 and V2 channels) that lacked clear RFs was considered to be located in the white matter.

Then, V1 and V2 channels were further subdivided into three distinct laminar compartments: superficial, granular (input), or deep. The laminar assignment was informed by the CSD analysis, which allowed us to identify the input layer (Mitzdorf, 1987; Schroeder et al., 1998).

Specifically, we estimated the CSD responses to the presentation of the gratings in the VARX and FIX blocks. We had originally planned to estimate the CSD based on the full-field flashes, but the CSDs based on the VARX or FIX blocks turned out to be more reliable, probably due to the larger number of trials, CSD analysis of LFP signals was performed using the MATLAB file exchange function 'CSD' (Olsen, 2023). The CSD of each channel was estimated per trial and then averaged across trials. For each electrode x, the CSD per trial was calculated using the following equation:

$$CSD(x) = -\sigma \frac{n(x-1)-2n(x)+n(x+1)}{h^2}$$

where,  $\sigma = 0.3$  (s/m) is the conductivity of the extracellular medium, and h is the inter-contact spacing.

To ensure that there was no drift of the recording probe throughout the session, the CSD maps were calculated separately for VAR1, FIX and VAR2. Based on these separate CSD maps, we did not notice drifts of the earliest current sink, and therefore used all maps to inform our decision.

We first describe the procedure to assign electrodes to laminar compartments in V1. The electrode showing the earliest current sink was defined as the input layer 4C (L4C). This was typically confirmed by this electrode also showing the earliest MUA response. On this electrode, the early current sink was consistently followed by a current source. The first or second electrode below the L4C electrode consistently showed a current sink that started after the L4C current sink (Rimehaug et al., 2023; Self et al., 2019). This electrode was defined as the uppermost electrode of the deep laminar compartment. The lowermost electrode of the deep laminar compartment was defined as the lowest electrode showing a clear bLFP-RF with V1 characteristics (see above). The granular compartment was defined to contain the L4C electrode and all electrodes up to 300 µm above L4C. Electrodes above this boundary were defined to be in the superficial laminar compartment (Fig. 4.1H), until the electrodes did not any more show bLFP-RFs. In some sessions, we were able to obtain clear inter-contact coherence maps, as previously described (Maier et al., 2010), which can pinpoint the transition from granular to deep layers. In sessions with such a clear transition, we used this information to further validate our laminar assignment.

The same procedure was applied to assign electrodes to layers in V2 while (1) taking into account that the laminar sequence is inverted (Fig. 4.1H), (2) defining the granular compartment to be only 200  $\mu$ m thick (instead of 300  $\mu$ m in V1, Kelly and Hawken (2017); Ziemba et al. (2019)). In three recording sessions, we obtained only a small coverage of area V2. In these cases, channels covering the first 300  $\mu$ m were considered part of the deep layers of V2.

#### Data inclusion

Our analysis included only behaviorally correct trials. Recording sessions that lacked a clear early current sink were excluded from our laminar analysis. In the case of area V1, sessions that yielded few MUA RFs, such that the MUA RFs spanned < 800 µm of cortical tissue, were excluded from the analysis.

After application of these selection criteria, 16 V1 sessions remained from a total of 22 sessions that targeted V1, and 16 V2 sessions remained from a total of 16 sessions that targeted V2. Seven channels from 3 sessions were excluded due to the presence of strong artefacts in multiple trials.

The quality of spiking activity showed a large variation between sessions and channels. To ensure that only channels with clear visually induced spiking responses were included in our analysis, we performed the following procedure: For each session and channel, a sign test was performed on the data from the first variable-stimulus block to assess if there is a significant increase in the spiking activity around the onset of the visual stimulus. Only channels that showed a significant increase in their spiking activity between the baseline (-0.2 to 0 s) and the stimulus presentation period (0 to 0.2 s) were included in further analysis of spiking activity.

In the analysis of intra-areal GC, we noticed that one session produced outlier results for V2. Specifically, when we calculated the mean and SD across the GC values from all V2 sessions, this session exceeded the mean plus 4 SD, and we therefore excluded it from the GC analysis.

iammar compa	iammar Compartment.							
Signal	Cortical area	S	G	D				
LFP	V1	63	58	56				
	V2	35	26	64				
MUA	V1	23	52	55				
	V2	35	26	63				

Table 4.1. Number of included channels in LFP and MUA analyses per cortical area and

#### Spectral analysis of sustained period

We performed spectral analyses of bLFP power, and bLFP-bLFP GC. For all those spectral analyses, we used a 500 ms stimulus period from 270 to 770 ms post stimulus onset. This stimulus period was chosen to focus the spectral analysis on the sustained period and avoid the early post-stimulus onset transients.

All spectral analyses used the Fourier transforms of the bLFP signals in the described periods. Each 500 ms period was cut into five overlapping 300 ms epochs (Welch's method), the epochs were linearly detrended, Hann tapered, zero-padded to 1 s, and Fourier transformed.

Power spectra were derived by squaring Fourier spectra. The power spectra of the visual stimulation period were baseline corrected. An average baseline power spectrum was estimated by combining all correct trials from all three repetition blocks over a pre-stimulus baseline window of 500 ms (-530 to -30 ms relative to stimulus onset). The stimulus-period power spectra were then expressed as percent change relative to the baseline power spectra.

To define frequency windows of interest for both V1 and V2, we first averaged the power spectra over all V1 and V2 sites and all correct trials of FIX. The average spectrum showed clear spectral peaks at 9, 20, 41, and 80 Hz (Suppl. Fig. 4.2). Correspondingly, we defined an alpha rhythm peaking at 9 Hz, a beta rhythm peaking at 20 Hz, and a gamma rhythm peaking at 41 Hz. We did not consider a second gamma rhythm, because it was at a harmonic frequency and much weaker than the main gamma peak. The range of each frequency band was defined as +/- 30% around these peak frequencies, resulting in an alpha band of 6-12 Hz, a beta band of 14-26 Hz, and a gamma band of 29-53 Hz as indicated in Suppl. Fig. 4.2.

GC spectra were derived through non-parametric spectral matrix factorization as described in (Dhamala et al., 2008) and implemented in FieldTrip (Oostenveld et al., 2011).

#### Peri-stimulus analysis of MUA

We estimated the average peri-stimulus MUA responses during FIX. For each repetition group separately (see Fig. 4.2A for definition of repetition groups), the MUA activity around the stimulus presentation was averaged over trials. The resulting traces were smoothed (25 ms boxcar moving average) and baseline normalized. A single baseline MUA value was obtained by averaging all MUA values over all baseline windows (0.53-0.03 s relative to stimulus onset) of all correct trials of all repetition blocks. This baseline MUA value was used to normalize the peristimulus MUA response by calculating the percent MUA change from the baseline to the stimulus period. The single baseline MUA value was approximately zero, because the MUA had been z-standardized using the mean and STD of the baseline periods (see above). Therefore, to avoid division by zero, the percent-change values were calculated as follows, expressing the MUA as percent change relative to a unit baseline:

$$MUAResponse(\%) = 100 \left( \frac{1 + \left( stim_t - \overline{baseline} \right)}{1 + \left( \overline{baseline} \right)} - 1 \right)$$

#### Single-trial estimates

To obtain single-trial estimates of MUA responses (stMUA), we defined a stimulus period (0.05 to 0.1 s relative to stimulus onset). Note that this stimulus period was meant to capture the strong transient MUA response and was different from the stimulus period for spectral analyses. The stMUA estimates were baseline normalized as described in section 'Peri-stimulus analysis of MUA'.

Single-trial estimates of power changes relative to baseline were obtained by averaging the power changes over the frequency windows of interest described above. Single-trial estimates for the gamma rhythm are referred to as stGamma. In some of the analyses, alpha and beta rhythms showed qualitatively the same effects (see Results, section 4.3) and therefore were combined into a common alpha-beta rhythm with a frequency band of 6 to 25 Hz (stAlpha-Beta). The single-trial power changes were baseline normalized as described in section 'Spectral analysis of sustained period'.

## Assessing the repetition effect as a function of orientation difference from the conditioned stimulus

For a given recording session, the conditioned orientation was randomly selected from a pool of 18 orientations. We aimed at investigating the effect of repeating this orientation 90 times during the FIX block on the response to all 18 orientations. Therefore, we compared the responses during VAR2, obtained after

the conditioning, to the responses during VAR1, obtained before conditioning. As VAR1 and VAR2 contained all 18 orientations, we could express the orientation presented in each trial as the orientation difference from that session's conditioned orientation (i.e. the orientation presented in FIX). Positive and negative orientation differences of the same magnitude were combined (because there was no reason to assume that they were different), leading to orientation differences from 0 to 90°. Note that in the VAR1 block, the monkey completed 10 mini-blocks, whereas in the VAR2 block, the monkey typically completed more mini-blocks. For this analysis, only the first ten mini-blocks of VAR2 were included to avoid potential biases due to different amounts of data

We intended to estimate the neuronal responses just before and just after the FIX block, separately for each orientation and thereby for each orientation difference relative to the conditioned orientation (see Fig. 46A for an illustration). Each orientation (difference) was presented once per mini-block, and thereby 10 times during VAR1 and 10 times during VAR2. These repetitions inside the VARX blocks themselves were expected to incur repetition-related changes in neuronal responses, which we aimed at eliminating. Therefore, we performed regression analyses of the neuronal responses as a function of these 10 repetitions, separately per orientation difference, and separately for the VAR1 block and the VAR2 block. From the VAR1 regression, we obtained the estimate of the neuronal response at the end of the VAR1 block, just before conditioning and refer to it as the preconditioning value; From the VAR2 regression, we obtained the estimate of the neuronal response at the beginning of the VAR2 block, just after conditioning and refer to it as the post-conditioning value. The difference between the post- and the pre-conditioning value isolates the effect of the conditioning during the FIX block, while eliminating or minimizing effects of stimulus repetitions inside the VARX blocks (which were required to obtain sufficient data for robust estimation and statistics).

## Assessing the repetition effect as a function of the orientation difference from the preferred orientation of the recording site

We also analyzed the repetition effect as a function of the difference between the stimulus orientation and the preferred orientation of the recording site. The approach for this analysis was identical to the approach described in the last paragraph, except that the orientation difference was not relative to the conditioned orientation but relative to the preferred orientation of the recording site. The preferred orientation was determined as described in Womelsdorf et al. (2012): Let  $r_m$  (m = 1; 2; ...; 18) be the empirically observed neuronal response when the m<sup>th</sup> stimulus orientation was presented, with the stimulus orientation denoted as  $\theta_m = (0, 10, 20, 30,..., 180^{\circ})$ . We intended to express neuronal responses as complex vectors and perform a complex vector average, to use the resultant vector orientation as the estimate of the preferred orientation. However, stimulus orientation is a circular variable in the interval [0, 180]. Therefore, to use this approach, we scaled the orientation variable to a circular variable in the interval [0, 360] and transformed it to radians. For every m, we defined

$$\tilde{\theta}_m = (2 \theta_m) (2\pi/360)$$

The vector sum was then defined as

$$S_i = \Sigma(w_m \cos(\tilde{\theta}_m rad)) + i \times \Sigma(w_m \sin(\tilde{\theta}_m rad))$$

where  $w_m$  is the mean gamma power value of the  $m^{th}$  stimulus orientation. Subsequently, the orientation of the vector sum Si was extracted based on the inverse tangent, and it was re-scaled from the  $[-\pi, +\pi]$  interval to the  $[0, +\pi]$  interval, and re-transformed from radiant to degree. Finally, the nearest stimulus orientation to the orientation of the vector sum was considered as the preferred orientation. This procedure was applied based on the responses measured during VAR1, separately per recording site.

#### Statistical analysis

All statistical analyses were based on non-parametric randomization tests.

We first describe the analyses for Figures 4.2-5, which are based on two types of tests: (1) We tested for significant differences between repetition groups 1 and 3, as defined in the results and Figure 4.2A; (2) We tested for significant slopes as a function of repetition number. Approach (2) takes all repetitions (except the early repetitions of FIX) into account, yet requires an estimation of the dependent variable for each single trial, which is difficult for GC. Therefore, we complemented it with approach (1), which defined trial groups that allow the straightforward estimation of GC; as this requires relatively many trials, we performed it only for the fixed-stimulus repetition block, containing 90 repetitions of the same stimulus.

Approach (1) compared spectra or time courses and therefore involved correction for multiple comparisons across frequencies or times, respectively. Per session and electrode or site (pair), we calculated differences between repetition groups 1 and 3 and subsequently averaged those differences over electrode or site (pairs)

and sessions. We then performed 1000 randomizations. In each randomization, per session and electrode or site (pair), we randomly exchanged trials between groups 1 and 3 and re-calculated the difference. We then averaged over electrodes, sites or site pairs. We then retained the minimal difference and placed it into the distribution of minimal randomization differences, and we retained the maximal difference and placed it into the distribution of maximal randomization differences. The 2.5th percentile of the minimal randomization distribution and the 97.5th percentile of the maximal randomization distribution were used as thresholds for statistical significance, corresponding to a two-sided false-positive rate of 5%, corrected for multiple comparisons.

This approach allowed us to test for effects over time in the MUA, and over frequency in the case of power and GC spectra. In the case of GC spectra, we complemented our analysis with an additional statistical assessment (see motivation in Results, section 4.3) that looked for significant changes in three specific frequency bands: alpha (6-12 Hz), beta (14-26 Hz) and gamma (29-53 Hz) (see section 'spectral analysis of sustained period' above for the definition of these frequency bands). This approach compared the GC for three frequency bands and two directions, and therefore involved correction for six multiple comparisons. Per session and site pair, we calculated differences in GC between repetition groups 1 and 3 and subsequently averaged those differences over the frequencies within each frequency bands, separately per band, and subsequently over site pairs and sessions. This delivered one observed difference per frequency band and GC direction. We then performed 1000 randomizations. In each randomization, per session and site pair, we randomly exchanged trials between groups 1 and 3, re-calculated the difference and the averaging as for the observed differences, and kept the maximal and minimal differences separately per frequency band and GC direction. This resulted in one maximal randomization and one minimal randomization distribution per frequency band and per GC direction. Note that this approach was motivated by the large differences in GC values and GC differences between frequency bands, as discussed in the Results section. From each randomization distribution, we used the 2.5/6 percentile and the 100-(2.5/6) percentile as thresholds for statistical significance of the corresponding observed difference. Thus, the correction for multiple comparisons across the six combinations of frequency bands and GC direction used the Bonferroni method. This constitutes a non-parametric significance test with a two-sided false-positive rate of 5%, corrected for multiple comparisons across frequency bands and GC directions.

Approach (2) tested the slopes for single-trial values of MUA in a specific time window or spectral power in specific bands and therefore did not involve correction for multiple comparisons across frequencies or times. First, the data were averaged over sites, and subsequently a linear regression was performed to obtain the slopes for the observed data. For the VARX blocks, this gave separate slopes per session and per stimulus orientation, which were then averaged; for the fixed-stimulus block, this gave separate slopes per session, which were then averaged. Then, we performed 1000 randomizations. In each randomization, the repetition order was randomized, and subsequently, the same analyses were performed as for the observed data. The resulting slopes were placed into the randomization distribution. The 2.5<sup>th</sup> and 97.5<sup>th</sup> percentiles of this distribution were then used as thresholds for statistical significance with a two-sided false-positive rate of 5%. Note that some slope analyses were performed for specific repetition ranges, e.g. for the first 20 trials, which is then specified in the results and figure legends.

For Figure 4.6, we used the difference between the above described post-conditioning value and the pre-conditioning value. Note that the randomization between VAR1 and VAR2 was performed without keeping the order within the respective blocks. This automatically eliminated the repetition effects expected to occur within the VARX blocks. Thereby, we could use, for the randomized data, the same test statistic as for the observed data, namely the difference between the neuronal response at the beginning of VAR2 minus the neuronal response at the end of VAR1.

For Figure 4.7, we tested for significant differences in the mean neuronal responses between the three blocks (VAR1, FIX, and VAR2). We compared the results of the regression analyses of their single-trial estimates in the following way. First, the mean values of the fitted regression lines were computed for each block individually and subtracted from each other in order to obtain the observed mean difference between blocks. Then, we performed 1000 randomizations by shuffling single-trial estimates between blocks and repeating the analysis. This resulted in a distribution of mean differences, and its 2.5<sup>th</sup> and 97.5% percentiles were used to as thresholds for statistical significance, as described above.

#### Sample size

This study involved one male macaque monkey (*Macaca mulatta*). The use of a single subject allows an inference on that sample, but not on the population. If a second macaque had been added, any useful inference would still have pertained to that sample of two macaques, but not to the population of macaques, as Fries

and Maris (2022) have shown previously. As the inference remains qualitatively the same, we opted for a single macaque to reduce the number of animals used in research, according to the 3R principles (Russell and Burch, 1959). This approach has been questioned, and we responded to this, as described in Chapter 3.

#### Results

Laminar recordings of multi-unit activity (MUA) and local field potentials (LFPs) were obtained from primary visual cortex, V1, and in a subset of sessions from secondary visual cortex, V2, in one awake macaque monkey (Fig. 4.1D). The monkey performed a fixation task, while large grating stimuli were presented on a screen. In each trial, one grating orientation was shown (Fig. 4.1A). In each session, the monkey completed the following trial blocks (Fig. 4.1B-C): (1) A first block of stimulus repetitions with variable stimuli, referred to as the "VAR1" block; (2) A short break; (3) A block of stimulus repetitions with a fixed stimulus, referred to as "FIX" block; (4) A second block of stimulus repetitions with variable stimuli, referred to as the "VAR2" block. Stimuli were stationary square-wave gratings of 18 different, evenly spaced orientations (see Methods for details). VAR1 contained 10 subblocks, with each sub-block containing one correctly performed trial for each of the 18 different orientations. VAR2 had the same structure as VAR1, and contained at least 10 sub-blocks, but then continued as long as the monkey kept working. FIX contained 90 correctly performed trials for one of the orientations, which was randomly selected from the 18 orientations for a given recording session; this orientation will be referred to as the "conditioned" orientation.

As shown in Figure 4.1D-E, the recording chamber allowed perpendicular access in V1 and the underlying V2. Using linear multi-contact probes, we were able to simultaneously record across depths in both areas, yet not always across all depths in both areas simultaneously. Figure 4.1E shows the receptive fields (RFs) of an example recording session. Within each area, the RF centers were aligned across depths, confirming that the recordings were mainly confined within the same cortical column. An abrupt shift of the RF centers, accompanied by an increase of the RF size indicated the transition from area V1 to V2 (Fig. 4.1E-4.1F; see also Suppl. Fig. 4.1D). Figure 4.1G and Suppl. Figure 4.1B provide a summary of the MUAand bLFP-RF centers of the recorded sessions. The laminar recordings enabled the investigation of the previously described repetition-related changes, now as a function of cortical layers.

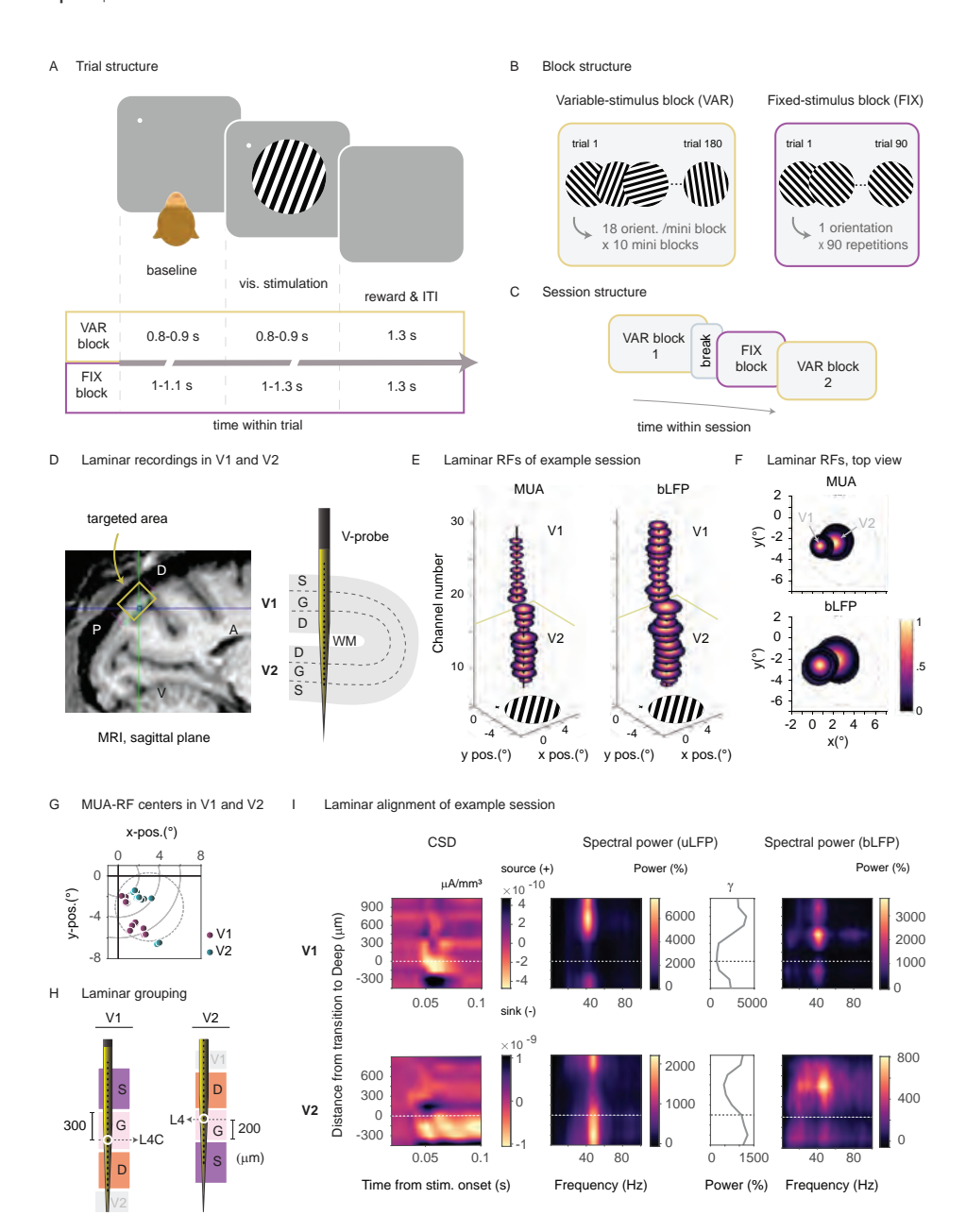


Figure 4.1. Behavioral task and electrophysiological recordings. (A) Schematic representation of the general trial structure and the specific timings for the VAR and the FIX blocks. (B) Structure of the variable-stimulus, VAR, blocks, and the fixed-stimulus, FIX, block. VAR blocks consisted of several mini-blocks. Within each mini-block, gratings of 18 different orientations were pseudo-randomly interleaved. In FIX, a stimulus orientation randomly selected for a given session was presented across 90 consecutive trials. (C) Structure of the session, showing the sequence of blocks. Each session started with VAR1, which was followed by a short break and then by FIX. FIX was immediately followed by VAR2. (D) Left: Sagittal plane of MRI scan of Monkey G showing the target area for electrophysiological recordings, marked by a yellow rectangle. The anterior (A) - posterior (P) and dorsal (D) - ventral (V) orientations are indicated. Right: Illustration of the targeted cortical area in V1 and V2 and their respective laminar compartments (S: superficial, G: granular, D: deep). Laminar recordings were performed with multi-contact linear arrays (V-probe). (E) MUA- and bLFP-Receptive Fields (RFs) in V1 and V2 of an example recording session as a function of channel number. The fixation spot (black cross) and the grating are shown on the bottom of the plots for comparison. (F) Top view of the RFs from (E). (G) MUA-RF centers per session, averaged over all contacts within one area, separately for V1 (magenta, N=16 sessions) and V2 (green, N=16 sessions). The grey dotted line indicates the outline of the presented grating. (H) Illustration of the grouping of V1 and V2 recording sites into laminar compartments. (I) Neuronal responses to grating presentations in one example session each for V1 and V2. Shown from left to right: Current Source Density (CSD), percent unipolar-LFP (uLFP) power change, percent uLFP-power change averaged over a gamma band frequency window (29 -53 Hz) and percent bipolar-LFP (bLFP) power change relative to baseline. White dashed lines denote the transition to deep layers (0 µm).

The VAR1 block allowed us to investigate whether the repetition-related changes occur during the interleaved presentation of 18, i.e. many, different orientations, with a given orientation repeated only across sub-blocks, i.e. typically spaced by several (on average 17) intervening stimuli. This block also provided orientation tuning curves. The FIX block induced repetition-related plasticity for the conditioned orientation. The VAR2 block provided orientation tuning curves after the repetition of the conditioned orientation in the FIX block. The comparison of VAR2 with VAR1 allowed us to investigate whether changes induced by the repetition of the conditioned orientation during FIX affect neuronal responses induced by other orientations, and therefore, test how orientation-specific these changes are. Note that the conditioned orientation in the FIX block was randomly selected on each recording day. This dissociated the conditioned orientation from the preferred orientation of the recorded neuronal populations.

We set out to investigate stimulus-repetition effects as a function of cortical depth. To this end, we assigned for each session the recording electrodes to three laminar compartments: superficial, granular, and deep. We first computed the current source density (CSD) of the visually evoked LFP (Fig. 4.11). Based on the CSD maps, we identified the input layers of areas V1 and V2. This allowed us to estimate the distance of each recording site from the input layer. This relative distance was then used to assign each recording site to one of the three laminar compartments (see Methods for a detailed description). Figure 4.1I shows the CSD and spectral power as a function of cortical depth of example V1 and V2 sessions.

The presentation of the grating induced a clear MUA response in all laminar compartments of both areas (Fig. 4.2D-E). The visual stimulation also induced a clear narrow-band gamma peak during the period of sustained stimulation (0.27-0.77 ms relative to stimulus onset) in all compartments of V1 and V2 (Fig. 4.3D-E). Additional spectral peaks were evident in both areas. In all V1 layers, there was a clear alpha peak centered around 8-10 Hz. An additional beta peak was present at 18 Hz in superficial and deep layers. In V2, there was a large peak in the beta range (20-23 Hz) and a smaller alpha peak (9 Hz) that was mostly evident in superficial and deep layers.

# The repetition of a fixed-orientation grating stimulus leads to gamma-power increases and spike-rate decreases across layers

We first investigated the repetition-related effects of a fixed-orientation grating stimulus (FIX block) on the amplitude of gamma-band power and the spike rates (MUA). To this end, we employed two complementary approaches. First, we obtained single-trial estimates that allowed us to look for neuronal changes over the course of stimulus repetitions. Single-trial estimates were obtained by averaging neuronal responses of a given trial over a time window (in the case of MUA) or over a frequency band of interest (in the cases of spectral power; see Methods for a detailed description). We refer to single-trial estimates of MUA responses relative to baseline as stMUA, and correspondingly for LFP power in the gamma-frequency range as stGamma (see Methods for details).

To localize repetition effects in time (for MUA) or frequency (for power or GC), we also directly compared time courses or spectra, respectively, between an early and a late group of trials in the FIX block. Of the 90 trials of the FIX block, the initial 6 were excluded, and the remaining 84 were divided into three non-overlapping groups of 28 trials (Fig. 4.2A and Fig. 4.3A). We compared the first and third of those 28-trial groups to assess the repetition effect. The exclusion of the initial 6 trials was motivated by the previous finding that gamma-band power often shows a distinct behavior in response to the first few repetitions of a given stimulus, with likely a different mechanism compared to the later repetition-related increase (Peter et al. (2021); Stauch et al. (2021); see Discussion in section 4.4).

Figure 4.2B and C illustrate the mean MUA responses for all V1 and V2 recording sites and for each trial group. Comparing trial group 3 versus group 1, MUA did

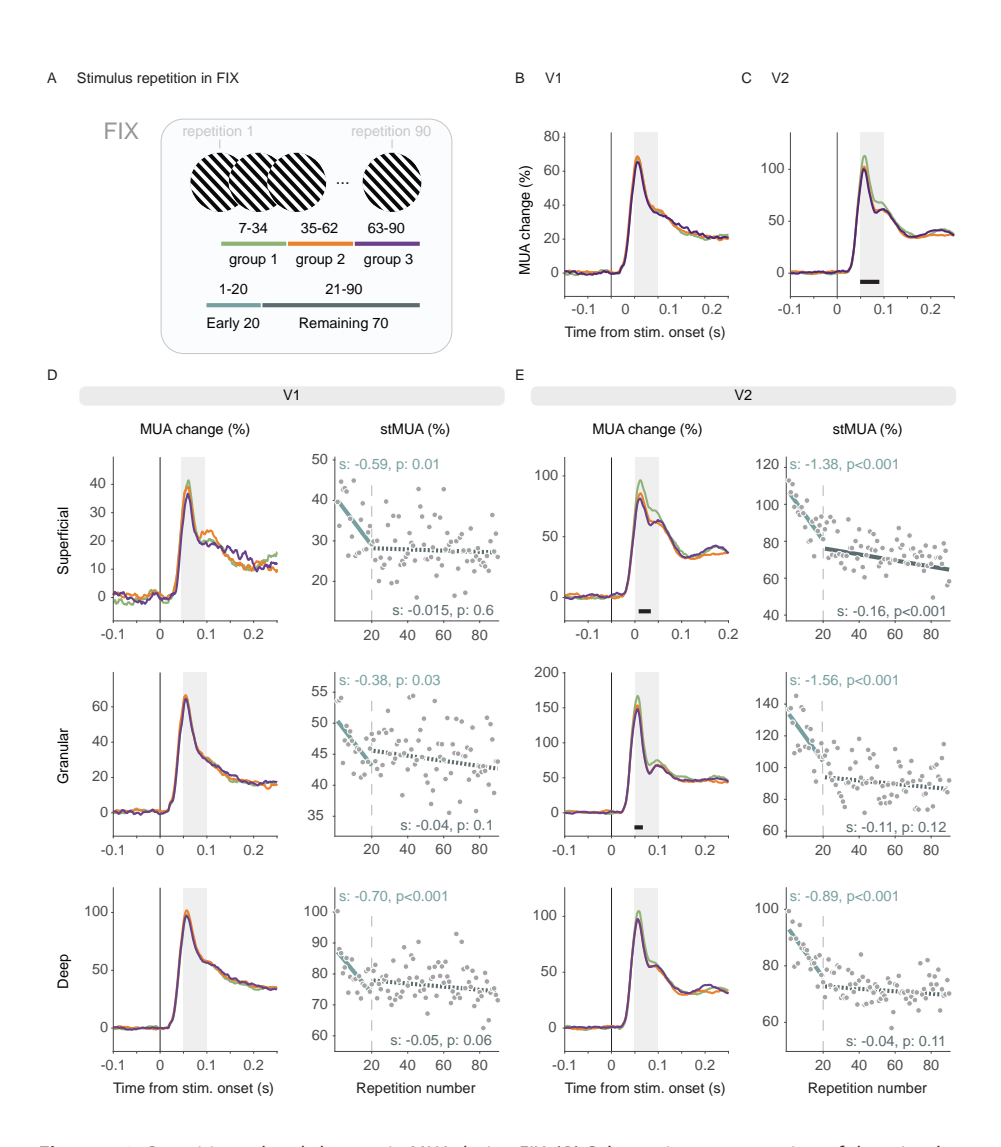


Figure 4.2. Repetition-related changes in MUA during FIX. (A) Schematic representation of the stimulus repetitions in FIX and their grouping into repetition groups 1, 2 and 3. Each group consisted of 28 repetitions. For the analysis of stMUA in D and E, we also defined an Early-20 and a Remaining-70 trials group. (B-C) MUA response from baseline averaged over all sites in V1 (B) or V2 (C), per repetition group (color-coded as in A). (D) Left: MUA response from baseline per repetition group averaged per laminar compartment (from top to bottom: superficial, granular, and deep). Grey rectangles indicate the time period that was used to estimate the stMUA responses. Right: stMUA as a function of repetition number within FIX. The dashed grey vertical lines indicate the 20th repetition. Two separate regression fits are plotted: one for the Early-20 repetition group and one for the Remaining-70 repetition group. Regressions with (non-) significant slopes are plotted as (dashed) solid lines. The respective slopes (s) and p-values (p) are reported on top of each panel. (E) Same as in D but for V2.

not show significant differences in area V1 (Fig. 4.2B, D), whereas there were some significant differences during the early transient in area V2, both for the MUA pooled over all compartments (Fig. 4.2C) and for the superficial and granular compartments (Fig. 4.2E).

To further investigate how the MUA decrements found for the transient evolve across trials, stMUA estimates were obtained by averaging MUA responses from each trial within a time window of 0.05 to 0.1s relative to stimulus onset. Visual inspection of stMUA in both areas V1 and V2 revealed two distinct patterns: (1) a sharp decline during the initial approximately 20 trials, followed by (2) a period of more subtle changes throughout the subsequent 70 trials. To capture both patterns, we applied two separate linear regression models: one for the first 20 stMUA responses (referred to as "Early-20") and one for the stMUA responses from trials 21-90 (referred to as "Remaining-70"), as illustrated in Figure 4.2A. The regression slopes were significantly negative for all V1 and V2 laminar compartments during the Early-20 trials, and for the superficial compartments of V2 during the Remaining-70 trials (Fig. 4.2D-E). When we considered the stMUA pooled over all V1 and V2 sites, the regression slopes were significantly negative for both the Early-20 and the Remaining-70 trials and for both areas (Suppl. Fig. 4.3).

We then tested the repetition-related effects on LFP power. In accordance with previous studies (Brunet et al., 2014; Peter et al., 2021; Stauch et al., 2021), we observed a significant increase in gamma-band power from group 1 to group 3 in both areas V1 and V2 (Fig. 4.3B-C). This increase was not only evident in the grand averages of V1 and V2 but also within each laminar compartment (Fig. 4.3D-E).

Given that the repetition-related increase was confined to the gamma band (34-51 Hz for V1 and 40-54 Hz for V2; Fig. 4.3B-C), our subsequent single-trial analysis was focused on this frequency range. Note that we defined the different frequency bands independently of the repetition effect, on the basis of the stimulus-versus-baseline power change spectra (see Methods and Suppl. Fig. 4.2 for details and resulting band definitions). The resulting frequency band for gamma was 29-53 Hz. For this gamma band, stGamma was computed, and the stGamma values of trials 7 to 90 were fitted with a linear regression. The regression slopes were significantly positive for all laminar compartments of V1 (Fig. 4.3D) and V2 (Fig. 4.3E) and when all compartments were pooled per area (Suppl. Fig. 4.3). The first six trials were excluded from the regression fits for reasons mentioned earlier.

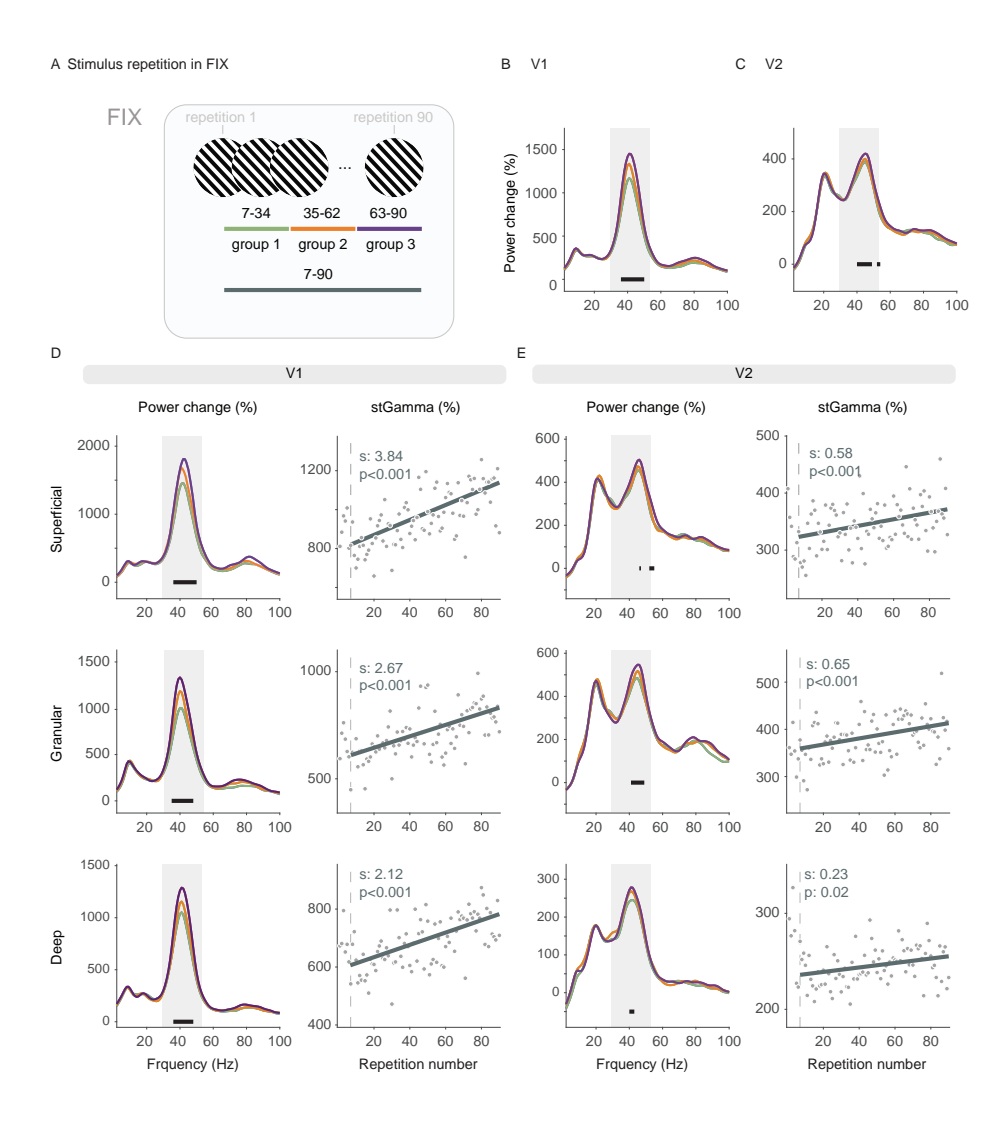


Figure 4.3. Repetition-related changes in bLFP power during FIX. (A) Schematic representation of the stimulus repetitions in FIX and their grouping into repetition groups 1, 2 and 3. Each group consisted of 28 repetitions. For the analysis of stGamma in D and E, we also defined a Trial-7-90 group. (B-C) Power change from baseline averaged over all V1 (B) and V2 sites (C), per repetition group (color-coded as in A). (D) Left: Power change from baseline per repetition group per laminar compartment (from top to bottom: superficial, granular, and deep). Grey rectangles indicate the gamma frequency range that was used to estimate the stGamma responses. Right: stGamma as a function of repetition number within FIX. The dashed grey vertical lines indicate the 7th repetition. Regressions with (non-)significant slopes are plotted as (dashed) solid lines. The respective slopes (s) and p-values (p) are reported on top of each panel. (E) Same as in D but for V2.

#### Repetition-related changes in inter-laminar interactions

We then investigated the effects of stimulus repetition on the information flow between laminar compartments inside V1 and inside V2. Information flow was quantified by computing Granger causality (GC) between all possible intra-areal inter-laminar site pairs and subsequent averaging for each combination of laminar compartments, separately for each direction of information flow. To test for repetition-related GC changes, we used the FIX block and compared trial group 1 to group 3. Similar to our analysis of power spectra, we first compared GC spectra per frequency. However, we noted that the randomization distributions were dominated by GC values in the lower frequency range. Therefore, we additionally present a less fine grained comparison, after first averaging GC values within the distinct frequency bands as defined in the Methods and shown in Suppl. Figure 4.2. The results of both statistical approaches are reported in Figure 4.4, and the results for the separate bands are discussed here. In area V1, in the alpha-frequency range, there was an increase in GC with stimulus repetition from deep to superficial, deep to granular, superficial to deep and superficial to granular compartments. In the beta range, we observed a significant increase from granular to superficial and superficial to deep compartments. In gamma, there was a significant increase from granular to superficial, from deep to superficial and deep to granular layers. In area V2, the effects were mostly confined to the gamma-frequency band, with an increase from deep to superficial compartments.

Suppl. Figure 4.4 shows a corresponding analysis for inter-areal GC between laminar compartments of V1 and V2. Note that the bLFP-RFs of the simultaneously recorded V1- and V2-sites typically overlapped only to a small degree or not at all, and therefore (1) gamma-band interactions were expected to be weak or absent, (2) the observed effects might be specific for interactions between V1 and V2 sites with non-overlapping RFs. Indeed, a clear gamma peak was mainly observed for GC from the deep V1 to the deep V2 compartment, maybe because deep-layer RFs are larger (Gilbert, 1977; Self et al., 2013). Overall, feedforward GC from V1 to V2 often showed a clear alpha peak, whereas feedback GC from V2 to V1 often showed a clear beta peak. The repetition effects showed clear patterns that differed between alpha and beta. For alpha, all significant repetition effects were increases. By contrast, for beta, all significant repetition effects were decreases, and they all involved the granular or deep V1 compartments.

## The repetition of multiple interleaved stimuli leads to MUA and gamma-band changes

So far, we demonstrated that the repetition of a single orientation leads to plastic changes of neuronal activity across laminar compartments of V1 and V2. We next asked whether these effects were also present when many different stimuli were presented interleaved (Fig. 4.5A). As the above analyses found qualitatively similar repetition-related results across the laminar compartments and in both areas, all following analyses will pool the laminar compartments per area, and we add for most analyses the results for the pooled areas, referred to as V1+V2. We did this to simplify the presentation and enhance sensitivity.

We first investigated repetition-related plastic changes in VAR1. In this block, eighteen grating orientations were repeated interleaved. Importantly, it was the first block that the monkey completed in each session (Fig. 4.5B). This ensured that any observed repetition-related neuronal changes (within the session) could only result from repetitions within this block, excluding the influence from the FIX block. VAR1 consisted of ten mini-blocks. In each mini-block, all eighteen orientations were presented once in a randomized order. This design prevented immediate repetitions of the same orientation within a mini-block, while allowing each orientation to be repeated across the ten mini-blocks (Fig. 4.5A).

StMUA and stGamma responses were calculated per orientation and mini-block, resulting in ten single-trial estimates per orientation. For each orientation, the ten estimates were first fitted with a linear regression model. All estimates and fits were then averaged, leading to a grand-average fit.

Interestingly, stMUA and stGamma of V1, V2, and V1+V2 showed qualitatively similar repetition effects as observed in the FIX block. The slope of stMUA was significantly negative (green data in Fig. 4.5C-E), indicating a decrease in spiking activity with stimulus repetition. Conversely, the slope of the stGamma was significantly positive (green data in Fig. 4.5F-H), indicating an increase with repetition.

Thus, changes in MUA and gamma as observed with many repetitions of a single orientation in FIX, were also seen during VAR1 with 18 different orientations interleaved. Note, however, that the experimental design of VAR1 did not allow us to dissociate between the repetition of a specific orientation versus the overall repetition of stimuli across mini-blocks. Previous results suggest that when different orientations are presented in separate adjacent blocks, there is some overall gamma increase across the session, yet the dominant effect is a repetition-

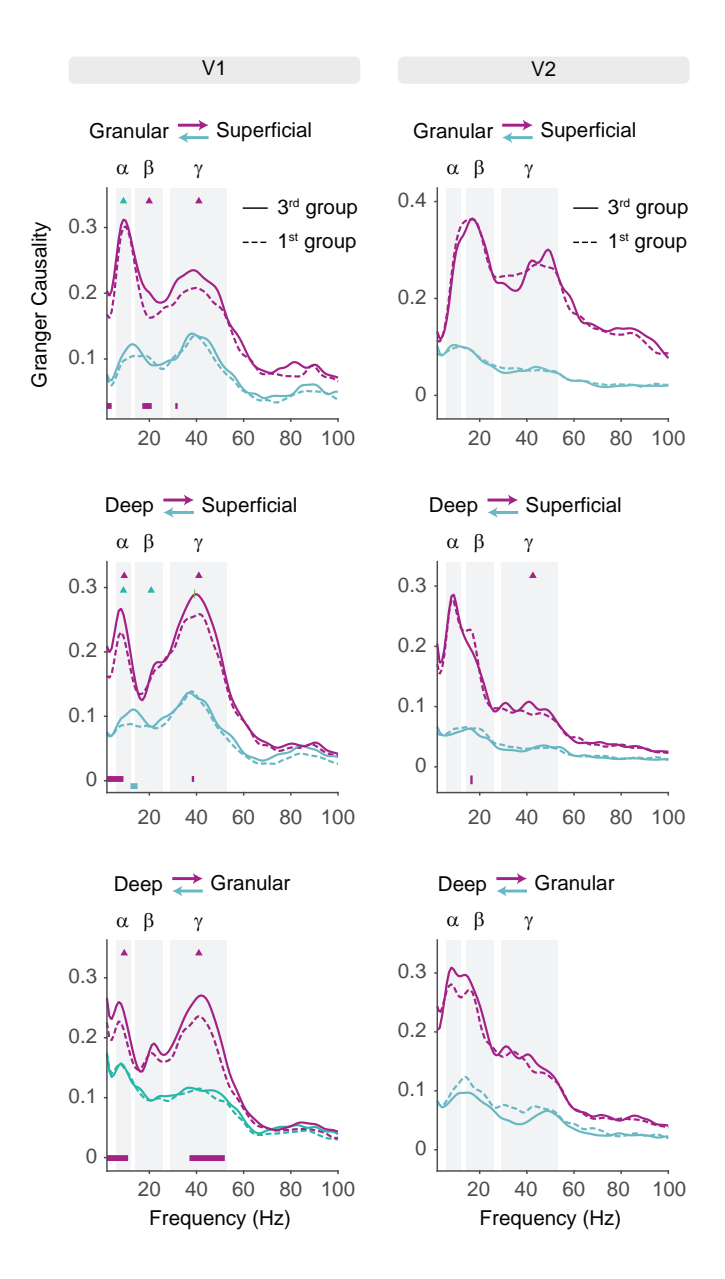


**Figure 4.4.** Repetition-related changes of Granger Causality between laminar compartments during FIX. Granger Causality (GC) during the 1st (dashed line) and 3rd repetition group (solid line) of FIX. Different colors represent the GC direction as indicated on top of each panel. Grey rectangles show the three frequency bands that were used for the statistical analysis: alpha ( $\alpha$ ), beta ( $\beta$ ), and gamma ( $\gamma$ ). Triangles indicate statistically significant changes per frequency band, color-coded per GC direction; all significant changes were increases. Horizontal lines at the bottom of the plots (color-coded per directionality) indicate frequencies with significant differences derived from the statistical comparison across all frequencies.

related stimulus-specific gamma increase (Stauch et al., 2021). In the following, we will use VAR2 to investigate whether such stimulus-specificity is also present for 18 interleaved orientations.

## The repetition of multiple interleaved stimuli leads to stimulusspecific neuronal changes

VAR2 had the same structure as VAR1, but it was completed immediately after FIX. This allowed us to investigate lasting effects of the orientation that had been conditioned during FIX. We looked for plastic changes in VAR2 separately for the conditioned orientation and for all other orientations combined, referred to as non-conditioned orientations. We hypothesized that different repetition-related response patterns between these two groups could indicate stimulus specificity.

Note that this analysis led to unequal numbers of trials per group. For the conditioned orientation, single-trial estimates were based on only one trial per mini-block. For the non-conditioned orientations, they were based on 17 trials. This probably led to higher noise levels in the estimates for the conditioned orientation.

In V1, V2 and V1+V2, the stMUA slopes for the non-conditioned orientations were significantly negative, whereas the stMUA slopes of the conditioned orientation did not show a significant effect (Fig. 4.5C-E). Direct comparison of the regression lines for the conditioned versus non-conditioned orientations revealed that the slopes were significantly different for V1 but not for V2 or V1+V2. Yet intercepts were significantly lower for the conditioned orientation for V1, V2 and V1+V2. The exact p-values for each comparison are reported in the legend of Figure 4.5.

stGamma responses for the non-conditioned orientations showed the expected positive slope for V1, V2 and V1+V2 (Fig. 4.5F-H). By contrast and intriguingly, stGamma responses for the conditioned orientation showed a negative slope for V2 and V1+V2, and the same trend for V1 (p=0.07). Direct comparison of the regression lines for the conditioned versus non-conditioned orientations revealed that, for V1, V2 and V1+V2, the conditioned orientation showed higher intercepts and lower slopes.

Thus, stGamma responses to the conditioned versus the non-conditioned orientation differed both at the beginning and during the first ten mini-blocks of VAR2. This demonstrates that repetition-related effects did not only survive the interleaving of 18 different orientations, but that they were at the same time stimulus specific. Furthermore, there was partial persistence over time. The difference between stGamma for conditioned versus non-conditioned orientations decreased over the course of the ten mini-blocks, such that by the 10<sup>th</sup> mini-block, the two orientation groups elicited responses of similar amplitude (Fig. 4.5F-H). This implies a partial persistence of the gamma-band increase induced during FIX despite the interleaved repetition of 17 other stimuli during VAR2. Taking into account the trial duration of VAR2, the time period to complete all ten mini-blocks ranges between at least 8.7 and 9.3 minutes, without considering additional delays due to incorrect trials like fixation beaks.

As a control, we also compared the single-trial responses to the conditioned and non-conditioned orientations in VAR1. As expected, before conditioning, the response patterns of stMUA and stGamma did not differ between orientation groups (Suppl. Fig. 4.5).

#### Gamma-band plasticity is highly stimulus-specific

We next quantified the degree of stimulus specificity of the repetition-related changes induced by the FIX block. Do these repetition effects transfer to orientations that are close to the conditioned one? By comparing the neuronal responses in VAR2, that is after FIX, to the responses in VAR1, that is before FIX, we were able to investigate the effects of conditioning one orientation on the neuronal responses for all orientations, including the conditioned orientation itself, immediately neighboring orientations and more dissimilar orientations.

On each recording day, the conditioned orientation was chosen randomly, leading to different conditioned orientations across sessions. To combine data across sessions, we expressed all orientations as a function of their orientation difference from the conditioned orientation. As we had no reason to believe that positive and negative orientation differences had different effects, we pooled corresponding absolute orientation differences, leading to orientation differences ranging between 0 and 90 °.

As we showed earlier, there are plastic changes that take place during VARX blocks due to repetitions across mini-blocks. We aimed at isolating the effect of the conditioning happening in FIX while eliminating the influence of VARX effects. To this end, we estimated the responses at the end of VAR1 and at the start of VAR2, each time using all data of the respective blocks, but eliminating the changes that occurred within those blocks. Specifically, for each orientation, we fitted linear regressions to VAR1 responses and used the value of this regression at the final VAR1 stimulus presentation as the best estimate of the last response just before FIX,

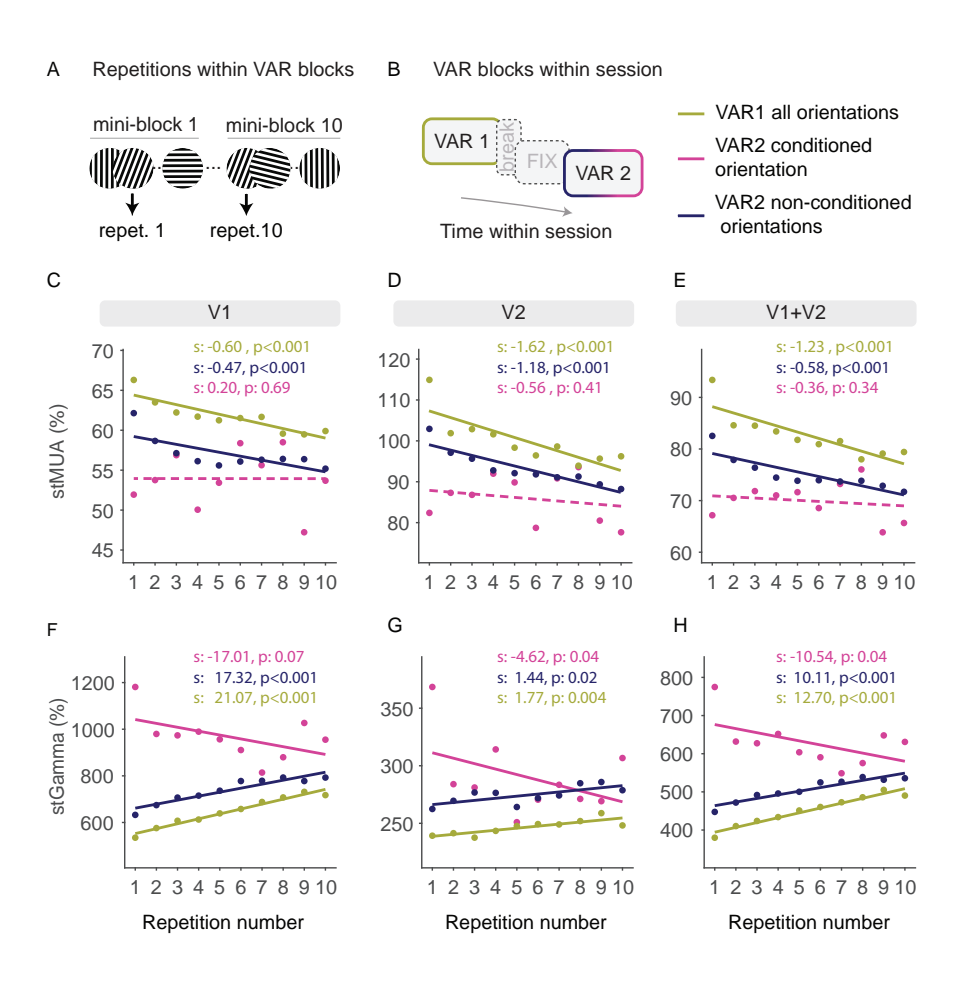


Figure 4.5. Repetition-related changes during VAR blocks in V1 and V2. (A) Schematic representation of stimulus repetitions across mini-blocks in VARX, illustrating that a given orientation occurred at a random position per mini-block. (B) Block sequence within a recording session. (C - E) stMUA as a function of the repetition number of a given stimulus orientation across the mini-blocks. For VAR1, neuronal responses were averaged over all orientations. For VAR2, neuronal responses were divided into two groups: responses for non-conditioned orientations and responses for the conditioned orientation. Each group is color-coded and presented for V1 (C), V2 (D) and combined V1+V2 (E). Lines indicate the respective linear fits (solid (dashed) for (non-)significant slopes). Slopes (s) and p-values (p) are color-coded and reported at the top of each panel. (F - H) Same as C-E, but for stGamma.

Results of the statistical comparisons of repetition-related stMUA changes between conditioned and non-conditioned orientations in VAR2 (listed are the p-values): (1) difference between slopes: V1: 0.06, V2: 0.42, V1+V2: 0.19; (2) difference between intercepts: V1 < 0.001, V2 < 0.001, V1+V2 < 0.001. Results of the statistical comparisons of repetition-related stGamma changes between conditioned and nonconditioned orientations in VAR2 (listed are the p-values): (1) difference between slopes: V1: 0.004, V2 <0.001, V1+V2: 0.006; (2) difference between intercepts: V1 <0.001, V2 <0.001, V1+V2 <0.001.

referred to as Pre-conditioning value, or just "Pre" in Figure 4.6. Correspondingly, we fitted linear regressions to VAR2 and used the intercept of this regression, i.e. its value for a hypothetical zeroth presentation before any effect of the first VAR2 mini-block, referred to as Post-conditioning value or just "Post" in Figure 4.6. Then, we computed the difference of Post minus Pre as an estimate of the effects induced by the intervening FIX.

The conditioning-induced stMUA changes were qualitatively similar in V1 and V2 (Fig. 4.6B). There were both increases and decreases, most not reaching significance, with the changes almost balanced around zero. Yet, there also seemed to be a tendency for an overall increase with orientation distance from the conditioned orientation; indeed for some of the orientations opposite to the conditioned orientation, increases reached significance. For the pooled V1+V2 data, a decrease close to the conditioned orientation reached significance.

The conditioning-induced stGamma changes were again qualitatively similar in V1 and V2 (Fig. 4.6C), but dissimilar from the stMUA changes. For gamma, there was a significant increase at the conditioned orientation, for V1, V2 and V1+V2, and no significant changes for all but one of the other conditions. Overall, the pattern was consistent with an increase that is specific for precisely the conditioned orientation.

Note that VAR1 and VAR2 were separated by substantial time, for the break between VAR1 and FIX, and for FIX itself. With this passage of time, we expected some decay of the VAR1-induced changes between Pre and Post (except of course for the conditioned orientation; Peter et al. (2021)). Given that VAR1 induced MUA decreases and gamma increases, the decay of these effects should lead to opposite effects on the Post-minus-Pre difference (i.e. our estimate of the conditioning during FIX): The MUA effects should be slightly shifted upwards, whereas the gamma effects should be slightly shifted downwards. Indeed, for MUA, most significant effects were increases, and for gamma in V1, there was one unexpected significant decrease.

As a control, we repeated the same analyses, yet not aligned to the conditioned orientation but to the preferred orientation of the respective recording site. As mentioned above, the conditioned orientation was randomly chosen per session to eliminate confounds with the preferred orientation. The analyses aligned to the preferred orientation revealed no significant changes for stMUA, except for a single orientation after combining V1 and V2 (Suppl. Fig. 4.6B). For stGamma, there were no significant changes, except for one orientation in V1 and V1+V2 (Suppl. Fig.

4.6C). These unexpected significant results are an increase for stMUA and a decrease for stGamma. Thereby, they are consistent with the abovementioned decay for the non-conditioned orientations due to time passing during FIX. Overall, these control analyses suggest that the experimental design was successful at avoiding a confound between the conditioned and the preferred orientation.

#### A Analysis of stimulus specificity of the conditioning effects

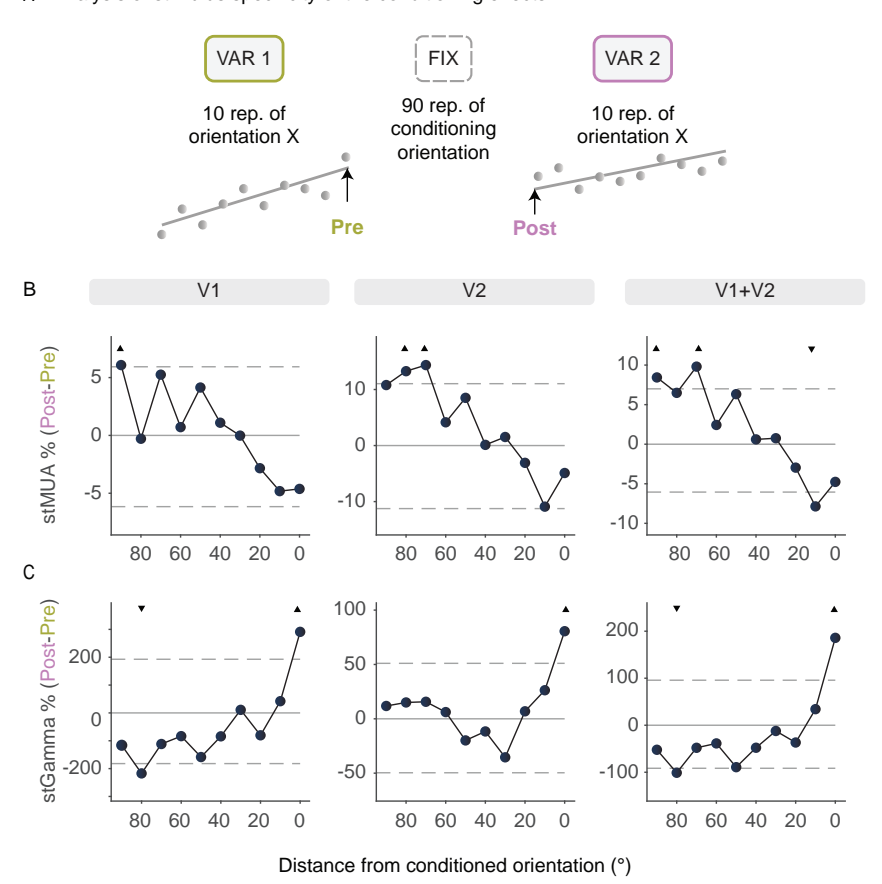


Figure 4.6. Stimulus specificity of the repetition-related changes. (A) Schematic representation of the analysis of stimulus specificity. For each orientation, single-trial estimates of the neuronal responses were fitted with linear regressions in VAR1 (pre conditioning) and VAR2 (post conditioning). The conditioning-related change of the neuronal responses was then calculated as the difference between the intercept of the VAR2 fit (marked as "Post") minus the last point of the VAR1 fit (marked as "Pre"). The conditioning-related change (Post-Pre) for stMUA (B) and stGamma (C) are plotted as a function of orientation difference from the conditioned orientation. Positive and negative orientation differences have been combined. Dashed horizontal lines indicate the upper and lower significance limits derived from the randomization distribution. Triangles indicate orientation differences with statistically significant conditioning effects, with the triangles pointing upward for increases and downward for decreases.

### Neuronal responses across trial blocks suggest effects of temporal stimulus predictability

When we compared the spectral response to the conditioned orientation during FIX and VAR2, we found that the strength of the alpha and beta rhythms was conspicuously higher during FIX than VAR2 in both areas and all laminar compartments (Fig. 4.7B and Suppl. Fig. 4.7). When we investigated singletrial responses across all trials, including all orientations, of a session, we noticed intriguing dynamics across trial blocks (Fig. 4.7C-E). This was particularly conspicuous for alpha and beta power, and since these two frequency bands showed similar effects here, we pooled them in a combined alpha-beta band (6-26 Hz) for the remaining analyses and refer to these single-trial estimates as stAlpha-Beta. In area V1, stAlpha-Beta showed in each block, for approximately the first 20 trials, a strong increase, and for the remaining trials of the block it either stayed at this high level or decreased slightly (Fig. 4.7C, see Suppl. Fig. 4.8 for similar results in area V2). Note that for this and the following analyses, to show the stability of the effects, we included all trials that the monkey completed in VAR2 up to the minimal number available in all sessions. For FIX, alpha-beta power rose to and staved at a substantially higher level than for VAR1 or VAR2. Table 4.2 reports the p-values of the statistical comparisons between the means of the regressions of each block. Note that in FIX, the conditioned orientation was repeated in each trial, rendering it highly predictable, whereas in VARX, the 18 different orientations were randomly interleaved, rendering a given orientation much less predictable. Studying this orientation predictability was not the purpose of our experimental design, such that the design was not optimized to study predictability effects, but nevertheless, the results seemed intriguing and potentially inspiring for more targeted future investigations.

stMUA showed in all blocks, for approximately the first 20 trials, a strong decrease; this reached significance in all blocks, except in VAR1 for V1, which showed the same trend (Fig. 4.7D). For the remaining trials of each block, stMUA showed further decreases. For FIX, stMUA decreased to and stayed at lower levels than for VAR1 or VAR2 (Table 4.2). This is again suggestive of an effect of stimulus predictability.

As mentioned above, previous studies had described that also stGamma can show decreases for the initial few repetitions of a given stimulus. The reports so far have described this decrease to occur across the initial 4 (Peter et al., 2021) or initial 10 (Stauch et al., 2021) trials, and primarily for stimuli that were less overtrained than the gratings for the monkey used here. Nevertheless, to be consistent with the analyses of stApha-Beta and stMUA, we also analyzed stGamma separately for the initial 20 trials of each block and the remaining trials of each block (Table 4.2). For most blocks, stGamma across the initial 20 trials did not show a significant change; only for FIX in V1, a significantly negative slope was observed. By contrast, for the remaining trials, stGamma showed significant increases within each block and for both areas. The means of stGamma were higher in VAR2 than VAR1, and highest in FIX.

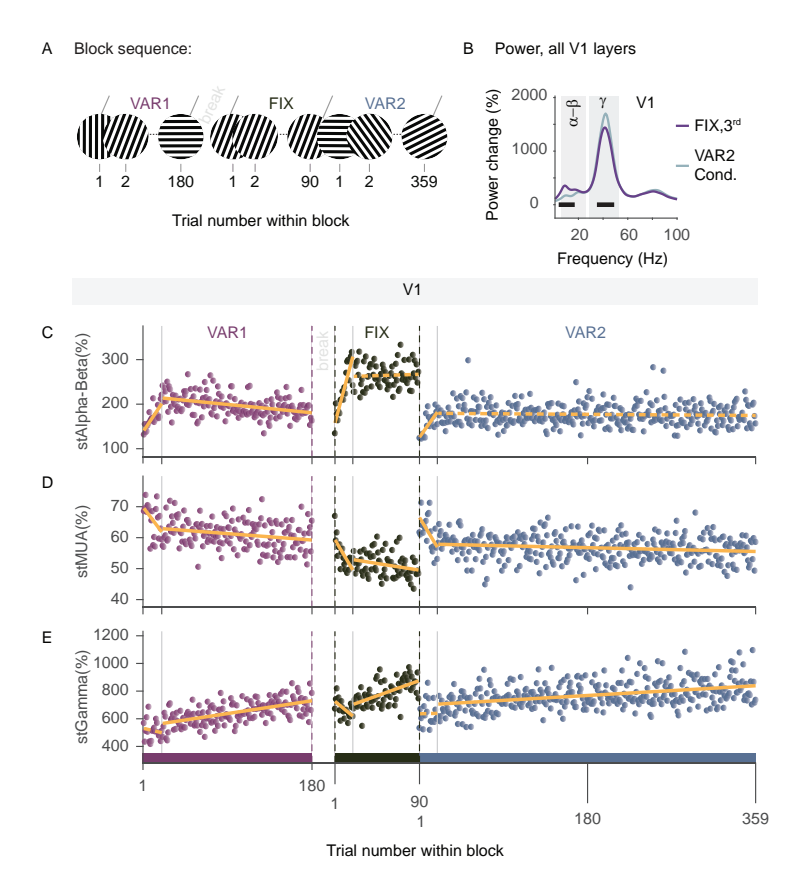


Figure 4.7. Comparison of neuronal responses in V1 across blocks. (A) Schematic representation of the block sequence within the session, and the trial number within the block. Note that for this and the following analyses, we included all trials that the monkey completed in VAR2 up to the minimal number available in all sessions. (B) Power change relative to baseline in response to the conditioned orientation in the 3rd repetition group in FIX (purple) and in VAR2 (light blue). Black horizontal lines show frequencies of significant difference between the conditions. Single-trial estimates for alphabeta (C), MUA (D), and gamma (E) are plotted for all trials (irrespective of stimulus orientation) as a function of trial number, color coded per block as indicated in A. Orange lines show the two regressions fitted per block for trials 1-20 and trials 21 until the end of that block. Grey vertical lines show the 20th trial in each block. Solid (dashed) lines indicate that the slopes of the respective linear fits are (not) significantly different from zero. The slopes and p-values are summarized in Supp. Table 4.1. A statistical comparison of the regression means is presented in Table 4.2.

 
 Table 4.2. Statistical comparison of the mean values of the regression fits between blocks. Reported are difference of the regression means
  $(\Delta s)$  and the corresponding p-values (p).

Comparisons	<b>Trial 1-20</b>	.20					Trials,	Trials 21-last block trial	ck trial			
	stAlpha-Beta	a-Beta	stMUA		stGamma	ma	tAlpha-Beta	ı-Beta	stMUA		stGamma	ma
	Δs	۵	Δs	۵	Δs	۵	Δs	ď	Δs	ď	Δs	ď
FIX-VAR1	59	<0.001	-11.2	<0.001	159.8	<0.001	67.4	<0.001	-9.9	<0.001	140.5	<0.001
VAR2-FIX	-75.9	<0.001	7.3	<0.001	-37.7	0.03	-87.6	<0.001	5.5	<0.001	-16.5	0.12
VAR2-VAR1	-16.9	<0.001	-3.9	900.0	122.1	<0.001	-20.3	<0.001	4.4	<0.001	124.1	<0.001
V2												
FIX-VAR1	Trial 1-20	.20					Trials?	Trials 21-last block trial	ck trial			
	Δs	Ь	Δs	р	Δs	d	Δs	d	Δs	d	Δs	d
	47.1	<0.001	-18	<0.001	36.7	<0.001	41.3	<0.001	-21.7	<0.001	44.1	<0.001
VAR2-FIX	-43.6	<0.001	2	900.0	-20.1	<0.001	-44.3	<0.001	11.8	<0.001	-17.3	<0.001
VAR2-VAR1	3.5	0.622	-13	<0.001	16.6	0.14	ς-	0.102	-9.9	<0.001	26.8	<0.001

### Discussion

#### **Summary**

- In accordance with previous studies, we found stimulus-specific MUA decreases and gamma increases with stimulus repetition (Peter et al., 2021; Stauch et al., 2021).
- We systematically investigated the level of stimulus specificity by presenting 18 orientations spaced by 10 ° before and after conditioning. By comparing neuronal responses before and after conditioning, we found that the conditioning effect is highly specific for the conditioned orientation.
- The repetition-related changes in gamma and MUA existed in all recorded laminar compartments.
- · Repetition-related changes in gamma and MUA were evident even when 18 different orientations were interleaved. This suggests that these effects might generalize to natural viewing conditions, where also many stimuli are expected to be interleaved.
- At the same time, we found clear indications that these changes were still stimulus specific, as VAR2 showed clear differences in intercept and slope of the regression for gamma between conditioned and non-conditioned orientations.
- Finally, we report changes of alpha-beta power and MUA across blocks that suggest a potential relation to stimulus predictability.

#### Limitations

The data presented here is from one monkey, which limits the inference to this sample. Note that almost all studies with awake macagues use few monkeys, i.e. typically two or three, and therefore, their inference is also limited to their sample, rather than to the population from which the sample has been drawn (see also Chapter 3).

Furthermore, our test of stimulus specificity was performed with a resolution of 10°, as we presented orientations spaced by this amount. Future studies might test finer steps, at least close to the conditioned orientation. We had opted against an uneven sampling of orientations during VAR1 and/or VAR2, because this would have also changed the probabilities of the different orientations, with unknown consequences for neuronal responses. The alternative, an evenly spaced sampling with smaller orientation steps would have resulted in a very large number of conditions and thereby a reduction in our sensitivity to observed effects. Yet, having established the effect here, future studies might be able to investigate the effect further, at higher resolution.

#### Gamma changes on different timescales

Previous studies of repetition-related gamma changes have reported (1) a strong gamma response for the first presentation of a given stimulus that rapidly declines over the course of the subsequent few (up to 10) repetitions (Friese et al., 2012; Gruber and Müller, 2002; Peter et al., 2021; Stauch et al., 2021), (2) a later, slower gamma increase that builds up over the course of further repetitions (Brunet et al., 2014; Peter et al., 2021; Stauch et al., 2021). These two patterns of gamma changes might reflect the superposition of two distinct dynamics, corresponding to two processes (Peter et al., 2021; Stauch et al., 2021). Specifically, it has been suggested that the strong initial gamma response reflects novelty detection, and the late gamma increase is related to synaptic plasticity (Peter et al., 2021; Stauch et al., 2021).

In the present study, we intended to investigate the late gamma increase. Therefore, in the analysis of FIX, we excluded the first 6 trials. Regarding the VARX blocks, each mini-block contained 18 different orientations, and thereby a putative novelty-related response might not show the same degree of decrease as seen in previous studies with repetitions of identical (Peter et al., 2021; Stauch et al., 2021), highly similar (Brunet et al., 2014), or very few distinct stimuli (Peter et al., 2021). Our analysis of VARX based on the repetitions of a specific stimulus across mini-blocks indeed showed no indication of a novelty effect for the first mini-block. In any case, in the present data, any novelty effect in gamma seemed weak, even in FIX, probably because the animals were highly overtrained on the very grating stimuli used during data collection.

# Repetition-related gamma increases occur in all laminar compartments of V1 and V2

While some studies indicate that visually-driven gamma synchronization is more prominent in superficial cortical layers (Bastos et al., 2018; Bastos et al., 2020; Buffalo et al., 2011), others report an additional peak in deep layers and a relative absence in the V1 input layer L4C (Gieselmann and Thiele, 2022; Roberts et al., 2013; van Kerkoerle et al., 2014; Xing et al., 2012). We found prominent visually induced gamma-band power in the bLFP from all laminar compartments of both V1 and V2. Note that the V1 granular compartment combined L4C with other L4 sublayers, such that the gamma observed for the entire granular compartment might primarily originate from outside L4C.

We investigated for the first time the laminar distribution of the late repetitionrelated increase of gamma. Interestingly, we found prominent repetition-related gamma increases in all laminar compartments of V1 and V2.

#### Potential mechanisms of late gamma-band increase

Stauch et al. (2021) suggested that the late repetition-related gamma increase might reflect plastic changes of the synaptic connectivity between excitatory and inhibitory neurons, and we will review their arguments here. Changes in the synaptic weights between excitatory and inhibitory neurons could emerge through the interaction between Hebbian spike-timing-dependent plasticity (STDP) and the spike timing in the gamma cycle that depends on the neuron's stimulus drivenness. Neurons in early visual cortex are tuned to specific features like orientation. For a given stimulus orientation, the most strongly stimulus-driven neurons tend to spike earlier in the gamma cycle than the most weakly driven ones (Fries et al., 2007; Vinck et al., 2010). Furthermore, within the gamma cycle, excitation is followed by inhibition within few milliseconds (Atallah and Scanziani, 2009; Csicsvari et al., 2003; Hasenstaub et al., 2005; Vinck et al., 2013). Together, these empirical results suggest that gamma-band activity induced by a particular stimulus entails an activation sequence of strongly stimulus driven excitatory neurons (E<sub>strong</sub>), followed by local inhibition (I<sub>local</sub>), followed by weakly stimulus driven excitatory neurons (E<sub>weak</sub>), or in short an E<sub>strong</sub>-I<sub>local</sub>-E<sub>weak</sub> sequence (Stauch et al., 2021). During stimulus repetition, the same  $E_{strong} - I_{local} - E_{weak}$  sequence is repeatedly activated, and typically followed by reward, providing ideal conditions for Hebbian STDP (Ahissar et al., 1992; Caporale and Dan, 2008).

Importantly, synaptic weights between connected neurons can be either potentiated or weakened depending on the temporal relation of their spiking: Inputs from the leading to the lagging neurons are typically strengthened, whereas inputs from the lagging to the leading neurons are typically weakened (Caporale and Dan, 2008). Thereby, the repeated activation of  $E_{\text{strong}}$ - $I_{\text{local}}$ - $E_{\text{weak}}$  could lead to a strengthening of the connections from  $E_{\text{strong}}$  to  $I_{\text{local}}$  and from  $I_{\text{local}}$  to  $E_{\text{weak}}$ . Strengthening of the connection from  $E_{\text{strong}}$  to  $I_{\text{local}}$  would allow the  $E_{\text{strong}}$  neurons to drive I<sub>local</sub> more efficiently and faster, which could explain both the increase in gamma-band power and in the peak frequency (Brunet et al., 2014; Peter et al., 2021; Stauch et al., 2021). A strengthening of the connections from  $I_{local}$  to  $E_{weak}$ neurons would lead to increased inhibition of the  $\mathsf{E}_{\mathsf{weak}}$  population, and thereby a sharpening of the neuronal population response. See Figure 6 in Stauch et al. (2021) for a schematic representation of the proposed mechanism.

The abovementioned mechanism (Stauch et al., 2021) could explain the high stimulus specificity that we report in this study. Note that this mechanism does not place strong constraints on the spatial scale, as long as the involved neurons engage in gamma-band synchronization, which has been found locally (Brunet et al., 2015; Fries et al., 2008; Gieselmann and Thiele, 2008, 2022; Peter et al., 2019; Roberts et al., 2013; Womelsdorf et al., 2006) and interareally (Bosman et al., 2012; Gregoriou et al., 2012; Gregoriou et al., 2009; Roberts et al., 2013). Thus, these plastic changes could take place within a layer of an activated cortical column, across an entire column, and between connected columns within an area or even between areas.

Among those options, a particularly intriguing one is that the late repetitionrelated gamma increases could be due to plastic changes of the intrinsic, i.e. intra-areal, horizontal connections. Those horizontal connections originate from excitatory neurons (Angelucci et al., 2002), target both excitatory and inhibitory neurons (McGuire et al., 1991), and they are orientation specific in superficial layers of V1 (Malach et al., 1993; Stettler et al., 2002). Plastic changes of these connections underlie cortical reorganization in macaque and cat V1 following retinal lesions (Darian-Smith and Gilbert, 1994; Das and Gilbert, 1995; Yamahachi et al., 2009), and also perceptual learning (for a review see Gilbert and Li (2012)). Importantly, horizontal connections have been suggested to play an important role in the generation of gamma oscillations (Gieselmann and Thiele, 2008; Peter et al., 2019; Uran et al., 2020; Vinck and Bosman, 2016). Electrophysiological recordings in cat V1 revealed that distant cortical columns with non-overlapping RFs synchronize in gamma only when they exhibit similar orientation preference (Gray et al., 1989). The orientation-selective anatomical and functional connectivity predict that during the repetition of a specific orientation, cortical columns preferentially tuned to the presented orientation are repeatedly activated and synchronize in gamma, entailing spiking with precise relative timing. This might lead to a strengthening of horizontal connectivity with maintained orientation specificity.

In fact, a putative involvement of intrinsic horizontal connections might explain our observation that the repetition-related changes showed more pronounced orientation selectivity for gamma than for MUA responses. Gamma might be specifically dependent on long-range horizontal connections, which are particularly orientation selective. This orientation selectivity might thereby be transferred to gamma and its changes with stimulus repetition.

In line with the potential interaction between Hebbian plasticity and gamma oscillations, Galuske et al. (2019) found that the repeated presentation of a grating leads to plastic changes of orientation domains in primary visual cortex of anesthetized cats. Importantly, the induced rearrangements of the orientation domains were only present under conditions of strong visually induced gamma. Thus, gamma oscillations seem to play an important role in cortical plasticity.

As an alternative explanation for the observed repetition-related changes, one might consider plastic changes of thalamocortical connections. However, developmental studies have shown that thalamocortical projections do not show experience-dependent changes after the critical period (Darian-Smith and Gilbert, 1995). Furthermore, gamma oscillations are cortically generated in awake primates (Bastos et al., 2014) and cats (Neuenschwander et al., 2023). Therefore, plastic changes of the thalamic input are unlikely to explain repetition-related gamma changes.

Stimulus repetition could also lead to plastic changes of cortico-cortical feedforward influences, leading to more efficient feedforward signaling. A human MEG study found that stimulus repetition leads to strengthening of feedforward influences in gamma from lower to higher cortical areas both in the ventral and dorsal visual streams (Stauch et al., 2021). Such increases could be mediated by local changes that increase the postsynaptic impact of bottom-up signals, by increased feedforward connectivity or both.

Finally, top-down signals could also contribute to repetition-related changes in lower areas. Area V1 receives the majority of its feedback projections from V2 (Markov et al., 2014a; Vanni et al., 2020), and interestingly, recent studies point to a crucial role of these V2-to-V1 projections in the generation of visually driven gamma and surround suppression in area V1. Reversible cooling of V2 drastically reduced visually driven gamma in V1 (Hartmann et al., 2019), and optogenetic inactivation of V2-to-V1 projections led to reductions in the surround suppression in V1 (Nurminen et al., 2018). Note that considerations mentioned here for V1 and its interactions with higher areas can be similarly made for V2 and its interactions with areas above it.

## Effects of stimulus repetition and predictability in the context of predictive coding

Theories of predictive coding propose that the brain uses prior knowledge to predict upcoming events and sensory input. Sensory inputs are compared and subtracted from sensory predictions, resulting in a prediction error signal. This is thought to happen in a cascaded fashion across the levels of the visual hierarchy, with prediction-error signals being fed forward in the bottom-up direction, and predictions being fed back in the top-down direction through the respective anatomical projections (Friston, 2005; Mumford, 1992; Rao and Ballard, 1999).

These bottom-up and top-down interactions have been linked with distinct neuronal rhythms (Bastos et al., 2015; Buschman and Miller, 2007; Michalareas et al., 2016; van Kerkoerle et al., 2014; Vezoli et al., 2021). Several studies suggest that top-down predictions are mediated by alpha and beta oscillations (Bastos et al., 2020; Chao et al., 2018; Mayer et al., 2016). Bastos et al. (2020) found higher alpha and beta power for predictable compared to unpredictable stimuli, and Chao et al. (2018) reported a beta-band power decrease during periods that required the update of sensory predictions. In line with these studies, we show that as a stimulus is repeated, alpha-beta power increases within a few trials and stays elevated until a prediction update is required, i.e. until an unexpected stimulus is presented (see transition from FIX to VAR2 in Fig. 4.7).

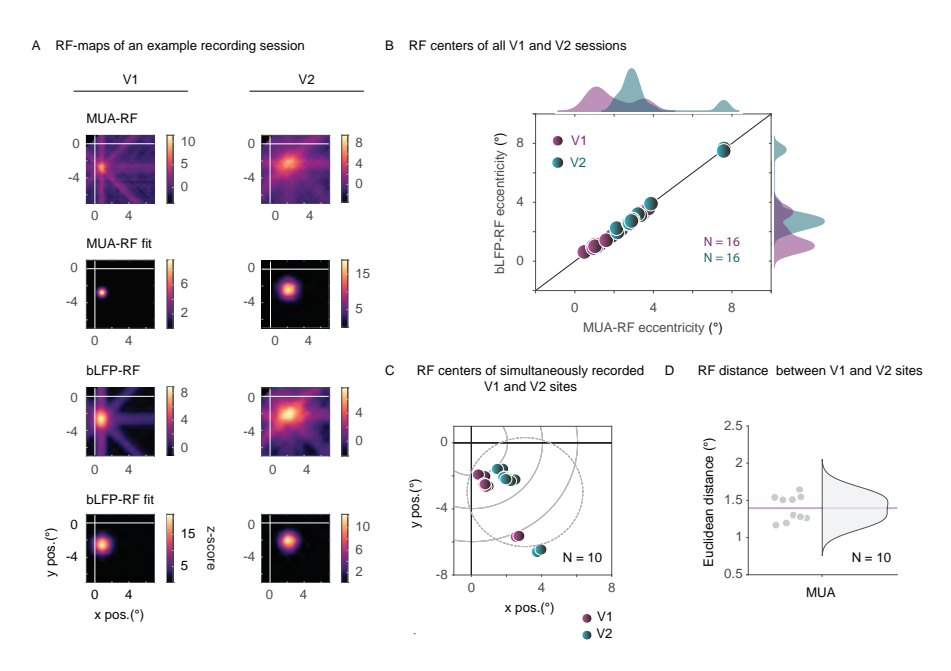
Gamma-band activity has been implicated in the bottom-up signalling of prediction errors, with stronger prediction errors leading to stronger gamma power (Bastos et al., 2020; Chao et al., 2018). This effect has also been supported by previous stimulus-repetition studies (Peter et al., 2021; Stauch et al., 2021): The first presentation of a novel stimulus led to a strong gamma-band response, which rapidly decreased over the course of the next few repetitions when the stimulus turned more predictable. Interestingly, these changes in gamma during the first few repetitions of a stimulus were prominent for novel (Peter et al., 2021; Stauch et al., 2021) but not for familiar stimuli like grating stimuli on which animals had been overtrained (Peter et al., 2021).

In the present study, we exclusively used such overtrained gratings and confirmed this previous finding. We focused our investigation of gamma on the late repetition-related increase. This effect might also be explained in the context of predictive coding. A generalization of the predictive coding framework posits that sensory inputs and their associated prediction errors are modulated by their inverse variance or precision (Brown and Friston, 2012; Feldman and Friston, 2010). The precision of a prediction error is thought to be context dependent and to modulate its postsynaptic gain, with increased precision leading to increased postsynaptic gain. The late repetition-related gamma-band increase could mediate this increased postsynaptic gain as precision rises with repetition. While spiking

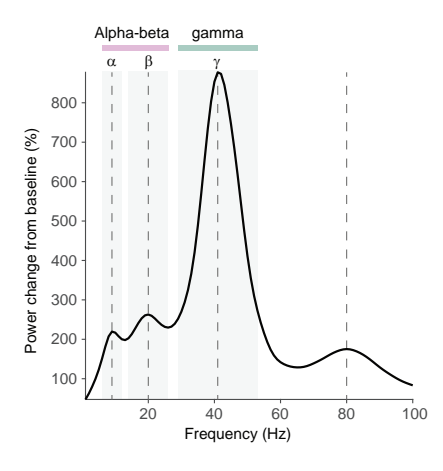
activity is decreased during repetitions, an increase in gamma synchrony could maintain or even boost the postsynaptic impact of the remaining spiking by means of increased feedforward coincidence detection (Gotts et al., 2012) or by increased postsynaptic entrainment (Fries, 2015).

## **Supplementary materials**

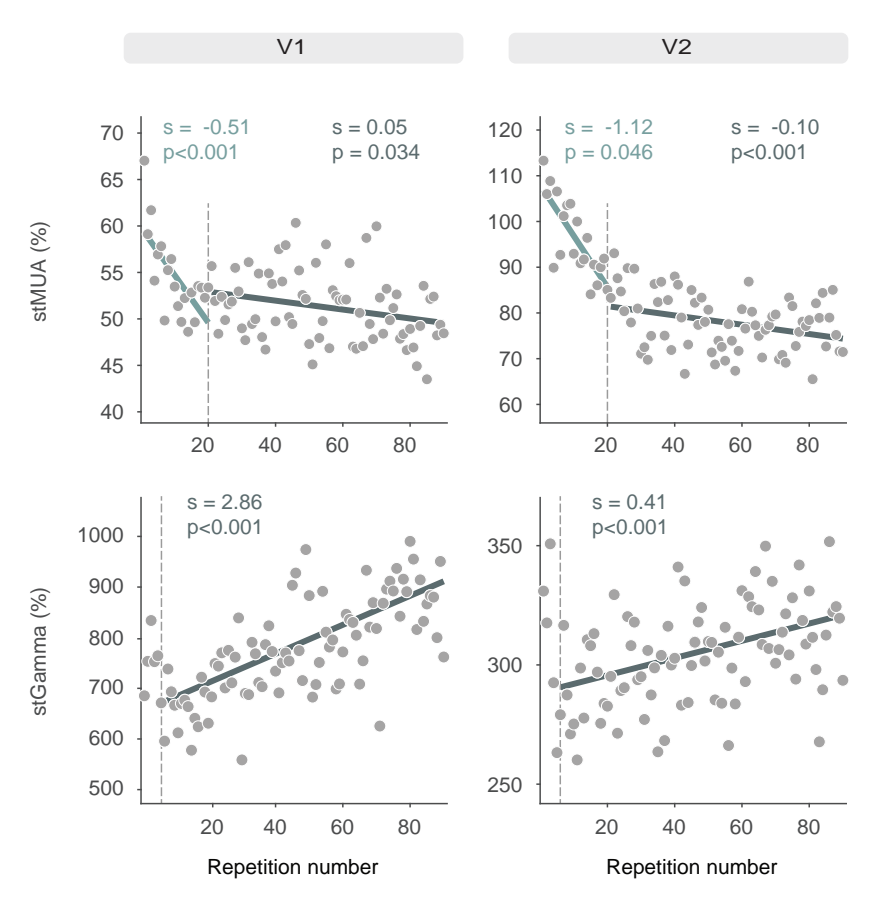
#### Supplementary figures



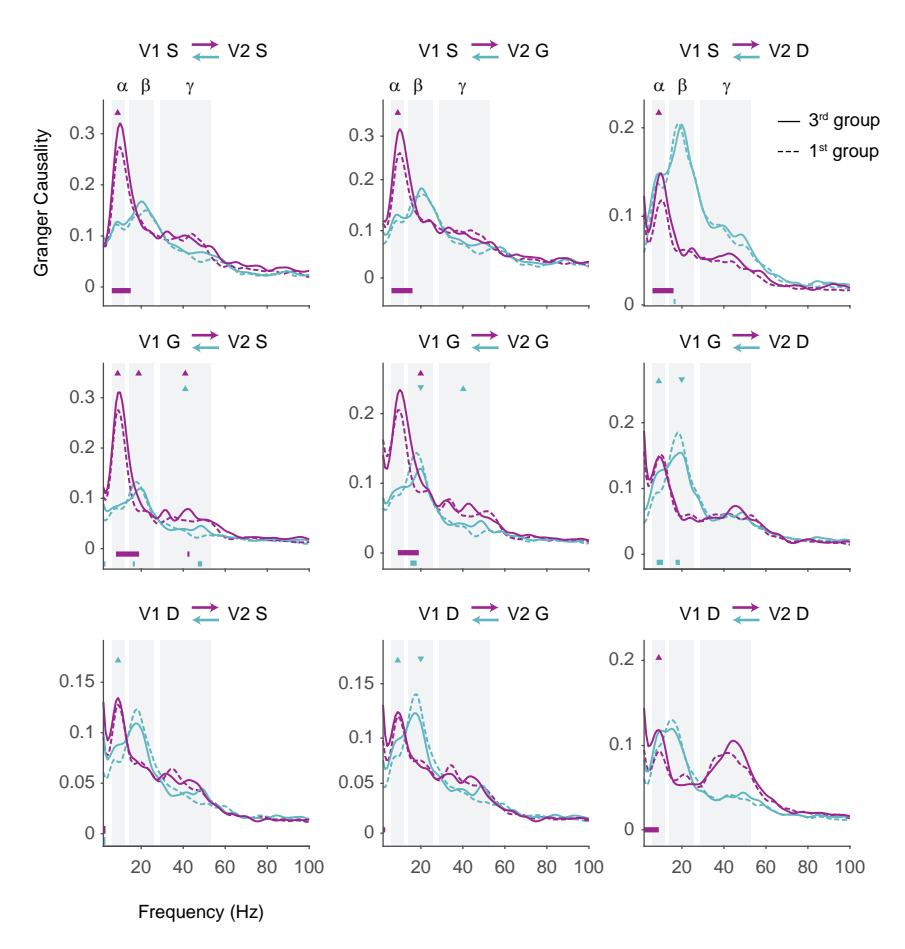
Suppl. Figure 4.1. Examples and distributions of receptive fields (RFs). (A) MUA- and bLFP-RF maps of example recording sites in V1 (left) and V2 (right) and their respective Gaussian fits that were used to calculate the coordinates of the RF centers. For B-C, each dot represents the average over all contacts within one area in one session. (B) bLFP- and MUA-RF centers. Recording sessions in V1 (N=16) and V2 (N=16) are color-coded in magenta and green, respectively. Note the strong similarity between bLFPand MUA-RF centers. (C) MUA-RF centers of all sessions with simultaneous recordings in V1 and V2 (N=10). Same color-coding as in (B), (D) Euclidean distances between simultaneously recorded V1- and V2-RF centers shown in (C). The pink horizontal line indicates the mean Euclidean distance.



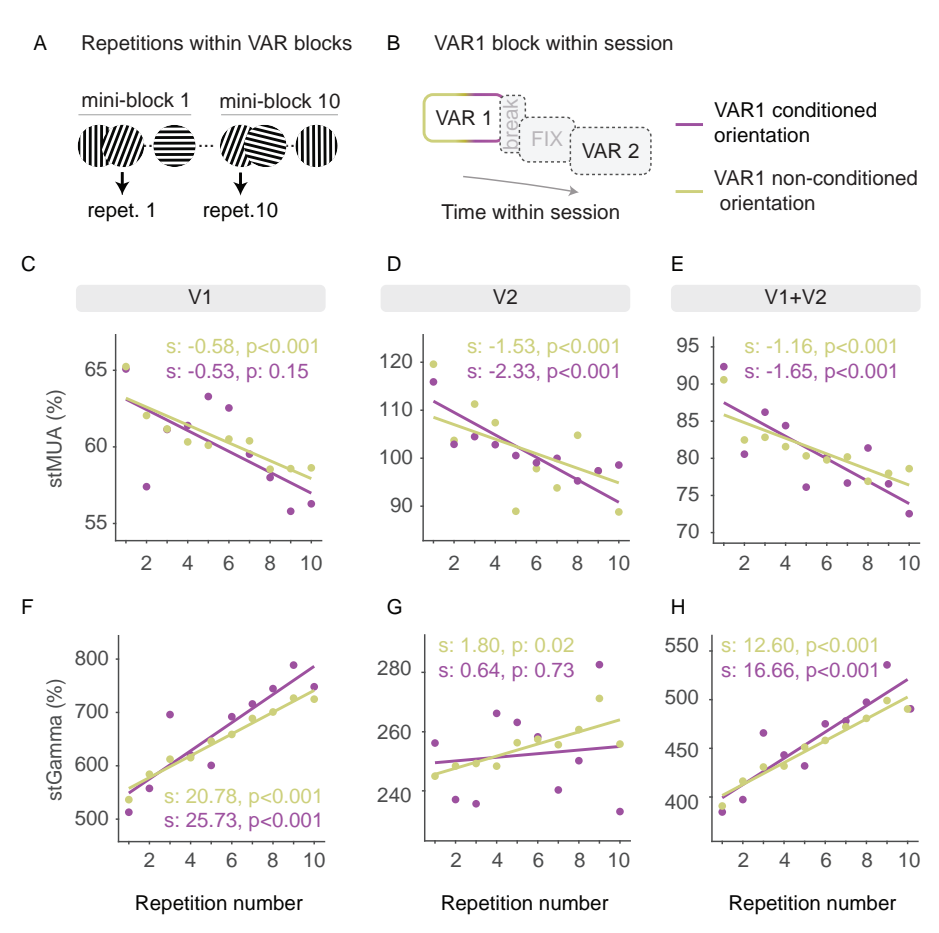
**Suppl. Figure 4.2.** *Definition of frequency bands.* Power change relative to baseline averaged over all V1 and V2 recording sites. Dashed lines indicate the four distinct spectral peaks (at 9, 20, 41 and 80 Hz) that guided the definition of frequency bands. Based on these peaks, an alpha (6-12 Hz), a beta (14-26 Hz) and a gamma band (29-53 Hz) were defined (see Methods for details). Grey rectangles indicate each band and outline their respective frequency limits. Some analyses used a combined alpha-beta band (6-26 Hz), shown as a pink rectangle on top of the panel.



**Suppl. Figure 4.3.** Single-trial estimates averaged over laminar compartments during FIX. stMUA (top) and stGamma (bottom) were averaged over laminar compartments of V1 (left) and V2 (right). For stMUA, the dashed vertical line indicates trial 20, and two separate regressions were performed for the Early-20 repetition group and the Remaining-70 repetition group (see Fig. 4.2A). For stGamma, the dashed vertical line indicates trial 7, and one regression was performed for repetitions 7-90. The slopes (s) and p-values (p) for each fit are color-coded and reported on top of each panel.



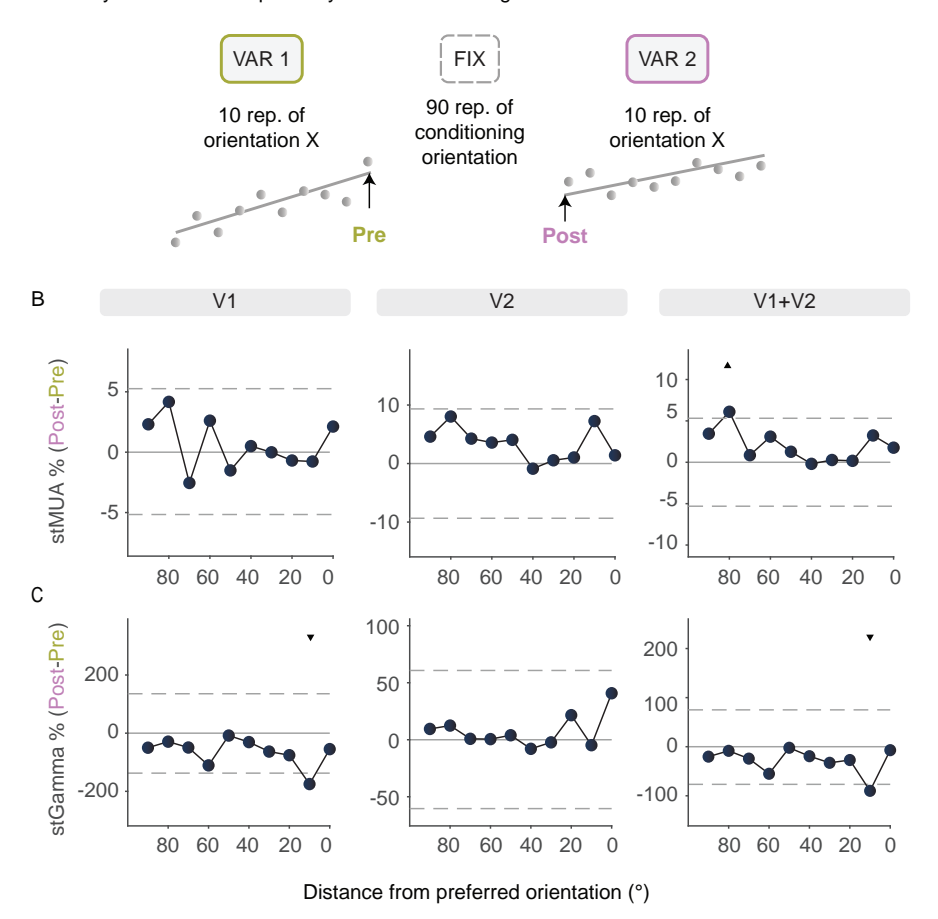
**Suppl. Figure 4.4.** Granger Causality between laminar compartments of areas V1 and V2 during the 1st repetition group (dashed line) and 3rd repetition group (solid line) of FIX. Note that the RF centers of the simultaneously recorded sites in V1 and V2 (N = 9 sessions) were largely non-overlapping (see Suppl. Fig. 4.1C-D). Different colors represent the GC direction (magenta for V1-to-V2 feedforward; green for V2-to-V1 feedback). Grey rectangles show the three frequency bands that were used for statistical comparison: alpha ( $\alpha$ ), beta ( $\beta$ ), and gamma ( $\gamma$ ). Triangles show statistical significance per frequency band, with the triangles pointing upward for increases and downward for decreases. Horizontal lines at the bottom of the plots indicate significant differences across frequencies, color-coded for feedforward and feedback directions.



Suppl. Figure 4.5. Control analysis: Repetition-related changes during VAR1 for conditioned and nonconditioned orientations. (A) Schematic representation of stimulus repetitions across mini-blocks in VARX, illustrating that a given orientation occurred at a random position per mini-block. (B) Block sequence within a recording session. (C - E) stMUA as a function of the repetition number of a given stimulus orientation across the mini-blocks. Neuronal responses were divided into two groups: responses for non-conditioned orientations and responses for the orientation that was later-on conditioned in FIX. Each group is color-coded and presented for V1 (C), V2 (D) and combined V1+V2 (E). Solid lines indicate the respective linear fits. Slopes (s) and their p-values (p) are color-coded and reported at the top of each panel. (F - H) Same as C-E, but for stGamma.

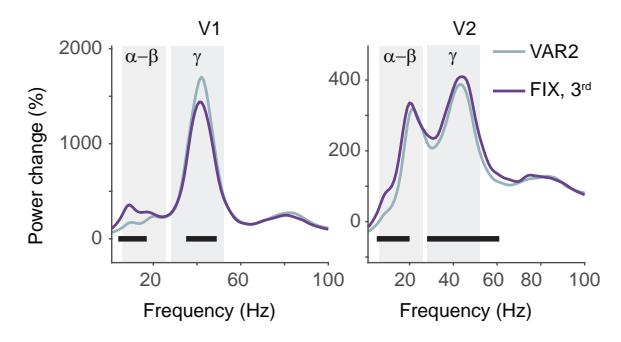
Results of the statistical comparisons of repetition-related stMUA changes between conditioned and non-conditioned orientations in VAR1 (listed are the p-values): (1) difference between slopes: V1: 0.56, V2: 0.28, V1+V2: 0.28; (2) difference between intercepts: V1: 0.39, V2: 0.85, V1+V2: 0.71. Results of the statistical comparisons of repetition-related stGamma changes between conditioned and nonconditioned orientations in VAR2 (listed are the p-values): (1) difference between slopes: V1: 0.49, V2: 0.24, V1+V2: 0.79; (2) difference between intercepts: V1: 0.59, V2: 0.38, V1+V2: 1.

#### A Analysis of stimulus specificity of the conditioning effects

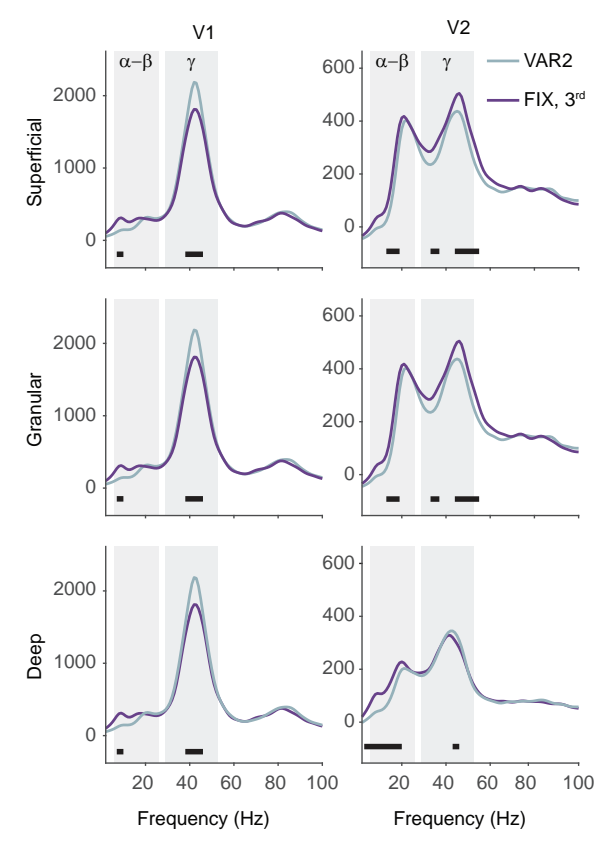


**Suppl. Figure 4.6**. Control analysis: Repetition-related changes relative to the orientation distance from the preferred orientation. Same as Fig. 4.6, but as a function of the orientation distance from the preferred orientation. To ease direct comparison, the Y-axis limits are the same as in the respective panels of Fig. 4.6.

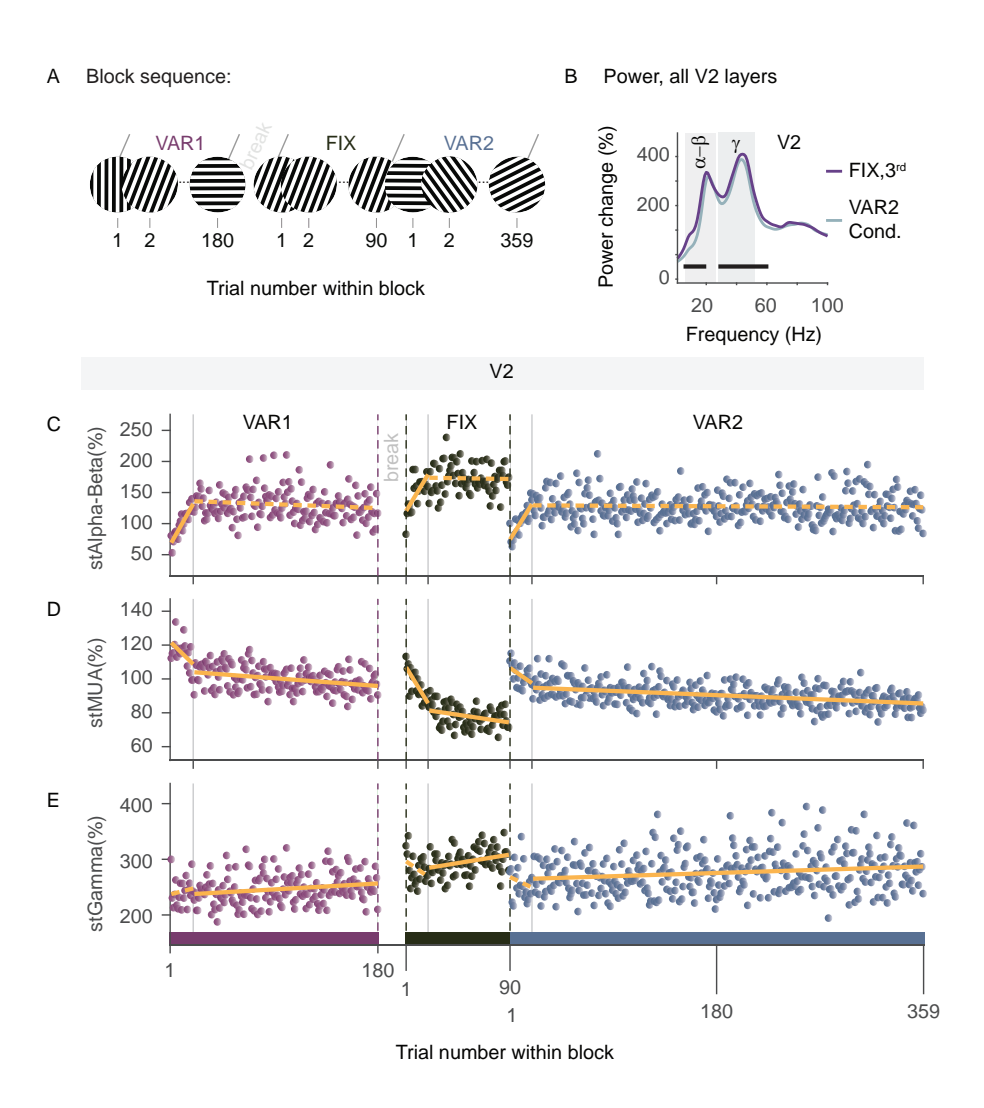
#### Power, all layers



#### В Power per laminar compartment



Suppl. Figure 4.7. Comparison of average power between FIX and VAR2. (A) Power change relative to baseline in response to the conditioned orientation in the 3<sup>rd</sup> repetition group in FIX (purple) and in VAR2 (light blue), separately for V1 (left) and V2 (right). (B) Same as (A) but per laminar compartment. Black horizontal lines denote frequencies where significant differences were observed between the two conditions. Grey rectangles indicate the alpha-beta and gamma frequency bands that were used for single-trial estimates in Fig. 4.7. The left panel of (A) is identical to Fig. 4.7b and is reproduced here to facilitate the direct comparison between V1 and V2.



**Suppl. Figure 4.8.** Comparison of neuronal responses in V2 across blocks. Same as Fig. 7, but for area V2. The slopes and p-values are summarized in Suppl. Table 4.1. A statistical comparison of the regression means is presented in Table 4.2.

Supplementary tables

**Suppl. Table 4.1**. Summary of regression slopes and their p-values for Figure 4.7 and Suppl. Figure 4.8.

V1												
Block	stAlpha	a-Beta			stMUA				stGamma	la		
	Trials 1-2	-20	Trials 2'	Trials 21-last block trial	Trials 1-20	20	Trials 21 trial	Trials 21-last block trial	Trials 1-20	20	Trials 21 trial	Trials 21-last block trial
	slope	ď	slope	ď	slope	۵	slope	۵	slope	۵	slope	۵
VAR1	3.19	<0.001	-0.21	<0.001	-0.41	0.05	-0.03	<0.001	-1.63	0.542	1.04	<0.001
FIX	7.84	<0.001	0.07	9/90	-0.52	<0.001	-0.05	0.034	-5.62	0.018	2.45	<0.001
VAR2	2.97	<0.001	-0.02	0.282	-0.51	0.002	-0.01	<0.001	0.16	0.938	0.4	<0.001
V2												
Block	stAlpha	-Beta			stMUA				stGamma	la		
	slope	d	slope	ď	slope	۵	slope	ď	slope	۵	slope	Ф
VAR1	3.09	<0.001	-0.07	0.09	9.0-	0.046	-0.06	<0.001	0.75	0.586	0.12	0.01
FIX	2.92	<0.001	-0.01	0.85	-1.15	<0.001	-0.11	900.0	-1.51	0.154	0.29	0.012
VAR2	2.79	<0.001	-0.01	0.438	-0.56	0.03	-0.03	<0.001	-0.98	0.47	90.0	0.002

#### **Author Contributions**

**Eleni Psarou**: Conceptualization, Methodology, Investigation, Software, Formal analysis, Visualization, Writing - Original Draft, Writing - Review & Editing. **Mohsen Parto Dezfouli**: Software, Formal analysis, Visualization, Writing - Review & Editing. **Iris Grothe**: Methodology, Writing - Review & Editing. **Alina Peter**: Conceptualization, Writing - Review & Editing. **Rasmus Roese**: Methodology, Writing - Review & Editing. **Pascal Fries**: Conceptualization, Methodology, Investigation, Writing - Original Draft, Writing - Review & Editing, Supervision, Project administration, Resources, Funding acquisition.

#### **Declaration of interest**

P.F. has a patent on thin-film electrodes and is a member of the Advisory Board of CorTec GmbH (Freiburg, Germany).

## **Acknowledgements**

We thank Christini Katsanevaki, Dr. Benjamin Stauch, and Yufeng Zhang for inspiring discussions and invaluable scientific input. We thank Marianne Hartmann, Julia Hoffmann, Sabrina Wallrath, and Johanna Klon-Lipok for their assistance in animal care and surgical procedures. We are grateful to Dr. Christa Tandi and Dr. Alf Theisen who provided excellent veterinary care and advice. We also thank the technical service teams of the Ernst Strüngmann Institute for their exceptional technical support. P.F. acknowledges grant support by the German Research Foundation (FR2557/1-1, FR2557/2-1, FR2557/5-1, FR2557/7-1), the European Union (HEALTH-F2-2008-200728-BrainSynch, FP7-604102-HBP) and a European Young Investigator Award.



# Chapter 5

# **General discussion**

## **Summary of findings**

Chapter 2 described the planning, production, and implantation of modular, cement-free titanium cranial implants for macaques. Results from 12 animals confirmed the methods' success and suitability. The modular design allowed for a two-step implantation approach, resulting in long-lasting, healthy implants over 9 years post-implantation. To our knowledge, this is the longest follow-up reported for headpost implants. Post-operative CT scans confirmed the safety of using length-adjusted bone screws tailored to skull thickness. The two-step approach, combined with a punch tool, ensured a tight fit around the headpost without the need for additional sutures. These modifications likely contributed to irritation-free wound margins and implant stability over extended periods of time. The presented methods constitute an implementation of the 3R principles by refining implant techniques, minimizing the need for re-implantations, and potentially reducing animal numbers for future experiments.

Chapter 3 examined the statistical inference that is achieved with small sample sizes as traditionally used in NHP studies. The chapter critically discussed a recent framework that suggested testing three animals and considering the outcome that is present in the majority of animals as representative of the population (Laurens, 2022). We showed that the error rate of this framework heavily depends on the typicality of the outcomes, requiring a high typicality (87%) to achieve acceptable error rates. We also found that moving from one to three animals decreased error rates mainly for typicality values of 70-90%, and much less for lower and higher values. Furthermore, using conjunction analysis, we estimated the lower bound to typicality for a range of small sample sizes (up to M=10) with N out of M subjects showing an outcome. To improve transparency in publications, we recommended that studies with small sample sizes report the inferred lower bound to typicality.

Chapter 4 investigated the effects of stimulus repetition on gamma oscillations and spike rates. In agreement with previous studies, we showed that stimulus repetition led to stimulus-specific MUA decreases and gamma increases (Peter et al., 2021; Stauch et al., 2021). By presenting gratings of 18 orientations spaced by 10 ° before and after conditioning, we demonstrated that repetition-related changes in gamma were specific for the conditioned orientation, i.e. they did not transfer to other orientations. Repetition-related changes in gamma and MUA were observed across

all laminar compartments and were evident even when 18 different orientations were repeated interleaved, suggesting potential generalization to natural viewing conditions. Furthermore, the repetition-related plasticity in gamma during the repetition of interleaved orientations was also stimulus specific. Finally, we reported changes in alpha-beta power and MUA across blocks, potentially related to differences in stimulus predictability across the three blocks.

## Fostering methodological refinements in NHP research

Cranial implants for NHPs have seen significant refinements over the past decades, leading to improved implantation outcomes, increased implant longevity, and better animal welfare. Although Chapter 2 focused on the development of headpost and connector-chamber implants, similar modular designs and two-step implantation approaches could also improve other types of cranial implants, such as recording chambers.

NHP neuroscience would greatly benefit from more longitudinal studies reporting the long-term outcomes of employed methods, as well as suboptimal results that can prompt future refinements. An excellent example is provided by Pfingst et al. (1989), who reported results from 50 cranial implants developed for monkeys and implanted over several years. Crucially, the authors documented implant failures, which guided their subsequent efforts towards new refinements. Such reports provide invaluable insights for other researchers, helping them make informed methodological choices while avoiding suboptimal approaches, thereby promoting animal welfare.

Additionally, cross-laboratory surveys can allow an in-depth assessment of different methodological approaches. By collecting data from several labs, these surveys can identify practices linked to better or suboptimal outcomes in a variety of research settings. Importantly, such surveys can be easily conducted in the form of questionnaires or interviews and are low cost (for an example see Adams et al. (2007)).

Open-access databases can also allow researchers to make informed decisions about their methodological approaches. For instance, Tremblay et al. (2020) presented an impactful initiative aimed at promoting and accelerating the use of optogenetic manipulations in NHPs. They constructed a large open-access database where multiple laboratories reported optogenetic experiments and protocols. Crucially, such initiatives provide a platform to report valuable unpublished data.

Finally, while the main focus of the literature has been on the development of implants and implantation approaches, explantation techniques are rarely discussed (for an exception, see the supplementary materials of Mahmoudian et al. (2023)). The dissemination of detailed explantation protocols could enable researchers to design implants that are easier to remove or replace if necessary, improving both experimental outcomes and animal welfare.

## Fostering statistical inference in NHP research

Despite the challenges posed by small sample sizes, neurophysiological studies in NHPs have been instrumental in advancing our understanding of the primate brain, leading to fundamental discoveries about its organization and function (Asaad and Sheth, 2024). Although the number of animals per study will likely remain low, there are steps that can be taken to enhance statistical inference in the field.

Open-science initiatives and collaborations between laboratories allow researchers to combine or re-analyse data. By aggregating data from studies conducted in various labs under comparable experimental procedures, researchers can improve the generalizability of the observed results while effectively increasing sample sizes.

In addition, meta-analyses of previous studies could boost the statistical power and generalizability of findings (Papakostidis and Giannoudis, 2023). Currently, meta-analyses of NHP neuroscience studies are not realized. Yet, there are scientific questions that have been extensively studied over the past decades (e.g.: the effect of spatial attention on spike rates) that could allow meta-analysis to be conducted. Such studies would allow researchers to identify inconsistencies, patterns, and general trends that may not be evident in individual studies alone.

Importantly, results obtained from a small NHP sample can motivate and guide studies in a large sample of human participants using non-invasive techniques. For instance, Stauch et al. (2021) investigated in humans the repetition-related gammaband increase initially found in the macaque visual cortex (Brunet et al., 2014). In parallel with the study of Peter et al. (2021) in macaques, Stauch et al. (2021) examined stimulus-specific repetition effects in gamma activity in thirty healthy human participants. Using MEG recordings, the authors were able to: 1) replicate

the repetition-related increase in gamma in the human visual cortex; and 2) draw an inference on the population of humans by collecting data from a large cohort of participants.

However, it is important to note that parallel studies in NHPs and humans are not always feasible. Currently, non-invasive recording methods like fMRI, MEG and EEG only provide population signals. Thus, scientific questions that require recordings of neuronal spiking or cell-type-specific causal manipulations cannot be readily addressed with non-invasive methods in humans. Note that studies with invasive techniques in humans are often also bound to small sample sizes (typically less than 2; Asaad and Sheth (2024)).

## Repetition-related plasticity: open questions and outlook

In our stimulus-repetition study, we found a conspicuous repetition-related increase in gamma activity across all layers of V1 and V2. The gamma-band increase was highly stimulus-specific and evident even when several stimuli were repeated interleaved. These findings suggest that under natural conditions, where multiple stimuli are interleaved, similar plastic changes might take place. In natural settings, a significant portion of the repeated visual input we receive is linked to eye movements, as we tend to revisit task-relevant objects (Hayhoe and Ballard, 2005). Future studies could investigate the effects of stimulus repetition under free-viewing conditions and compare the neuronal activity in early versus late eye fixations on a given object.

The repetition-related plasticity could emerge through changes of the synaptic connectivity at various stages, either within an area and/or between areas (see Chapter 4 for a detailed discussion of this topic). An intriguing possibility is that the highly orientation-specific gamma plasticity arises from a strengthening of the intra-areal horizontal connectivity, which occurs with the repeated activation of these connections. Horizontal connections, particularly in the superficial layers of V1, tend to connect columns with similar orientation preferences (Lund et al., 2003; Malach et al., 1993; Stettler et al., 2002) and have been implicated in the generation of both gamma oscillations (Vinck and Bosman, 2016) and the near-surround suppression (Angelucci et al., 2017).

Interestingly, Shushruth et al. (2013) found that the near-surround suppression is highly orientation selective both in monkey V1 as well as in human perception. This orientation selectivity resembles the selectivity we found for the late gamma plasticity. The same authors found that the effects of far-surround suppression are not sharply tuned for orientation. Note that intra-areal horizontal connections are thought to mediate the effects of near-surround stimulation while feedback projections are thought to be responsible for the effects of far-surround stimulations (Angelucci et al., 2017). Future studies could compare the degree of orientation selectivity when gratings of different sizes (designed to activate either only the near-surround or both the near- and far-surround fields) are repeated in time.

Finally, we found pronounced changes in alpha-beta power across blocks that seemed to be related to the level of stimulus predictability. Even though our analysis focused on the time window during which the stimulus was presented, one could expect the effects of stimulus predictability to be already evident in the baseline period, before stimulus presentation. In the first few trials of each block, the monkey could potentially create expectations about the likelihood of the presented stimulus/stimuli. Along these lines, Bastos et al. (2020) reported increased beta activity (15-30 Hz) in the baseline period of blocks with predictable stimuli. Future analyses of our data could compare the neuronal responses during baseline between FIX and VAR blocks across trials.



# **Bibliography**

- Adams, D.L., Economides, J.R., Jocson, C.M., and Horton, J.C. (2007). A biocompatible titanium headpost for stabilizing behaving monkeys. Journal of neurophysiology 98, 993-1001.
- Adams, D.L., Economides, J.R., Jocson, C.M., Parker, J.M., and Horton, J.C. (2011). A watertight acrylic-free titanium recording chamber for electrophysiology in behaving monkeys. Journal of neurophysiology *106*, 1581-1590.
- Ahissar, E., Vaadia, E., Ahissar, M., Bergman, H., Arieli, A., and Abeles, M. (1992). Dependence of cortical plasticity on correlated activity of single neurons and on behavioral context. Science *257*, 1412-1415.
- Ahmed, Z., Agha, N., Trunk, A., Berger, M., and Gail, A. (2022). Universal Guide for Skull Extraction and Custom-Fitting of Implants to Continuous and Discontinuous Skulls. eNeuro 9.
- Anderson, J.C., and Martin, K.A. (2009). The synaptic connections between cortical areas V1 and V2 in macaque monkey. J Neurosci *29*, 11283-11293.
- Angelucci, A., Bijanzadeh, M., Nurminen, L., Federer, F., Merlin, S., and Bressloff, P.C. (2017). Circuits and Mechanisms for Surround Modulation in Visual Cortex. Annual review of neuroscience 40, 425-451.
- Angelucci, A., Levitt, J.B., Walton, E.J., Hupe, J.M., Bullier, J., and Lund, J.S. (2002). Circuits for local and global signal integration in primary visual cortex. J Neurosci 22, 8633-8646.
- Asaad, W.F., and Sheth, S.A. (2024). What's the n? On sample size vs. subject number for brain-behavior neurophysiology and neuromodulation. Neuron.
- Atallah, B.V., and Scanziani, M. (2009). Instantaneous modulation of gamma oscillation frequency by balancing excitation with inhibition. Neuron *62*, 566-577.
- Bartoli, E., Bosking, W., Chen, Y., Li, Y., Sheth, S.A., Beauchamp, M.S., Yoshor, D., and Foster, B.L. (2019). Functionally Distinct Gamma Range Activity Revealed by Stimulus Tuning in Human Visual Cortex. Curr Biol *29*, 3345-3358 e3347.
- Bastos, A.M., Briggs, F., Alitto, H.J., Mangun, G.R., and Usrey, W.M. (2014). Simultaneous recordings from the primary visual cortex and lateral geniculate nucleus reveal rhythmic interactions and a cortical source for gamma-band oscillations. J Neurosci 34, 7639-7644.
- Bastos, A.M., Loonis, R., Kornblith, S., Lundqvist, M., and Miller, E.K. (2018). Laminar recordings in frontal cortex suggest distinct layers for maintenance and control of working memory. Proc Natl Acad Sci U S A 115, 1117-1122.
- Bastos, A.M., Lundqvist, M., Waite, A.S., Kopell, N., and Miller, E.K. (2020). Layer and rhythm specificity for predictive routing. Proc Natl Acad Sci U S A.
- Bastos, A.M., Vezoli, J., Bosman, C.A., Schoffelen, J.M., Oostenveld, R., Dowdall, J.R., De Weerd, P., Kennedy, H., and Fries, P. (2015). Visual areas exert feedforward and feedback influences through distinct frequency channels. Neuron 85, 390-401.
- Betelak, K.F., Margiotti, E.A., Wohlford, M.E., and Suzuki, D.A. (2001). The use of titanium implants and prosthodontic techniques in the preparation of non-human primates for long-term neuronal recording studies. Journal of neuroscience methods 112, 9-20.
- Blonde, J.D., Roussy, M., Luna, R., Mahmoudian, B., Gulli, R.A., Barker, K.C., Lau, J.C., and Martinez-Trujillo, J.C. (2018). Customizable cap implants for neurophysiological experimentation. Journal of neuroscience methods *304*, 103-117.
- Bosman, C.A., Schoffelen, J.M., Brunet, N., Oostenveld, R., Bastos, A.M., Womelsdorf, T., Rubehn, B., Stieglitz, T., De Weerd, P., and Fries, P. (2012). Attentional stimulus selection through selective synchronization between monkey visual areas. Neuron *75*, 875-888.
- Brown, H.R., and Friston, K.J. (2012). Dynamic causal modelling of precision and synaptic gain in visual perception an EEG study. Neuroimage *63*, 223-231.

- Brunet, N., Bosman, C.A., Roberts, M., Oostenveld, R., Womelsdorf, T., De Weerd, P., and Fries, P. (2015). Visual cortical gamma-band activity during free viewing of natural images. Cereb Cortex 25, 918-926.
- Brunet, N.M., Bosman, C.A., Vinck, M., Roberts, M., Oostenveld, R., Desimone, R., De Weerd, P., and Fries, P. (2014). Stimulus repetition modulates gamma-band synchronization in primate visual cortex. Proc Natl Acad Sci U S A 111, 3626-3631.
- Brunet, N.M., and Fries, P. (2019). Human visual cortical gamma reflects natural image structure. NeuroImage 200, 635-643.
- Buffalo, E.A., Fries, P., Landman, R., Buschman, T.J., and Desimone, R. (2011). Laminar differences in gamma and alpha coherence in the ventral stream. Proc Natl Acad Sci U S A 108, 11262-11267.
- Buschman, T.J., and Miller, E.K. (2007). Top-down versus bottom-up control of attention in the prefrontal and posterior parietal cortices. Science 315, 1860-1862.
- Buzsáki, G., and Wang, X.J. (2012). Mechanisms of gamma oscillations. Annual review of neuroscience 35, 203-225.
- Caporale, N., and Dan, Y. (2008). Spike Timing-Dependent Plasticity: A Hebbian Learning Rule. 31, 25-
- Cardin, J.A., Carlén, M., Meletis, K., Knoblich, U., Zhang, F., Deisseroth, K., Tsai, L.H., and Moore, C.I. (2009). Driving fast-spiking cells induces gamma rhythm and controls sensory responses. Nature 459, 663-667.
- Chao, Z.C., Takaura, K., Wang, L., Fujii, N., and Dehaene, S. (2018). Large-Scale Cortical Networks for Hierarchical Prediction and Prediction Error in the Primate Brain. Neuron 100, 1252-1266 e1253.
- Chen, X., Possel, J.K., Wacongne, C., van Ham, A.F., Klink, P.C., and Roelfsema, P.R. (2017). 3D printing and modelling of customized implants and surgical guides for non-human primates. Journal of neuroscience methods 286, 38-55.
- Clopper, C.J., and Pearson, E.S. (1934). The use of confidence or fiducial limits illustrated in the case of the binomial. Biometrika 26, 404-413.
- Colman, R.J., and Anderson, R.M. (2011). Nonhuman primate calorie restriction. Antioxid Redox Signal 14, 229-239.
- Cragg, B.G. (1969). The topography of the afferent projections in the circumstriate visual cortex of the monkey studied by the Nauta method. Vision Res 9, 733-747.
- Csicsvari, J., Jamieson, B., Wise, K.D., and Buzsáki, G. (2003). Mechanisms of gamma oscillations in the hippocampus of the behaving rat. Neuron 37, 311-322.
- Darian-Smith, C., and Gilbert, C.D. (1994). Axonal sprouting accompanies functional reorganization in adult cat striate cortex. Nature 368, 737-740.
- Darian-Smith, C., and Gilbert, C.D. (1995). Topographic reorganization in the striate cortex of the adult cat and monkey is cortically mediated. J Neurosci 15, 1631-1647.
- Das, A., and Gilbert, C.D. (1995). Long-range horizontal connections and their role in cortical reorganization revealed by optical recording of cat primary visual cortex. Nature 375, 780-784.
- Dhamala, M., Rangarajan, G., and Ding, M. (2008). Estimating Granger causality from fourier and wavelet transforms of time series data. Physical review letters 100, 018701.
- Douglas, R.J., and Martin, K.A. (2004). Neuronal circuits of the neocortex. Annual review of neuroscience 27, 419-451.
- Dowdall, J.R., Schmiedt, J.T., Stephan, M., and Fries, P. (2018). ARCADE: a modular multithreaded stimulus presentation software for the real-time control of stimuli, actions and reward during behavioral experiments. Paper presented at: Society for Neuroscience (San Diego, CA).

- Dubowitz, D.J., and Scadeng, M. (2011). A frameless stereotaxic MRI technique for macaque neuroscience studies. Open Neuroimag J *5*, 198-205.
- Engel, A.K., Kreiter, A.K., Konig, P., and Singer, W. (1991). Synchronization of oscillatory neuronal responses between striate and extrastriate visual cortical areas of the cat. Proc Natl Acad Sci U S A 88, 6048-6052.
- Fedorov, A., Beichel, R., Kalpathy-Cramer, J., Finet, J., Fillion-Robin, J.C., Pujol, S., Bauer, C., Jennings, D., Fennessy, F., Sonka, M., *et al.* (2012). 3D Slicer as an image computing platform for the Quantitative Imaging Network. Magnetic resonance imaging *30*, 1323-1341.
- Feldman, H., and Friston, K.J. (2010). Attention, uncertainty, and free-energy. Frontiers in human neuroscience 4, 1-23.
- Fell, J., and Axmacher, N. (2011). The role of phase synchronization in memory processes. Nat Rev Neurosci 12, 105-118.
- Felleman, D.J., and Van Essen, D.C. (1991). Distributed hierarchical processing in the primate cerebral cortex. Cereb Cortex 1, 1-47.
- Fiorani, M., Azzi, J.C., Soares, J.G., and Gattass, R. (2014). Automatic mapping of visual cortex receptive fields: a fast and precise algorithm. Journal of neuroscience methods *221*, 112-126.
- Fries, P. (2009). Neuronal gamma-band synchronization as a fundamental process in cortical computation. Annual review of neuroscience 32, 209-224.
- Fries, P. (2015). Rhythms for Cognition: Communication through Coherence. Neuron 88, 220-235.
- Fries, P., and Maris, E. (2022). What to Do If N Is Two? J Cogn Neurosci 34, 1114-1118.
- Fries, P., Nikolić, D., and Singer, W. (2007). The gamma cycle. Trends in neurosciences 30, 309-316.
- Fries, P., Womelsdorf, T., Oostenveld, R., and Desimone, R. (2008). The effects of visual stimulation and selective visual attention on rhythmic neuronal synchronization in macaque area V4. J Neurosci 28, 4823-4835.
- Friese, U., Supp, G.G., Hipp, J.F., Engel, A.K., and Gruber, T. (2012). Oscillatory MEG gamma band activity dissociates perceptual and conceptual aspects of visual object processing: a combined repetition/conceptual priming study. Neuroimage *59*, 861-871.
- Friston, K. (2005). A theory of cortical responses. Philosophical transactions of the Royal Society of London Series B, Biological sciences *360*, 815-836.
- Friston, K.J., Holmes, A.P., and Worsley, K.J. (1999). How many subjects constitute a study? Neuroimage 10. 1-5.
- Galuske, R.A.W., Munk, M.H.J., and Singer, W. (2019). Relation between gamma oscillations and neuronal plasticity in the visual cortex. Proc Natl Acad Sci U S A *116*, 23317-23325.
- Gieselmann, M.A., and Thiele, A. (2008). Comparison of spatial integration and surround suppression characteristics in spiking activity and the local field potential in macaque V1. The European journal of neuroscience 28, 447-459.
- Gieselmann, M.A., and Thiele, A. (2022). Stimulus dependence of directed information exchange between cortical layers in macaque V1. Elife 11.
- Gilbert, C.D. (1977). Laminar differences in receptive field properties of cells in cat primary visual cortex. The Journal of physiology *268*, 391-421.
- Gilbert, C.D., and Li, W. (2012). Adult visual cortical plasticity. Neuron 75, 250-264.
- Gilbert, J.R., Gotts, S.J., Carver, F.W., and Martin, A. (2010). Object repetition leads to local increases in the temporal coordination of neural responses. Frontiers in human neuroscience 4, 30.
- Goebel, R., Esposito, F., and Formisano, E. (2006). Analysis of functional image analysis contest (FIAC) data with brainvoyager QX: From single-subject to cortically aligned group general linear model

- analysis and self-organizing group independent component analysis. Human brain mapping 27, 392-401.
- Gotts, S.J., Chow, C.C., and Martin, A. (2012). Repetition priming and repetition suppression: A case for enhanced efficiency through neural synchronization. Cognitive neuroscience 3, 227-237.
- Grav, C.M., König, P., Engel, A.K., and Singer, W. (1989), Oscillatory responses in cat visual cortex exhibit inter-columnar synchronization which reflects global stimulus properties. Nature 338, 334-337.
- Gray, C.M., and Singer, W. (1989). Stimulus-specific neuronal oscillations in orientation columns of cat visual cortex. Proc Natl Acad Sci U S A 86, 1698-1702.
- Gregoriou, G.G., Gotts, S.J., and Desimone, R. (2012). Cell-type-specific synchronization of neural activity in FEF with V4 during attention. Neuron 73, 581-594.
- Gregoriou, G.G., Gotts, S.J., Zhou, H., and Desimone, R. (2009). High-frequency, long-range coupling between prefrontal and visual cortex during attention. Science 324, 1207-1210.
- Griffiths, B.J., and Jensen, O. (2023). Gamma oscillations and episodic memory. Trends in neurosciences 46, 832-846.
- Grill-Spector, K., Henson, R., and Martin, A. (2006). Repetition and the brain: neural models of stimulusspecific effects. Trends Cogn Sci 10, 14-23.
- Gruber, T., and Müller, M.M. (2002). Effects of picture repetition on induced gamma band responses, evoked potentials, and phase synchrony in the human EEG. Brain research Cognitive brain research 13, 377-392.
- Hacking, S.A., Boyraz, P., Powers, B.M., Sen-Gupta, E., Kucharski, W., Brown, C.A., and Cook, E.P. (2012). Surface roughness enhances the osseointegration of titanium headposts in non-human primates. Journal of neuroscience methods 211, 237-244.
- Hartmann, T.S., Raja, S., Lomber, S.G., and Born, R.T. (2019). Cortico-cortical feedback from V2 exerts a powerful influence over the visually evoked local field potential and associated spike timing in V1. bioRxiv. 792010.
- Hasenstaub, A., Shu, Y., Haider, B., Kraushaar, U., Duque, A., and McCormick, D.A. (2005). Inhibitory postsynaptic potentials carry synchronized frequency information in active cortical networks. Neuron 47, 423-435.
- Hayhoe, M., and Ballard, D. (2005). Eye movements in natural behavior. Trends Cogn Sci 9, 188-194.
- Hendrickson, A.E., Wilson, J.R., and Ogren, M.P. (1978). The neuroanatomical organization of pathways between the dorsal lateral geniculate nucleus and visual cortex in Old World and New World primates. The Journal of comparative neurology 182, 123-136.
- Henrie, J.A., and Shapley, R. (2005). LFP power spectra in V1 cortex: the graded effect of stimulus contrast. Journal of neurophysiology 94, 479-490.
- Hubel, D.H., and Wiesel, T.N. (1962). Receptive fields, binocular interaction and functional architecture in the cat's visual cortex. The Journal of physiology 160, 106-154.
- Hubel, D.H., and Wiesel, T.N. (1965). Receptive fields and functional architecture in two nonstriate visual areas (18 and 19) of the cat. Journal of neurophysiology 28, 229-289.
- Jia, X., Tanabe, S., and Kohn, A. (2013). Gamma and the coordination of spiking activity in early visual cortex. Neuron 77, 762-774.
- Johnston, J.M., Cohen, Y.E., Shirley, H., Tsunada, J., Bennur, S., Christison-Lagay, K., and Veeder, C.L. (2016). Recent refinements to cranial implants for rhesus macaques (Macaca mulatta). Lab animal 45, 180-186.
- Kelly, J.G., and Hawken, M.J. (2017). Quantification of neuronal density across cortical depth using automated 3D analysis of confocal image stacks. Brain Struct Funct 222, 3333-3353.

- König, P., Engel, A.K., and Singer, W. (1996). Integrator or coincidence detector? The role of the cortical neuron revisited. Trends in neurosciences 19, 130-137.
- Lanz, F., Lanz, X., Scherly, A., Moret, V., Gaillard, A., Gruner, P., Hoogewoud, H.M., Belhaj-Saif, A., Loquet, G., and Rouiller, E.M. (2013). Refined methodology for implantation of a head fixation device and chronic recording chambers in non-human primates. Journal of neuroscience methods *219*, 262-270.
- Laurens, J. (2022). The statistical power of three monkeys. bioRxiv, 2022.2005.2010.491373.
- Lewis, C.M., Ni, J., Wunderle, T., Jendritza, P., Lazar, A., Diester, I., and Fries, P. (2021). Cortical gammaband resonance preferentially transmits coherent input. Cell reports *35*, 109083.
- Li, L., Miller, E.K., and Desimone, R. (1993). The representation of stimulus familiarity in anterior inferior temporal cortex. Journal of neurophysiology *69*, 1918-1929.
- Lin, Z., Fateh, A., Salem, D.M., and Intini, G. (2014). Periosteum: biology and applications in craniofacial bone regeneration. J Dent Res *93*, 109-116.
- Lund, J.S., Angelucci, A., and Bressloff, P.C. (2003). Anatomical substrates for functional columns in macaque monkey primary visual cortex. Cereb Cortex *13*, 15-24.
- Mahmoudian, B., Dalal, H., Lau, J., Corrigan, B., Abbass, M., Barker, K., Rankin, A., Chen, E.C.S., Peters, T., and Martinez-Trujillo, J.C. (2023). A method for chronic and semi-chronic microelectrode array implantation in deep brain structures using image guided neuronavigation. Journal of neuroscience methods 397, 109948.
- Maier, A., Adams, G.K., Aura, C., and Leopold, D.A. (2010). Distinct superficial and deep laminar domains of activity in the visual cortex during rest and stimulation. Frontiers in systems neuroscience 4.
- Malach, R., Amir, Y., Harel, M., and Grinvald, A. (1993). Relationship between intrinsic connections and functional architecture revealed by optical imaging and in vivo targeted biocytin injections in primate striate cortex. Proc Natl Acad Sci U S A 90, 10469-10473.
- Markov, N.T., Ercsey-Ravasz, M., Van Essen, D.C., Knoblauch, K., Toroczkai, Z., and Kennedy, H. (2013). Cortical high-density counterstream architectures. Science *342*, 1238406.
- Markov, N.T., Ercsey-Ravasz, M.M., Ribeiro Gomes, A.R., Lamy, C., Magrou, L., Vezoli, J., Misery, P., Falchier, A., Quilodran, R., Gariel, M.A., *et al.* (2014a). A weighted and directed interareal connectivity matrix for macaque cerebral cortex. Cereb Cortex *24*, 17-36.
- Markov, N.T., Vezoli, J., Chameau, P., Falchier, A., Quilodran, R., Huissoud, C., Lamy, C., Misery, P., Giroud, P., Ullman, S., *et al.* (2014b). Anatomy of hierarchy: feedforward and feedback pathways in macaque visual cortex. The Journal of comparative neurology *522*, 225-259.
- Markram, H., Gerstner, W., and Sjöström, P.J. (2012). Spike-timing-dependent plasticity: a comprehensive overview. Frontiers in synaptic neuroscience 4, 2.
- Mayer, A., Schwiedrzik, C.M., Wibral, M., Singer, W., and Melloni, L. (2016). Expecting to See a Letter: Alpha Oscillations as Carriers of Top-Down Sensory Predictions. Cereb Cortex 26, 3146-3160.
- McGuire, B.A., Gilbert, C.D., Rivlin, P.K., and Wiesel, T.N. (1991). Targets of horizontal connections in macaque primary visual cortex. The Journal of comparative neurology *305*, 370-392.
- McMahon, D.B., and Olson, C.R. (2007). Repetition suppression in monkey inferotemporal cortex: relation to behavioral priming. Journal of neurophysiology *97*, 3532-3543.
- Michalareas, G., Vezoli, J., van Pelt, S., Schoffelen, J.M., Kennedy, H., and Fries, P. (2016). Alpha-Beta and Gamma Rhythms Subserve Feedback and Feedforward Influences among Human Visual Cortical Areas. Neuron 89, 384-397.
- Miller, C.T., Freiwald, W.A., Leopold, D.A., Mitchell, J.F., Silva, A.C., and Wang, X. (2016). Marmosets: A Neuroscientific Model of Human Social Behavior. Neuron *90*, 219-233.
- Miller, E.K., Li, L., and Desimone, R. (1993). Activity of neurons in anterior inferior temporal cortex during a short-term memory task. J Neurosci *13*, 1460-1478.

- Mitzdorf, U. (1987). Properties of the evoked potential generators: current source-density analysis of visually evoked potentials in the cat cortex. The International journal of neuroscience 33, 33-59.
- Mulliken, G.H., Bichot, N.P., Ghadooshahy, A., Sharma, J., Kornblith, S., Philcock, M., and Desimone, R. (2015). Custom-fit radiolucent cranial implants for neurophysiological recording and stimulation. Journal of neuroscience methods 241, 146-154.
- Mumford, D. (1992). On the computational architecture of the neocortex. II. The role of cortico-cortical loops. Biological cybernetics 66, 241-251.
- Murakami, S., and Okada, Y. (2015). Invariance in current dipole moment density across brain structures and species: physiological constraint for neuroimaging. Neuroimage 111, 49-58.
- Nandy, A.S., Nassi, J.J., and Reynolds, J.H. (2017). Laminar Organization of Attentional Modulation in Macague Visual Area V4. Neuron 93, 235-246.
- NC3Rs (2015). Chronic Implants Wiki (https://www.ciwiki.net/).
- Neuenschwander, S., Rosso, G., Branco, N., Freitag, F., Tehovnik, E.J., Schmidt, K.E., and Baron, J. (2023). On the Functional Role of Gamma Synchronization in the Retinogeniculate System of the Cat. J Neurosci 43, 5204-5220.
- Nurminen, L., Merlin, S., Bijanzadeh, M., Federer, F., and Angelucci, A. (2018). Top-down feedback controls spatial summation and response amplitude in primate visual cortex. Nature communications 9, 2281.
- Olsen, T. (2023). Current source density (CSD) (https://www.mathworks.com/matlabcentral/ fileexchange/69399-current-source-density-csd: MATLAB Central File Exchange).
- Oostenveld, R., Fries, P., Maris, E., and Schoffelen, J.M. (2011). FieldTrip: Open source software for advanced analysis of MEG, EEG, and invasive electrophysiological data. Computational intelligence and neuroscience 2011, 156869.
- Ortiz-Rios, M., Haag, M., Balezeau, F., Frey, S., Thiele, A., Murphy, K., and Schmid, M.C. (2018). Improved methods for MRI-compatible implants in nonhuman primates. Journal of neuroscience methods 308, 377-389.
- Overton, J.A., Cooke, D.F., Goldring, A.B., Lucero, S.A., Weatherford, C., and Recanzone, G.H. (2017). Improved methods for acrylic-free implants in nonhuman primates for neuroscience research. Journal of neurophysiology 118, 3252-3270.
- Papakostidis, C., and Giannoudis, P.V. (2023). Meta-analysis. What have we learned? Injury 54, S30-S34.
- Passingham, R. (2009). How good is the macaque monkey model of the human brain? Current Opinion in Neurobiology 19, 6-11.
- Peter, A., Stauch, B.J., Shapcott, K.A., Kouroupaki, K., Schmiedt, J.T., Klein, L., Klon-Lipok, J., Dowdall, J.R., Schölvinck, M.L., Vinck, M., et al. (2021). Stimulus-specific plasticity of macaque V1 spike rates and gamma. Cell reports 37, 110086.
- Peter, A., Uran, C., Klon-Lipok, J., Roese, R., van Stijn, S., Barnes, W., Dowdall, J.R., Singer, W., Fries, P., and Vinck, M. (2019). Surface color and predictability determine contextual modulation of V1 firing and gamma oscillations. Elife 8, e42101.
- Pfingst, B.E., Albrektsson, T., Tjellström, A., Miller, J.M., Zappia, J., Xue, X.L., and Weiser, F. (1989). Chronic skull-anchored percutaneous implants in non-human primates. Journal of neuroscience methods 29, 207-216.
- Picaud, S., Dalkara, D., Marazova, K., Goureau, O., Roska, B., and Sahel, J.A. (2019). The primate model for understanding and restoring vision. Proc Natl Acad Sci U S A 116, 26280-26287.
- Prescott, M.J., and Poirier, C. (2021). The role of MRI in applying the 3Rs to non-human primate neuroscience. NeuroImage 225, 117521.

- Psarou, E., Vezoli, J., Schölvinck, M.L., Ferracci, P.A., Zhang, Y., Grothe, I., Roese, R., and Fries, P. (2023). Modular, cement-free, customized headpost and connector-chamber implants for macaques. Journal of neuroscience methods 393, 109899.
- Rao, R.P., and Ballard, D.H. (1999). Predictive coding in the visual cortex: a functional interpretation of some extra-classical receptive-field effects. Nature neuroscience 2, 79-87.
- Rimehaug, A.E., Stasik, A.J., Hagen, E., Billeh, Y.N., Siegle, J.H., Dai, K., Olsen, S.R., Koch, C., Einevoll, G.T., and Arkhipov, A. (2023). Uncovering circuit mechanisms of current sinks and sources with biophysical simulations of primary visual cortex. Elife *12*, e87169.
- Roberts, M.J., Lowet, E., Brunet, N.M., Ter Wal, M., Tiesinga, P., Fries, P., and De Weerd, P. (2013). Robust gamma coherence between macaque V1 and V2 by dynamic frequency matching. Neuron 78, 523-536.
- Rockland, K.S., and Pandya, D.N. (1979). Laminar origins and terminations of cortical connections of the occipital lobe in the rhesus monkey. Brain research *179*, 3-20.
- Rockland, K.S., and Virga, A. (1989). Terminal arbors of individual "feedback" axons projecting from area V2 to V1 in the macaque monkey: a study using immunohistochemistry of anterogradely transported Phaseolus vulgaris-leucoagglutinin. The Journal of comparative neurology 285, 54-72.
- Roelfsema, P.R., and Treue, S. (2014). Basic neuroscience research with nonhuman primates: a small but indispensable component of biomedical research. Neuron 82, 1200-1204.
- Russell, W.M.S., and Burch, R.L. (1959). The principles of humane experimental technique (Methuen).
- Sawamura, H., Georgieva, S., Vogels, R., Vanduffel, W., and Orban, G.A. (2005). Using functional magnetic resonance imaging to assess adaptation and size invariance of shape processing by humans and monkeys. J Neurosci 25, 4294-4306.
- Schneider, C.A., Rasband, W.S., and Eliceiri, K.W. (2012). NIH Image to Image J: 25 years of image analysis. Nature methods 9, 671-675.
- Schroeder, C.E., Mehta, A.D., and Givre, S.J. (1998). A spatiotemporal profile of visual system activation revealed by current source density analysis in the awake macaque. Cereb Cortex 8, 575-592.
- Self, M.W., van Kerkoerle, T., Goebel, R., and Roelfsema, P.R. (2019). Benchmarking laminar fMRI: Neuronal spiking and synaptic activity during top-down and bottom-up processing in the different layers of cortex. Neuroimage 197, 806-817.
- Self, M.W., van Kerkoerle, T., Super, H., and Roelfsema, P.R. (2013). Distinct roles of the cortical layers of area V1 in figure-ground segregation. Curr Biol 23, 2121-2129.
- Shirhatti, V., and Ray, S. (2018). Long-wavelength (reddish) hues induce unusually large gamma oscillations in the primate primary visual cortex. Proc Natl Acad Sci U S A 115, 4489-4494.
- Shushruth, S., Nurminen, L., Bijanzadeh, M., Ichida, J.M., Vanni, S., and Angelucci, A. (2013). Different Orientation Tuning of Near- and Far-Surround Suppression in Macaque Primary Visual Cortex Mirrors Their Tuning in Human Perception. The Journal of Neuroscience 33, 106.
- Sincich, L.C., and Horton, J.C. (2005). The circuitry of V1 and V2: integration of color, form, and motion. Annual review of neuroscience 28, 303-326.
- Singer, W. (2021). Recurrent dynamics in the cerebral cortex: Integration of sensory evidence with stored knowledge. Proc Natl Acad Sci U S A 118.
- Sobotka, S., and Ringo, J.L. (1994). Stimulus specific adaptation in excited but not in inhibited cells in inferotemporal cortex of macaque. Brain research *646*, 95-99.
- Stauch, B.J., Peter, A., Ehrlich, I., Nolte, Z., and Fries, P. (2022). Human visual gamma for color stimuli. eLife 11, e75897.
- Stauch, B.J., Peter, A., Schuler, H., and Fries, P. (2021). Stimulus-specific plasticity in human visual gamma-band activity and functional connectivity. Elife 10, e68240.

- Stettler, D.D., Das, A., Bennett, J., and Gilbert, C.D. (2002). Lateral connectivity and contextual interactions in macague primary visual cortex. Neuron 36, 739-750.
- Tremblay, S., Acker, L., Afraz, A., Albaugh, D.L., Amita, H., Andrei, A.R., Angelucci, A., Aschner, A., Balan, P.F., Basso, M.A., et al. (2020). An Open Resource for Non-human Primate Optogenetics. Neuron 108, 1075-1090 e1076.
- Uran, C., Peter, A., Lazar, A., Barnes, W., Klon-Lipok, J., Shapcott, K.A., Roese, R., Fries, P., Singer, W., and Vinck, M. (2020). Predictability in natural images determines V1 firing rates and synchronization: A deep neural network approach. bioRxiv, 2020.2008.2010.242958.
- van Kerkoerle, T., Self, M.W., Dagnino, B., Gariel-Mathis, M.A., Poort, J., van der Togt, C., and Roelfsema, P.R. (2014). Alpha and gamma oscillations characterize feedback and feedforward processing in monkey visual cortex. Proc Natl Acad Sci U S A.
- van Turennout, M., Ellmore, T., and Martin, A. (2000). Long-lasting cortical plasticity in the object naming system. Nature neuroscience 3, 1329-1334.
- Vanni, S., Hokkanen, H., Werner, F., and Angelucci, A. (2020). Anatomy and Physiology of Macaque Visual Cortical Areas V1, V2, and V5/MT: Bases for Biologically Realistic Models. Cereb Cortex 30, 3483-3517.
- Veit, J., Hakim, R., Jadi, M.P., Sejnowski, T.J., and Adesnik, H. (2017). Cortical gamma band synchronization through somatostatin interneurons. Nature neuroscience 20, 951-959.
- Veit, J., Handy, G., Mossing, D.P., Doiron, B., and Adesnik, H. (2021). Cortical VIP neurons locally control the gain but globally control the coherence of gamma band rhythms. bioRxiv, 2021.2005.2020.444979.
- Vezoli, J., Vinck, M., Bosman, C.A., Bastos, A.M., Lewis, C.M., Kennedy, H., and Fries, P. (2021). Brain rhythms define distinct interaction networks with differential dependence on anatomy. Neuron 109, 3862-3878 e3865.
- Vinck, M., and Bosman, C.A. (2016). More Gamma More Predictions: Gamma-Synchronization as a Key Mechanism for Efficient Integration of Classical Receptive Field Inputs with Surround Predictions. Frontiers in systems neuroscience 10, 35.
- Vinck, M., Lima, B., Womelsdorf, T., Oostenveld, R., Singer, W., Neuenschwander, S., and Fries, P. (2010). Gamma-phase shifting in awake monkey visual cortex. J Neurosci 30, 1250-1257.
- Vinck, M., Womelsdorf, T., Buffalo, E.A., Desimone, R., and Fries, P. (2013). Attentional modulation of cell-class-specific gamma-band synchronization in awake monkey area V4. Neuron 80, 1077-1089.
- Voss, P., Thomas, M.E., Cisneros-Franco, J.M., and de Villers-Sidani, É. (2017). Dynamic Brains and the Changing Rules of Neuroplasticity: Implications for Learning and Recovery. Frontiers in psychology 8, 1657.
- Whittington, M.A., Traub, R.D., Kopell, N., Ermentrout, B., and Buhl, E.H. (2000). Inhibition-based rhythms: experimental and mathematical observations on network dynamics. International journal of psychophysiology: official journal of the International Organization of Psychophysiology 38, 315-
- Wiggs, C.L., and Martin, A. (1998). Properties and mechanisms of perceptual priming. Current Opinion in Neurobiology 8, 227-233.
- Wikipedia contributors (2023). Binomial distribution (Wikipedia, The Free Encyclopedia.).
- Womelsdorf, T., Fries, P., Mitra, P.P., and Desimone, R. (2006). Gamma-band synchronization in visual cortex predicts speed of change detection. Nature 439, 733-736.
- Womelsdorf, T., Lima, B., Vinck, M., Oostenveld, R., Singer, W., Neuenschwander, S., and Fries, P. (2012). Orientation selectivity and noise correlation in awake monkey area V1 are modulated by the gamma cycle. Proc Natl Acad Sci U S A 109, 4302-4307.

- Wong-Riley, M. (1978). Reciprocal connections between striate and prestriate cortex in squirrel monkey as demonstrated by combined peroxidase histochemistry and autoradiography. Brain research *147*, 159-164.
- Xing, D., Yeh, C.I., Burns, S., and Shapley, R.M. (2012). Laminar analysis of visually evoked activity in the primary visual cortex. Proc Natl Acad Sci U S A *109*, 13871-13876.
- Yamahachi, H., Marik, S.A., McManus, J.N., Denk, W., and Gilbert, C.D. (2009). Rapid axonal sprouting and pruning accompany functional reorganization in primary visual cortex. Neuron *64*, 719-729.
- Ziemba, C.M., Perez, R.K., Pai, J., Kelly, J.G., Hallum, L.E., Shooner, C., and Movshon, J.A. (2019). Laminar Differences in Responses to Naturalistic Texture in Macaque V1 and V2. J Neurosci 39, 9748-9756.



# **Appendices**

## **A1 - Dutch Summary**

Het werk dat in dit proefschrift wordt gepresenteerd is het resultaat van meerdere jaren experimenteel werk met makaken in het Fries Lab. Specifiek wordt in hoofdstuk 2 de verfijning van craniale implantaten en implantatietechnieken voor makaken gepresenteerd. Neurofysiologische studies met wakkere makaken vereisen meestal het gebruik van chronische craniale implantaten. Headpost- en connectorkamerimplantaten worden respectievelijk gebruikt om het hoofd te stabiliseren en om connectoren van chronisch geïmplanteerde elektroden te huisvesten. Wii presenteren duurzame, modulaire, cementvrije headpost implantaten gemaakt van titanium, die bestaan uit twee delen: een basisplaat en een bovendeel. De basisplaat wordt eerst geïmplanteerd, bedekt met spier en huid en mag enkele weken tot maanden genezen en osseointegreren. Het bovendeel wordt daar in een tweede, korte operatie aan vastgemaakt. Het ontwerp, de planning en de productie van handmatig gebogen en CNC-gefreesde basisplaten worden in detail beschreven. Daarnaast wordt ook een modulaire, voetloze connector-kamer gepresenteerd die minimale impact op de schedel heeft. Twaalf volwassen mannelijke makaken werden met succes geïmplanteerd met een headpost, en één met de connectorkamer. Tot op heden melden we geen implantaatfalen, grote stabiliteit van het hoofd, en goede conditie van het implantaat, in vier gevallen zelfs meer dan 9 jaar na implantatie. Onze resultaten tonen aan dat geoptimaliseerde implantaten minstens 9 jaar stabiel en gezond kunnen blijven en daarmee de typische duur van experimenten ruim overschrijden. Dit minimaliseert implantaatgerelateerde complicaties en corrigerende operaties en verbetert daardoor aanzienlijk het welzijn van dieren.

Hoofdstuk 3 geeft een kritische evaluatie van de steekproefgroottes die typisch gebruikt worden in studies met niet-menselijke primaten (NHP's). NHP studies gebruiken traditioneel twee of drie dieren. Met behulp van standaard statistiek hebben Fries and Maris (2022) eerder gepleit voor het gebruik van ofwel één dier, voor een gevolgtrekking over die steekproef, of vijf of meer dieren, voor een bruikbare gevolgtrekking over de populatie. Een recent voorgesteld raamwerk pleitte voor het testen van drie dieren en het accepteren van de uitkomst die in de meerderheid werd gevonden als de uitkomst die het meest representatief is voor de populatie (Laurens, 2022). Dit raamwerk wordt getest onder verschillende aannames over de werkelijke waarschijnlijkheid van de representatieve uitkomst in de populatie, oftewel hoe typisch de uitkomst is. Op basis hiervan wordt betoogd dat het raamwerk geldig is voor een breed scala aan typeringen (Laurens, 2022). In dit hoofdstuk laten we zien (1) dat de foutmarge van het raamwerk sterk afhangt

van hoe typisch de representatieve uitkomsten zijn, (2) dat voor een acceptabele foutmarge deze ,typischheid' zeer hoog moet zijn (87% voor één bepaald soort afwijkende waarde), en (3) dat de overgang van één naar drie dieren de foutmarge vooral verlaagt voor ,typischheidswaarden' van 70-90%. Verder gebruiken we conjunctieanalyse om aan te tonen dat twee van de drie dieren met een bepaalde uitkomst slechts een ondergrens van 9% aan typischheid laten zien. Het gebruik van twee of drie dieren maakt dus geen bruikbare gevolgtrekking over de populatie mogelijk en als toch voor deze optie wordt gekozen, moet de afgeleide ondergrens van de typischheid worden gerapporteerd.

Hoofdstuk 4 onderzoekt de effecten van stimulusherhaling op de neuronale reacties in de vroege visuele cortex van een aap. Wanneer een visuele stimulus wordt herhaald, heeft de cortex de gelegenheid om zijn verwerking aan te passen. Zoals verwacht leiden herhaalde stimuli tot het verminderde vuren van neuronen en verhoogde neuronale gamma-band synchronisatie. Eerdere studies vonden dat de herhalingsgerelateerde gammaverhoging optrad bij zowel menselijke als niet-menselijke primaten, voor kunstmatige en natuurlijke stimuli, minutenlang aanhield en niet overging tussen sterk verschillende stimuli. Hier hebben we de herhalingsgerelateerde effecten verder onderzocht met laminaire opnames van multi-unit activiteit en lokale veldpotentialen van de hersengebieden V1 en V2 in wakkere makaken. We vinden effecten op de pieksnelheid van vuren en gamma synchronisatie in alle laminaire compartimenten van V1 en V2. We kwantificeren de mate van stimulus specificiteit met georiënteerde roosters (,oriented gratings') en vinden dat de herhaling-gerelateerde gammaverhoging niet vermindert tussen roosters die slechts 10° verschillen, het kleinste geteste verschil. Bovendien vinden we dat de herhaling-gerelateerde effecten robuust zijn wat betreft stimulus set grootte, zowel wanneer één stimulus werd herhaald als wanneer achttien verschillende stimuli werden herhaald. Tot slot laten we zien dat activiteit in het alfa-bèta frequentiegebied toeneemt en verhoogd blijft wanneer een stimulus wordt herhaald, en sterk afneemt wanneer een onverwachte stimulus wordt gepresenteerd. Deze resultaten suggereren dat herhalingsgerelateerde plasticiteit leidt tot veranderingen in vuursnelheden en ritmische neuronale synchronisatie in verschillende frequentiebanden die de corticale verwerking van herhaalde stimuli aanpassen.

### **A2 - Abbreviations**

NHP = Non-human primate

fMRI = Functional magnetic resonance imaging

FF = Feedforward

FB = Feedback

V1 = Visual area 1 (primary visual area)

V2 = Visual area 2

LGN = Lateral Geniculate Nucleus

L1 = Layer 1

L2/3 = Layer 2/3

L4 = Layer 4

L5 = Layer 5

L6 = Layer 6

SM = Surround modulation

RF = Receptive field

E = Excitatory neurons

I = Inhibitory neurons

PING = Pyramidal-interneuron network gamma

PV = Parvalbumin-Positive interneurons

SOM = Somatostatin-Expressing interneurons

VIP = Vasoactive Intestinal Peptide interneurons

STDP = Spike-Timing-Dependent Plasticity

MUA = Multi-unit activity

CNC = Computer-numerical-control

CT = Computerized tomography

MRI = Magnetic resonance imaging

NSAIDs = Nonsteroidal anti-inflammatory drugs

CBCT = Cone Beam Computed Tomography

PEI = Polyetherimide

PEEK = Polyether ether ketone

PVC = Polyvinyl chloride

CAD = Computer-aided design

NooM = N-out-of-M

2-00-3 = 2-out-of-3

VAR1 = Variable-stimulus block 1

VAR2 = Variable-stimulus block 2

VARX = Variable-stimulus blocks 1 and 2

FIX = Fixed-orientation block

ITI = Intertrial interval

LFP = Local field potential

IIR = Infinite impulse response

uLFP = unipolar LFP

bLFP = bipolar LFP

CSD = Current source density

GC = Granger Causality

stMUA = Single-trial estimate of multiunit activity

stGamma = Single-trial estimate of gamma activity

stAlpha-Beta = Single-trial estimate of alpha-beta activity

## A3 - Data Management

#### **Ethical Approval**

All procedures and housing conditions complied with the German and European law for the protection of animals (EU Directive 2010/63/EU for animal experiments). All surgical and experimental methods that are described in Chapter 2 and Chapter 4 were approved by the regional authority for animal welfare (Regierungspräsidium Darmstadt).

#### **Findability and Accessibility**

The raw data of the study presented in Chapter 4 are stored in the archive of Ernst Strüngmann Institute (ESI) for Neuroscience in Cooperation with Max Planck Society in Frankfurt am Main, (Germany), where the study was conducted.

The models and drawings of the implants and tools presented in Chapter 2 are publicly available in the following repository: https://doi.org/10.5281/zenodo.7300042.

### **Interoperability and Reusability**

The raw and preprocessed trial data (MUA, LFP, and eye data) and MATLAB code used in Chapter 3 and Chapter 4 are documented and stored in the archive of Ernst Strüngmann Institute.

The preprocessed data used in Chapter 4 can be provided upon reasonable request.

## **A4 - Acknowledgements**

I am deeply grateful for this journey and for all the people who supported me over the years.

Pascal, thank you for your supervision, guidance, and support. I am deeply grateful for the trust you showed to my work. Thank you for the knowledge you shared with me on experimental planning, data analysis, writing, working with oscillations, and so much more. Marieke, thank you for being a great co-supervisor and for helping me navigate the final steps of my PhD.

When I first came to Frankfurt, I could not have imagined building such an incredible network of colleagues and friends. I was incredibly lucky to meet amazing people at ESI who became true friends and, over time, family. Tina, Ana, and Irene, thank you for your positive and transformative influence.

Tina, words cannot fully express my gratitude. Thank you for everything—you have been the best flatmate and office mate, my emotional support, and someone I can always rely on. Ana, thank you for making my life and my PhD brighter. Sissi, Irene, Anya, Nisa, Regina, Katharine, and Matteo, thank you for the wonderful moments we shared, even amidst dark times. Amr, Marius, and Petros, I regret that we only grew closer at the end of this work. Thank you for the energy and excitement you brought.

In the Fries Lab, I had the privilege of working with an incredible team of scientists who were also great people. Tina, Mohsen, Ben, Alina, Shivangi, Frederike, Martina, Yufeng, Doro, and Rasmus—you have been the best colleagues I could have asked for.

Rasmus, I am deeply indebted to you for everything you taught me in the lab and for the support you provided throughout these years. What began as a small challenge turned into a great collaboration. It will be difficult to find another colleague as efficient, respectful, and enthusiastic as you. Mohsen and Tina, much of this work would not have been possible without your patience and hard work—thank you for everything.

Christa and Alf, thank you for the excellent veterinary care, for your support and for helping us refine our methods. Georg and David, thank you for helping us implement our ideas, develop and refine our implants.

Misha, thank you for standing by me and supporting me through the most challenging part of my PhD—the experimental phase during COVID. It is hard to imagine those times without your support, our travels, and Plushka.

Thorsten, meeting you during this journey was a great coincidence. Thank you for your generous support, for staying positive during difficult times, and for always being there for me. You really helped me conclude this step.

To my parents, my sister, and Phoebus: Σας ευχαριστώ για την στήριξή σας όλα αυτά τα χρόνια, για την έμπρακτη βοήθεια που μου προσφέρατε τον τελευταίο χρόνο, καθώς και για τις ευκαιρίες, την παιδεία, και την εκπαίδευση που μου χαρίσατε.

This work would not have been possible without the support of all of you and many others. Thank you all.

### A5 - Curriculum Vitae

#### **Education**

- M.Sc. in "Brain and Mind Sciences" (September 2014 March 2017)
  University of Crete, School of Medicine, Heraklion, Greece
- B.Sc in Psychology (September 2009 October 2014)
  Panteion University of Social and Political Sciences, Athens, Greece

#### **Research Experience**

- Researcher (July 2024 present)
  Havenith & Schölvinck Lab, Ernst Strüngmann Institute in cooperation with the Max Planck Society, Frankfurt am Main, Germany
- PhD Candidate (March 2017 present)
  Fries Lab, Ernst Strüngmann Institute in cooperation with the Max Planck Society,
  Frankfurt am Main, Germany
- B.Sc. thesis (2014)
  "A Comparison of Temporal Approximation in Intentional and Crossmodal Binding"
  Laboratory of Cognitive Science; National and Kapodistrian University of Athens, Greece

#### **Publications**

**Psarou, E.**, Katsanevaki, C., Maris, E., & Fries, P. (2024). Would you agree if N is three? On statistical inference for small N. bioRxiv. https://doi.org//10.1101/2024.08.26.609821

Patel, S., **Psarou, E.**, Mönke, G., & Fries, P. (2024). Spectral estimation at the edge. bioRxiv 2024.10.02.616083; doi: https://doi.org/10.1101/2024.10.02.616083

**Psarou, E.**, Patel, S., & Schölvinck, M. (2024). Vision: Running into differences. eLife, 13:e101013. https://doi.org/10.7554/eLife.101013

**Psarou, E.**, Vezoli, J., Schölvinck, M. L., Ferracci, P.-A., Zhang, Y., Grothe, I., Roese, R., & Fries, P. (2023). Modular, cement-free, customized headpost and connector-chamber implants for macaques. Journal of Neuroscience Methods, 393, 109899. https://doi.org/10.1016/j.jneumeth.2023.109899

Stauch, B. J., **Psarou, E.**, Roese, R., & Fries, P. (2022). Phase leads between oscillatory visual stimuli induce a salience illusion. bioRxiv. https://doi.org/10.1101/2022.10.31.514570

Thanopoulos, V., **Psarou, E.**, Vatakis, A. (2018). Robust intentional binding for causally-linked sequences of naturalistic events but not for abstract event sequences. Acta Psychologica, 190, 159–173. https://doi.org/10.1016/j.actpsy.2018.08.001

### **Donders Graduate School**

For a successful research Institute, it is vital to train the next generation of scientists. To achieve this goal, the Donders Institute for Brain, Cognition and Behaviour established the Donders Graduate School in 2009. The mission of the Donders Graduate School is to guide our graduates to become skilled academics who are equipped for a wide range of professions. To achieve this, we do our utmost to ensure that our PhD candidates receive support and supervision of the highest quality.

Since 2009, the Donders Graduate School has grown into a vibrant community of highly talented national and international PhD candidates, with over 500 PhD candidates enrolled. Their backgrounds cover a wide range of disciplines, from physics to psychology, medicine to psycholinguistics, and biology to artificial intelligence. Similarly, their interdisciplinary research covers genetic, molecular, and cellular processes at one end and computational, system-level neuroscience with cognitive and behavioural analysis at the other end. We ask all PhD candidates within the Donders Graduate School to publish their PhD thesis in de Donders Thesis Series. This series currently includes over 600 PhD theses from our PhD graduates and thereby provides a comprehensive overview of the diverse types of research performed at the Donders Institute. A complete overview of the Donders Thesis Series can be found on our website: https://www.ru.nl/donders/donders-series

The Donders Graduate School tracks the careers of our PhD graduates carefully. In general, the PhD graduates end up at high-quality positions in different sectors, for a complete overview see https://www.ru.nl/donders/destination-our-formerphd. A large proportion of our PhD alumni continue in academia (>50%). Most of them first work as a postdoc before growing into more senior research positions. They work at top institutes worldwide, such as University of Oxford, University of Cambridge, Stanford University, Princeton University, UCL London, MPI Leipzig, Karolinska Institute, UC Berkeley, EPFL Lausanne, and many others. In addition, a large group of PhD graduates continue in clinical positions, sometimes combining it with academic research. Clinical positions can be divided into medical doctors, for instance, in genetics, geriatrics, psychiatry, or neurology, and in psychologists, for instance as healthcare psychologist, clinical neuropsychologist, or clinical psychologist. Furthermore, there are PhD graduates who continue to work as researchers outside academia, for instance at non-profit or government organizations, or in pharmaceutical companies. There are also PhD graduates who work in education, such as teachers in high school, or as lecturers in higher education. Others continue in a wide range of positions, such as policy advisors, project managers, consultants, data scientists, web- or software developers, business owners, regulatory affairs specialists, engineers, managers, or IT architects. As such, the career paths of Donders PhD graduates span a broad range of sectors and professions, but the common factor is that they almost all have become successful professionals.

For more information on the Donders Graduate School, as well as past and upcoming defences please visit: http://www.ru.nl/donders/graduate-school/phd/





